PHARMACOLOGICAL POTENTIAL OF CERIUM OXIDE NANOPARTICLES THROUGH PH DEPENDENCY FOR COLON CANCER

by

Elif Tarakcı

Submitted to Graduate School of Natural and Applied Sciences
in Partial Fulfillment of the Requirements
for the Degree of Master of Science in
Biomedical Engineering

Yeditepe University
2023

PHARMACOLOGICAL POTENTIAL OF CERIUM OXIDE NANOPARTICLES THROUGH PH DEPENDENCY FOR COLON CANCER

APPROVED BY:

Assoc. Prof. Dr. Feride Şermin Utku ……
(Thesis Supervisor)
(Yeditepe University)

Assoc. Prof. Dr. Hilal Yazıcı Malkoçoğlu ……
(Thesis Co-Supervisor)
(TÜBİTAK MAM)

Prof. Dr. Gamze Torun Köse ……
(Yeditepe University)

Assist. Prof. Dr. Banu İyisan ……
(Boğaziçi University)

Assist. Prof. Dr. Mukaddes Avşar Saral ……
(Istanbul Aydın University)

DATE OF APPROVAL: ..../..../20..

I hereby declare that this thesis is my own work and that all information in this thesis has been obtained and presented in accordance with academic rules and ethical conduct. I have fully cited and referenced all material and results as required by these rules and conduct, and this thesis study does not contain any plagiarism. If any material used in the thesis requires copyright, the necessary permissions have been obtained. No material from this thesis has been used for the award of another degree.

I accept all kinds of legal liability that may arise in case contrary to these situations.

Name, Last name Elif Tarakcı

Signature …..……

ACKNOWLEDGEMENTS

It is with immense gratitude that I acknowledge the support and help of my supervisor Assoc. Prof. Dr. Hilal Yazıcı Malkoçoğlu. Pursuing my thesis under her supervision has been an experience that broadens the mind and presents an unlimited source of learning.

I would also like to thank my advisor, Assoc. Prof. Dr. Feride Şermin Utku, who has always supported me in every sense since my undergraduate education. She never hesitated to guide me during this Master's period.

I would like to express my deepest gratitude to Dr. Ahsen Morva Yılmaz. I am very grateful to her for her endless patience and guidance throughout this period.

I would like to thank my colleagues Kübra Kıdık, Feride Melisa Bilgin, Jamila Bayramova, Şöhret Meryem Göçek, Yasemin Küçük, Ogün Çoban, Ahmet Dinç, Sahra Esmkhani, Seda Nur Kabadayı, Büşra Ağır and Kadir Ziya Durmuş. Whenever I needed motivation, whenever I faced a problem, they showed me how a teamwork should be.

I would like to thank my family for their endless love and support, making everything more beautiful for my future and their encouragements within this journey.

Many thanks to the Scientific and Technological Research Council of Turkey (TUBITAK) for making this Master's thesis possible with providing sources. This project was funded by The International Centre for Genetic Engineering and Biotechnology (ICGEB) entitled ‘Cetuximab Mediated Molecular Targeted Cancer Therapy Through Nanoceria’.

Finally, I would like to show my greatest gratitude to Mustafa Kemal Atatürk, the founder of Turkey Republic who made it possible for me to study and become a scientist as a young woman.

ABSTRACT

PHARMACOLOGICAL POTENTIAL OF CERIUM OXIDE NANOPARTICLES THROUGH PH DEPENDENCY FOR COLON CANCER

Nanoparticle-based cancer treatments have become attractive recently as an alternative to conventional treatments for colon cancer such as chemotherapy, biological agents, alkylating agents and antimetabolites. However, the major problem in traditional therapies is the side effects that arise in distinguishing normal and cancerous cells and resulting from complications that produce systemic toxicity. Therefore, the application of nanoparticles in cancer treatment emerges as a method aiming for controlled drug delivery and minimizing side effects. Unlike other nanoparticles such as silver, zinc, polymeric and gold nanoparticles etc., used to treat colon cancer, nanoceria is one of the most promising nanoparticles due to its excellent catalytic activities, which is derived from rapid oxidation state between Ce^{4+} and Ce^{3+}. The hypothesis regarding the action mechanism of nanoceria is that cancerous cells are predicted to be acidic and nanoceria can increase the oxidative stress of these acidic cells and apoptosis leading to the destruction of cancer cells. In this study, after detailed characterization (UV-Vis, DLS, FTIR, Raman, XRD, XPS, TGA) of two synthesized Dex-CeNPs (SD1, SD2), their cytotoxicity, reactive species (ROS) scavenging properties and cell health status were evaluated in colon cancer cell lines. Cells were tested in cell culture at concentrations of 100, 250, 500 and 1000 μg/mL. The IC50 values of all cell lines were determined and SD2 synthesis was determined to be effective at lower doses between the two syntheses. However, flow cytometry experiments were continued over SD2 synthesis. With the high cytotoxicity observed in SD1 synthesis, UV-Vis and DLS characterization of the synthesis at pH 6 and pH 7 was performed. Two cell lines with relatively high ROS production (DLD-1 and COLO 201) compared to other three line was chosen for cytotoxicity assay at different pH values of tumors and healthy cells (pH 6 and pH 7). In line with the results, it was observed that both syntheses were synthesized successfully. As a result of the high concentration requirement for SD1 synthesis, the concentration required for the IC50 value for DLD-1 at pH 6 decreased from the two tested cell lines. As a result of these sets of experiments, the concentration required for the IC50 of the SW48 line was greater than 5 mg/mL for both syntheses, so it was not used in the rest of the experiments. SD2 synthesis was promising for future experiments.

ÖZET

KOLON KANSERİ İÇİN PH BAĞIMLILIĞI YOLUYLA SERYUM OKSİT NANOPARTİKÜLLERİNİN FARMAKOLOJİK POTANSİYELİ

Kemoterapi, biyolojik ajanlar, alkilleyici ajanlar ve antimetabolitler gibi kolon kanseri için geleneksel tedavilere bir alternatif olarak son zamanlarda nanopartikül bazlı kanser tedavileri çekici hale gelmiştir. Ancak asıl sorun, geleneksel tedavideki normal ve kanserli hücreleri ayırt etmede ortaya çıkan ve sistemik toksisite oluşturan komplikasyonlardan kaynaklanan yan etkilerdir. Bu nedenle kanser tedavisinde nanopartiküllerin uygulanması, kontrollü ilaç dağıtımını hedefleyen ve yan etkileri en aza indiren bir yöntem olarak karşımıza çıkmaktadır. Kolon kanserini tedavi etmek için kullanılan gümüş, çinko, polimerik ve altın nanopartiküller vb. gibi diğer nanopartiküllerin aksine, nanoceria, Ce^{4+} ve Ce^{3+} arasındaki hızlı oksidasyon geçişiyle türetilen mükemmel katalitik aktivitesi nedeniyle en umut verici nanopartiküllerden biridir. Nanoceria'nın etki mekanizmasına ilişkin hipotez, kanserli hücrelerin asidik olması nedeniyle nanoceria'nın bu asidik hücrelerin oksidatif stresini artırabileceği ve kanser hücrelerinin yok edilmesine yol açan apoptozu artırabileceği yönündedir. Bu çalışmada, sentezlenen iki Dex-CeNP'nin (SD1, SD2) detaylı karakterizasyonunun (UV-Vis, DLS, FTIR, Raman, XRD, XPS, TGA) ardından sitotoksisitesi,reaktif türler (ROS) süpürücü özellikleri ve hücre sağlıklılık durumları kolon kanseri hücrelerinin varlığında, hücre kültüründe 100, 250 500 ve 1000 µg/mL konsantrasyonlarda denenmiştir. Bütün hücre hatlarının IC50 değerleri belirlenmiş ve iki sentez arasında SD2 sentezinin daha düşük dozlarda etkili olduğu belirlenmiştir. Bununla birlikte, akış sitometrisi deneyleri SD2 sentezi üzerinden devam ettirilmiştir. SD1 sentezinde gözlemlenen yüksek sitotoksisiteyle birlikte sentezin pH 6 ve pH 7'de UV-Vis ve DLS karakterizasyonu yapıldıktan sonra ROS üretimi çok yüksek olan iki hücre hattında (DLD-1 ve COLO 201) tümörlerin ve sağlıklı hücrelerin farklı pH değerlerinde (pH 6 ve pH 7) sitotoksisitesine bakılmıştır. Elde edilen sonuçlar doğrultusunda her iki sentezin başarıyla sentezlendiği gözlemlenmiştir. SD1 sentezinin yüksek konsantrasyon gerektirmesi sonucunda denenen iki hücre hattından DLD-1 için pH 6 da IC50 değeri için gereken konsantrasyon düşmüştür. Bu deney setlerinin sonucunda SW48 hattının IC50 için gerektirdiği konsantrasyon her iki sentez için de 5 mg/mL'den büyük olduğundan deneylerin geri kalanında kullanılmamıştır. SD2 sentezi daha ileri çalışmalarda kullanılabilir.

TABLE OF CONTENTS

ACKNOWLEDGEMENTS iv

ABSTRACT v

ÖZET vi

LIST OF FIGURES x

LIST OF TABLES xiii

LIST OF SYMBOLS/ABBREVIATIONS xiv

1. INTRODUCTION 1

1.1. NANOTECHNOLOGY IN BIOMEDICAL SCIENCE 1

1.1.1. Metal Based Nanoparticles 2

1.1.1.1. Metal-oxide Nanoparticles 3

1.1.2. CeO_2 Nanoparticles in Biomedical Science 4

1.1.2.1. Synthesis Strategies of CeO_2 5

1.1.2.2. Surface Coatings for Nanoparticles 8

1.1.2.3. Dextran Coatings of CeO_2 Nanoparticles 8

1.2. APPLICATION OF NANOPARTICLES IN CANCER RESEARCH 9

1.2.1. Dex-CeNPs in Cancer Treatments 13

1.2.2. Dex-CeNPs in Colon Cancer Treatments 14

2. MATERIALS AND METHODS 17

2.1. SYNTHESIS OF DEX-CeNPS 17

2.2. CHARACTERIZATION OF DEX-CeNPS 17

2.2.1. UV-Visible Spectrophotometry 18

2.2.2. Dynamic Light Scattering (DLS) and Zeta Potential Measurements 18

2.2.3. Attenuated Total Reflectance Fourier-transform Infrared (ATR-FTIR) Spectroscopy 18

2.2.4. Raman Spectroscopy 19

2.2.5. High Resolution Transmission Electron Microscopy (HRTEM) 19

2.2.6. X-Ray Diffraction (XRD) 19

2.2.7. X-Ray Photoelectron Spectroscopy (XPS) 19

2.2.8. Thermogravimetric Analysis (TGA) 20
2.2.9. Stability Analysis of Synthesized Dex-CeNPs 20
2.3. MAMMALIAN ADHERENT CELL CULTURE 20
2.3.1. Colon Cell Lines and Media 21
2.3.2. General Cell Culture Procedure 21
2.3.3. Mycoplasma Detection 22
2.4. CELL CULTURE PROCEDURES 23
2.4.1. Cytotoxicity (WST-1) Assay Procedure for Colon Cancer Cell Lines 24
2.4.1.1. pH-dependent Cytotoxicity Assay of Colon Cancer Cell Lines 25
2.4.1.2. Half Maximal Inhibitory Concentration (IC50) Calculation 26
2.4.2. Reactive Oxygen Species (ROS) Measurements 26
2.4.3. Flow Cytometry Analysis 26
2.4.4. Statistical Analysis 27
3. RESULTS 28
3.1. SYNTHESIS AND CHARACTERIZATION OF DEX-CeNPS 28
3.1.1. Synthesis Strategy of Dex-CeNPs 28
3.1.2. Characterization of Dex-CeNPs 28
3.1.2.1. Ultraviolet-Visible (UV-Vis) Spectroscopy 29
3.1.2.2. Dynamic Light Scattering (DLS) Measurement 30
3.1.2.3. Attenuated Total Reflectance-Fourier Transform Infrared (ATR-FTIR) Spectroscopy 30
3.1.2.4. Raman Spectroscopy 31
3.1.2.5. High Resolution Transmission Electron Microscopy (TEM) 32
3.1.2.6. X-Ray Diffraction (XRD) 33
3.1.2.7. X-Ray Photoelectron Spectroscopy (XPS) 34
3.1.2.8. Thermogravimetric Analysis (TGA) 34
3.1.2.9. Stability of Dextran-Coated Nanoceria 35
3.2. DEX-CeNP AS A DRUG CANDIDATE FOR COLON CANCER 40
3.2.1. Cellular Impact of Dex-CeNPs (SD1 and SD2) Against Colon Cancer 40
3.2.1.1. Determination of Dex-CeNPs Concentration Ranges 43
3.2.1.2. Determination of Higher Concentrations 46
3.2.1.3. Determination of Narrowed Concentrations 47

3.2.1.4. IC50 Determination of Colon Cancer Cell Lines 50
3.2.2. Cell Number Determination of Colon Cancer Cell Lines 51
3.2.3. Reactive Oxygen Species Generation of Dextran-coated Nanoceria on Colon Cancer Cell Lines 51
3.2.4. Flow Cytometry Analysis 54
3.3. pH Dependent Anti-cancer Properties of Dextran-coated Nanoceria 61
3.3.1. Characterization of SD1 with pH6 and pH7 62
3.3.2. WST-1 Assay with pH Adjusted Dex-CeNPs 63
3.3.2.1. IC50 Values pH Adjusted Dex-CeNPs on Colon Cancer Lines 67
4. DISCUSSION 68
5. CONCLUSION 75
6. FUTURE DIRECTIONS 76
REFERENCES 78
APPENDIX A 91
APPENDIX B 92
APPENDIX C 93

LIST OF FIGURES

Figure 1.1. A scheme of biomedical applications of Nanoceria [12]. 4

Figure 1.2. Oxidation exchange between Ce^{3+}/Ce^{+4} of Nanoceria [15] 5

Figure 1.3. Comparison between conventional therapy and nanotechnology enhanced therapy. 10

Figure 3.1. The colour change during synthesis of (a) SD1 from 1 hour to 18 hours (left) and UV-Vis spectrum of SD1 (right) (b) colour change during synthesis of SD2 1 hour to 18 hours (left) and UV-Vis spectrum of SD2 (right). 29

Figure 3.2. DLS and zeta potential measurements of Dex-CeNPs. (a) size distribution by number and (b) zeta potential values of SD1 and SD2. 30

Figure 3.3. ATR-FTIR spectra of Dex-CeNPs. (a) SD1 and (b) SD2. 31

Figure 3.4. Raman spectra of SD1 and SD2. (a) Raman spectra of SD1 and D1, (b) Raman spectra of SD2 and D2. 32

Figure 3.5. TEM characterization of Dex-CeNPs. (a) SD1 and (b) SD2. 33

Figure 3.6. XRD results of SD1 and SD2. (a) XRD patterns (b) angle, intensity and d value table of both Dex-CeNPs. 33

Figure 3.7. XPS spectra of SD1 and SD2. (a) XPS spectra of SD1, (b) XPS spectra of SD2. 34

Figure 3.8. TGA plots of SD1 and SD2. 35

Figure 3.9. 6- month period stability analysis of Dex-CeNPs (SD1 and SD2) via UV-Vis spectroscopy and DLS. (a) UV-Vis spectrum of SD1, (b) DLS analysis of SD1, (c) zeta potential analysis of SD1, (d) UV-Vis Spectrum of SD2. 37

Figure 3.10. Mycoplasma detection results of colon cancer cell lines. (a) agarose gel image of PCR products, (b) MycoAlert™ PLUS mycoplasma detection kit contamination results. 42

Figure 3.11. Cytotoxic properties of two Dex-CeNPs (SD1 and SD2) against (a) DLD-1, (b) COLO 201, (c) LoVo, (d) HT-29, (e) SW48 cell lines at 100, 250, 500, 1000 μg/mL concentrations after 1 and 3 days of treatment. * Represents comparison between SD1 control group and each concentration (p-value≤0.001), # Represents comparison between SD2 control group and each concentration.(p-value≤0.001), ** Represents comparison between SD1 and SD2 at the same concentration. (p-value≤0.001), ## Represents comparison between SD1, Day3 and SD2, Day3 at the same concentration (p-value≤0.001). 43

Figure 3.12. Cytotoxic properties of two Dex-CeNPs (SD1 and SD2) against, (a) LoVo, (b) SW48 cell lines at readjusted concentrations after 1 and 3 days of treatment. * Represents comparison between SD1 control group and each concentration (p-value≤0.001), # Represents comparison between SD2 control group and each concentration.(p-value≤0.001), ** Represents comparison between SD1 and SD2 at the same concentration. (p-value≤0.001), ## Represents comparison between SD1, Day3 and SD2, Day3 at the same concentration (p-value≤0.001). 46

Figure 3.13. Cytotoxic properties of two Dex-CeNPs (SD1 and SD2) with narrowed concentrations. (a) DLD-1 with SD1, (b) DLD-1 with SD2, (c) COLO 201 with SD1, (d) COLO 201 with SD2, (e) LoVo w SD1, (f) LoVo with SD2 (g) HT-29 with SD1 and SD2, (h) SW48 with SD1. * Represents comparison between control group and each concentration (p-value≤0.001). 48

Figure 3.14. Cell viability of colon cancer cell lines. 51

Figure 3.15. ROS formation based on two Dex-CeNPs (SD1 and SD2). (a) DLD-1, (b) COLO 201, (c) LoVo, (d) HT-29, (e) SW48. * Represents comparison between SD1 control group and each concentration. (p-value≤0.001) # Represents comparison between SD2 control group and each concentration. (p-value≤0.001)** Represents comparison between SD1 and SD2 at the same concentration. (p-value≤0.001) 52

Figure 3.16. Effect of Dex-CeNP (SD2) on apoptosis profile of DLD-1 cells. (a) no treatment, (b) 100 μg /mL, (c) 215 μg /mL and (d) 250 μg /mL Dex-CeNP treatment. 56

Figure 3.17. Effect of Dex-CeNPs (SD2) on apoptosis profile of COLO 201 cells. (a) no treatment, (b) 100 µg /mL, (c) 124 µg /mL and (d) 250 µg /mL Dex-CeNPs treatment.....57

Figure 3.18. Effect of Dex-CeNPs (SD2) on apoptosis profile of LoVo cells. (a) no treatment, (b) 500 µg /mL, (c) 623 µg /mL and (d) 1000 µg /mL Dex-CeNPs treatment.....59

Figure 3.19. Effect of Dex-CeNP (SD2) on apoptosis profile of HT-29 cells. (a) no treatment, (b) 250 µg /mL, (c) 482 µg /mL and (d) 500 µg /mL Dex-CeNPs treatment.....60

Figure 3.20. The size and size distribution of Dex-CeNPs studied using UV-Vis spectroscopy and DLS. (a) UV-Vis Spectrum of SD1 at pH 6 , (b) DLS measurement of SD1 at pH 6, (c) UV-Vis spectrum of SD1 at Ph 7, (d) DLS measurement of SD1 at pH 7.....62

Figure 3.21. Cytotoxic properties of Dex-CeNPs (SD1) at pH 6 and pH 7 on DLD-1. (a) SD1 at pH 6 on DLD-1, (b) SD1 at pH 6 and not adjusted pH on DLD-1, (c) SD1 at pH 7 on DLD-1, (d) SD1 at pH 6 and not adjusted pH on DLD-1. * Represents comparison between SD1 control group and each concentration (p-value≤0.001), # Represents comparison between SD2 control group and each concentration.(p-value≤0.001), ** Represents comparison between SD1 and SD2 at the same concentration. (p-value≤0.001).....64

Figure 3.22. Cytotoxic properties of Dex-CeNP (SD1) against COLO 201 cell line at pH 6 and pH 7. (a) SD1 at pH 6 on COLO 201, (b) SD1 at pH 6 and not adjusted pH on COLO 201, (c) SD1 at pH 7 on COLO 201, (d) SD1 at pH 6 and not adjusted pH on COLO 201. * Represents comparison between SD1 control group and each concentration (p-value≤0.001), # Represents comparison between SD2 control group and each concentration.(p-value≤0.001). 66

LIST OF TABLES

Table 1.1. Biomedical applications of metal nanoparticles [10]. 3

Table 2.1. Cell lines and cell culture media.....21

Table 2.2. PCR reaction conditions for mycoplasma analysis. 23

Table 2.3. Concentration range of Dex-CeNPs (SD1 and SD2) for colon cancer.....25

Table 3.1. Mutation types and MSI status in colon cancer cell lines. 41

Table 3.2. IC50 values of colon cancer cell lines with respect to SD1 and SD2.....50

Table 3.3. Diagrammatic representation of the expected flow cytometry results. 55

Table 3.4. The percentage of DLD-1 cells corresponding to each apoptotic level.....57

Table 3.5. The percentage of COLO 201 cells corresponding to each apoptotic level (mean ± sd).. 58

Table 3.6. The percentage of LoVo cells corresponding to each apoptotic level (mean ± sd). 60

Table 3.7. The percentage of HT-29 cells corresponding to each apoptotic level (mean ± sd). 61

Table 3.8. IC50 values of DLD-1, COLO 201 cell lines with respect to pH 6 and pH 7.....67

LIST OF SYMBOLS/ABBREVIATIONS

AcOH	Acetic acid
AgO	Silver(II) oxide
Al_2O_3	Aluminium oxide
a.u	Absorbance units
ATP	Adenosine triphosphate
BSA	Bovine serum albumin
cm^2	Centimetres squared
CeO_2	Cerium oxide
CO_2	Carbon dioxide
CuO	Copper(II) oxide
CT	Computed tomography
DAPI	4′,6-diamidino-2-phenylindole
DCFDA	2 ', 7'- dichlorofluorescein diacetate
Dex-CeNPs	Dextran-coated cerium oxide nanoparticles
DLS	Dynamic light scattering
DNA	Deoxyribonucleic acid
DOPA	Dopamine
EDA	Ethylenediamine
EGFR	Epidermal growth factor receptor
EPR	Enhanced permeability and retention
eV	Electron volt
FBS	Fetal bovine serum
FDA	Food and drug administration
FSC-A	Forward scattering area
FTIR	Fourier- transform infrared spectroscopy
GIT	Gastrointestinal tract
h	Hour
HRTEM	High resolution transmission electron microscopy
IBD	Inflammatory bowel disease
IC50	Half-maximal inhibitory concentration

M	Molar
max	Maximum
MBC	Metastatic breast cancer
MDR	Multi-drug resistance
min	Minutes
mL	Milliliter
mm	Millimeter
MRI	Magnetic resonance imaging
mV	Millivolt
Nanoceria	Cerium oxide nanoparticles
nm	Nanometer
NP	Nanoparticle
NSCLC	Non-small cell lung carcinoma
PA	Polyaspartate
PAA	Poly-acrylic acid
PB	Pacific blue
PBS	Phosphate-buffered saline
PCL	Polycaprolactone
PCR	Polymerase chain reaction
PGA	Poly glutamic acid
PHPMA	Poly(N-(2-hydroxypropyl)-metacrylamide
PDI	Polydispersity index
PI	Propidium iodide
PLGA	Polylactic-co-glycolic acid
PLA	Polylactic acid
PEG	Polyethylene glycol
PET	Positron emission tomography
pH	Power of hydrogen
PTX	Paclitaxel
ROS	Reactive oxygen species
rpm	Revolutions per minute
sec	Seconds
SnO_2	Tin(IV) oxide

SPECT	Single-photon emission computerized tomography
SSC-A	Side scattering area
TGA	Thermogravimetric analysis
TiO_2	Titanium dioxide
VEGF	Vascular endothelial growth factor
XPS	X-ray photoelectron spectroscopy
XRD	X-ray diffraction spectroscopy
ZnO	Zinc oxide
ZrO_2	Zirconium dioxide

1. INTRODUCTION

Nanotechnology is an integrative scientific field that covers multidisciplinary areas such as biology, medicine, biotechnology, molecular engineering, and physical sciences under one roof [1]. Over the past decades, this field, which has been developing rapidly and achieving revolutionary achievements, brings along new solution alternatives for the problems we encounter in different areas of life such as medicine, agriculture and industry.

Nanotechnology is the name given to the whole of science, engineering and technology studies with materials at the nanoscale (1 to 100 nm). These materials are called nanoparticles, nanomaterials or nanostructures.

Nanoparticles became meaningful because of their unique and adjustable properties, such as electrical and thermal conductivity, light absorption, melting point adjustments, magnetic properties, catalytic activity, wettability, and so on, resulting in enhanced features compared to their counterparts [1, 2]. Due to the remarkable properties of nanomaterials, the interest in nanotechnological developments has risen recently because of its wide range of applications in various fields, helping to significantly develop and even revolutionize multiple technologies and industrial sectors, such as information technology, security, transportation, medicine, energy, food, environmental science, and biomedical science.

1.1. NANOTECHNOLOGY IN BIOMEDICAL SCIENCE

Nanotechnology is a facilitating tool for designing new materials and devices that open a new biomedical engineering era covering technology, biology, and medicine [3]. The potential use of nanotechnology in biomedical engineering includes the prevention, early diagnosis, treatment of several diseases, and equipment for a better quality of life for patients. The development of physical/chemical biology, fabrication principles, and predictive methods to adjust them has led to significant advances in nanomedicine and nanomaterials.

Biomedical applications in Nanotechnology are comprehensive and can divide into four categories which are diagnostics, therapeutic applications, immunization and vaccine production, and antiviral applications via drug-resistant bacteria. Following this, various

nano-sized structures have developed to advance biomedical nanotechnology strategies, including nanorods, nano shells, nanospheres, nanostrips, nanowires, nanocrystals, nanotubes, nanofibers, nano stars, nanocages, quantum dots, and nanoparticles [4].

Apart from classifying them according to shapes, the type of material is also crucial for biomedical applications due to the concern of biocompatibility. In the literature, nanomaterial origins can be classified as carbon-based, metal-based, ceramic-based, polymeric, and biomolecule-derived nanomaterials with four main headings [4]. By using nanotechnological applications and materials in the diagnosis and treatment of diseases, it has found a very wide application area in medicine, and it's called nanomedicine. In recent years, it has been shown in many studies that metal-based nanomaterials have antibacterial, antiviral, anticancer properties for use in biomedical fields such as treatments of different pathogens and cancer therapies [5].

Recently, the best examples of successful use of nanomaterials are the Pfizer-BioNTech and Moderna COVID-19 mRNA vaccines developed against the COVID-19. Apart from this, gold nanoparticles as metal based nanoparticles are successfully applied in rapid pregnancy and COVID-19 tests.

1.1.1. Metal Based Nanoparticles

Metal-based nanoparticles have a metal core that includes an inorganic metal/metal oxide, usually covered with a shell of organic or inorganic material/metal oxide [6]. They are characterized by small size with a large surface area. Their size, surface charge, and shape all impact their cellular uptake. Some metal nanoparticles can enhance their cellular interactions with the help of their functionalities present on their surface [7].

Physical and chemical methods are used to prepare nanoparticles. Metallic nanoparticles, such as gold, silver, iron, zinc and metal oxide nanoparticles, show great promise in biomedical applications because of their large surface area/volume ratio produced by both methods [8].

1.1.1.1. Metal-oxide Nanoparticles

The potential technological applications of metal oxide nanoparticles play a vital role in attracting researchers from materials chemistry, medicine, agriculture, information technology, biomedical, optics, electronics, catalysis, environment, energy and sense. CuO, ZnO, SnO_2, Al_2O_3, MgO, ZrO_2 AgO, TiO_2, CeO_2 are the examples of metal-oxide nanoparticles [9]. Changes in cell parameters were observed in nanoparticles due to size-dependent structural changes. As the size decreases in nanoparticles, increasing number of surface and interface atoms produce strain or stress resulting in adjacent structural distortions.

Table 1.1. Biomedical applications of metal nanoparticles [10].

Material	Material Type	Properties	Biomedical Applications
Iron Oxides	Fe_2O_3, Fe_3O_4, Fe_3S_4, MeO- Fe_2O_3 where M=Ni, Co, Zn	Magnetism catalytic properties	Molecular Labeling Imaging Drug Delivery Biomagnetic separation
TiO_2	Single-Crystalline metal-oxide, Wide band gap semiconductor	Photocatalytic activity Biocompatibility	Biomedical Implants Photocatalytic damage Neurochemical Imaging
ZnO, MnO_2, ZrO_2	Used mainly in composite films	Catalytic properties Anti-Inflammatory action	Antibacterial and Anti-inflammatory agents
CeO_2	Present in two states of Ce^{3+}/ Ce^{4+}	Catalytic properties Antioxidant /radical scavenging properties Biocompatible	Drug Delivery Imaging Neuroprotective Anti-inflammatory agents

1.1.2. CeO_2 Nanoparticles in Biomedical Science

Cerium oxide nanoparticles have various deformities on the nanoparticle's surface; these defects are oxygen vacancies resulting in an unstable valance switch of Cerium (IV) and Cerium (III) oxidation states which coexist on the surface. The results in the redox couple are the reason for the catalytic activity of nanoceria, which has raised interest as a biological antioxidant candidate [11].With the help of this remarkable feature, in healthy cells, it acts as an antioxidant by scavenging ROS at physiological pH. Thus, it works as a pro-oxidant by producing ROS in acidic cancer cell environments that result in the death of cells [12]. Nanoceria has widespread biomedical applications as a biosensor, targeted drug/gene delivery systems, anti-diabetic properties, photo receptor protector, tissue engineering, anticancer agent, antioxidant agent and antibacterial agent *in vitro* and *in vivo* research [12, 13], as shown in Figure 1.1.

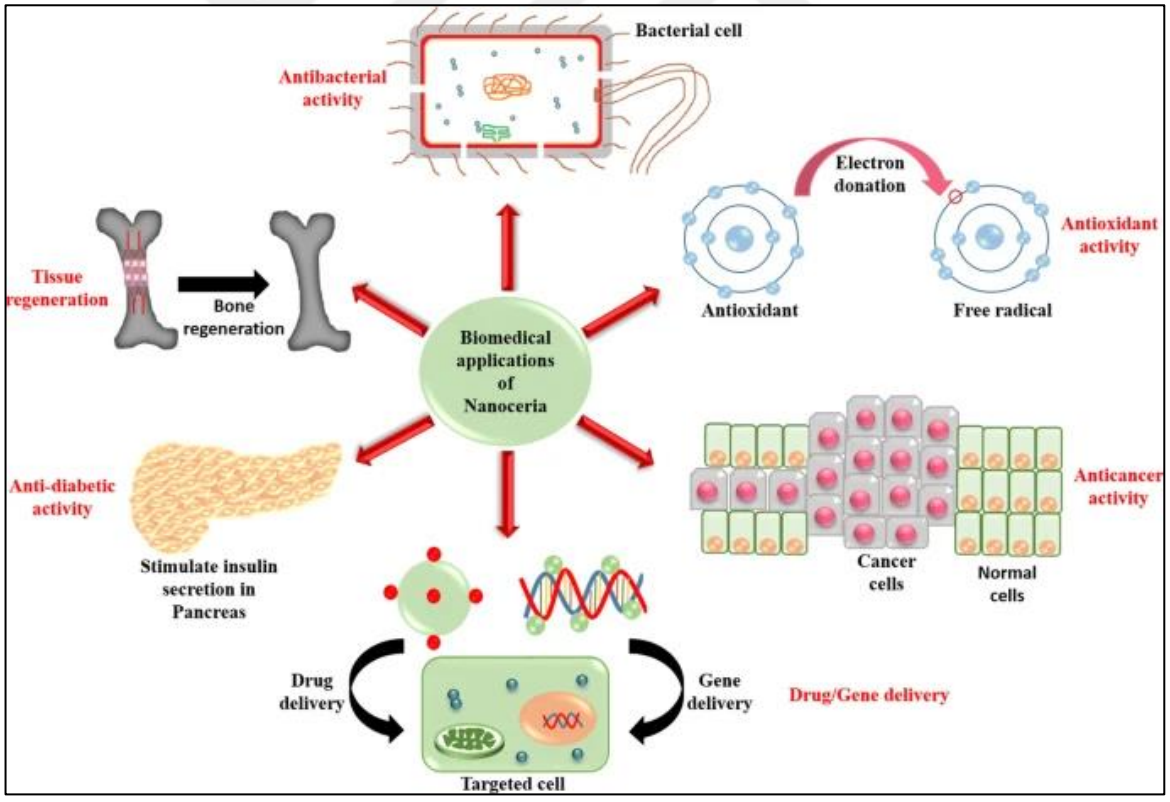

Figure 1.1. A scheme of biomedical applications of Nanoceria [12].

Thus, nanoceria tends to agglomerate due to the vacancies on their surface when not functionalized. In addition, surface functionalization is not only for the prevention of

agglomeration but also to increase the circulation time in the bloodstream and enhance water hydrophilicity [14].

Different synthesis methods are available to have stabilized nanoparticles to control the size, shape, and $Ce^{3+/}Ce^{4+}$ particles, which play a crucial role in forming their physical, chemical and biological properties. Nanotechnological applications in cancer treatment aim to complete the deficiencies of traditional cancer treatment and to turn the disadvantages in cancer development and treatment into advantages.

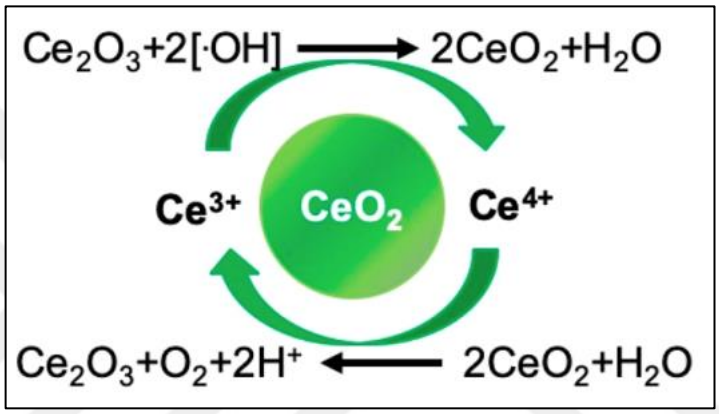

Figure 1.2. Oxidation exchange between Ce^{3+}/Ce^{+4} of Nanoceria [15] .

1.1.2.1. Synthesis Strategies of CeO_2

The correlation of nanoceria between physical and chemical properties and their size and surface morphology is essential for the controllable synthesis of nanoparticles of size and shape [16]. The CeO_2 nanoparticles can be synthesized with different synthesis strategies: precipitation, hydrothermal, green-synthesis, microemulsion process and sol-gel techniques are used as synthesis strategies. [17]. To have a successful synthesis, surface modification is required to increase the stabilization, enhance its biocompatibility, increase cell uptake, and reduce nanoceria agglomeration.

Co-Precipitation method: The precipitation technique, also known as “wet precipitation”, “chemical precipitation” or “aqueous precipitation” is the most common [18] for its simplicity, energy efficacy, possibility to modify nanoparticle surface features and homogeneity [19, 20] due to the synthesis circumstances, such as modification at room temperature or higher desired/required temperatures. The efficacy of a precipitation

technique relies on several factors, including the concentration of ionic metals present in solution and their types, the precipitator used, reaction conditions (especially primarily of the solution key presence) of other components that indirectly affects the synthesis [21]. In the literature, Cerium nitrate hexahydrate is the most used common precursor for nanoceria synthesis in the presence of bases, such as aqueous ammonia, ammonium carbonate, hexamethylenetetramine, potassium carbonate, and NaOH [12].

Green synthesis method: In materials science, "green" synthesis has received intense attention as a reliable, sustainable, and environmentally friendly protocol for synthesizing a variety of materials/nanomaterials, including metal/metal oxides nanomaterials, hybrid materials, and bio-inspired materials by using bioactive agents such as plant materials, microorganisms, and various biowastes including vegetable, fruit peel, eggshells and agricultural wastes [22]. Therefore, green synthesis is seen as an essential tool to reduce the destructive effects associated with traditional synthesis methods for nanoparticles widely used in the laboratory and industry [23].

Hydrothermal Method: Hydrothermal method consists of synthesis by chemical reactions of substances in a closed chamber, heated solution at tremendous temperatures and high pressure. Hydrothermal synthesis is a distinctive technique to crystallize substances from elevated temperatures reaching above 200ºC aqueous solutions under high vaporized pressures above 2000 psi and is also known as the “hydrothermal method" [24, 25].

The hydrothermal method is one of the soft chemical synthesis methods that evolved by mimicking the formation process of some ores in nature. This method is used to grow a variety of crystals to obtain specific organic reactions, to process and discard some organic waste materials that endanger the human living environment in a safe way, or to prepare ultrafine agglomerated or less agglomerated crystalline ceramic powders to sinter some ceramic materials at a relatively low temperature. Today, hydrothermal technology found its place in various fields of science and technology, covering several areas such as materials science, earth science, metallurgy, physics, chemistry and biology [26].

Micro-emulsion Method: Microemulsions are clear, thermodynamically stable liquid mixtures of two incompatible solvents, consisting of nano-sized aqueous or dispersion of oil droplets in a continuous phase [27]. Because of their characteristic interfacial properties, these nanodroplets can be used as nanoreactors allowing intimate contact at the nanoscale

level of hydrophilic and hydrophobic domains. The chemical reactions performed in these environments [28] allow for a broad-range agreement of the relatively well-understood self-assembly dynamics of these materials, and the simplicity of generation of closed structures of certain size and shape.

Their particle size and stability are the essential distinctions between standard emulsion and microemulsion. Coalescence of droplets and Ostwald ripening are aging signs of ordinary emulsions. The surfactant microemulsions used can be classified as water-in-oil (W/O), oil-in-water (O/W) and intermediate continuous structural types that can be reversible from one type to another depending on various ratios. Components and the hydrophilic-lyophilic balance (HLB) value [29]. The dispersed phase consists of monodispersed droplets in size range of 5 –100 nm. By varying parameters, e.g., the type of stabilizer, continuous phase, the precursor content dissolved within the nanodroplets, and the water content referred to as the molar ratio of water to surfactant (W), the nanodroplet size can be modified [29]. In addition, the microemulsion's stability can be influenced by the addition of salt, temperature, pressure or concentration of reagents.

Sol-Gel Method: A sol-gel method is a bottom-up approach in which atoms are converted into nanoparticles. It consists of the conversion of Sol (Colloidal Suspension) to gel [30]. Various applications of Sol-gel methods are preferable in preparing ceramic materials such as metal oxides, nitrides, and carbides. This technique offers several advantages, such as reduced reaction temperature, proper compositional control, high purity level, and the ability to develop large-scale/industrial application processes. The reaction is mainly produced from hydrolysis and condensation of a precursor (inorganic or metal-organic), which results in the formation of sol. After a series of chemical reactions and mild thermal treatments, this sol turns into a gel and is the final calcined material [31, 32].

The precipitation method is mainly used to synthesize nanoceria because of its simplicity among these different methods. In contrast, the green-synthesis way is advantageous. It has been given more consideration nowadays as it limits the toxicity of the solvents and reagents used. However, the need for a sterile environment and maintenance of microbial cultures, also biosafety concerns are still an issue for this method to become more popular. Also, the requirement for high-end devices to perform hydrothermal processes is an obstacle due to financial difficulties and safety concerns due to high temperatures and pressures. Furthermore, the micro-emulsion method has disadvantages such as its limited amount of

solubility capability for materials with high melting points, the requirement for a large number of surfactants and an adjustment of pH are obstacles to performing easy synthesis strategies [33].

1.1.2.2. Surface Coatings for Nanoparticles

Despite the many advantages of nanoparticles as drug carrier systems, there are still various limitations to be solved due to their low oral bioavailability, instability in circulation, random tissue distribution and toxicity [34]. The coating is a crucial technique to enhance the features of nanoparticle materials. Surface coatings of nanomaterials are generally applied to alter or affect different particle properties selectively. Surface coatings of nanomaterials are usually used to selectively change or affect other particle properties. The surface ("core") of a particle can be coated with a wide variety of materials for this aim, which in turn creates a single and multi-layered ("shell"), which is complete or incomplete. The final features of the nanomaterial with coats are ultimately determined by the shell rather than the particle's core. The coatings are used to increase the stabilization, increase the uptake by cells, prevent agglomeration, decrease the cytotoxic effects on healthy cells, and enhance the water solubility and circulation time by making the nanoparticles stealth from the immune system. The functional properties of coating substances such as organic coating materials (chitosan, dextran, heparin, alginate, gelatin, collagen, albumin, etc.) also inorganic coating substances (Poly glutamic acid (PGA), Polycaprolactone (PCL), Poly(N-(2-hydroxypropyl)-metacrylamide (PHPMA), Polylactic-co-glycolic acid (PLGA), Polylactic acid (PLA), Polyethylene glycol (PEG)). Several coatings have been proven to maintain nanoparticle sizes and shapes, which is crucial in minimizing cytotoxic effects [35].

1.1.2.3. Dextran Coatings of CeO_2 Nanoparticles

As one of various surface functional agents, dextran possesses attractive properties since it is a biocompatible, complex polysaccharide commonly used as a surface coat for colloidal nanoparticle synthesis due to its elevated-water solubility. Moreover, in the literature, the surface coating of nanoceria with dextran does not affect/change its redox properties, but only its surface charge [14].

In addition to being highly biocompatible, dextran is also used in FDA-approved nanoparticles such as Dextran-coated iron oxides Feridex [15], which is clinically approved as an MRI contrast agent. The area of its use is for specific/targeted imaging, cell display, and drug and nucleic acid delivery [36]. Therefore, the dextran coating of these Cerium

Oxide nanoparticles may be the reason for the enhanced cytocompatibility compared to other coating substances. Two common types of dextrans are dextran from Leuconostoc mesenteroides and dextran from Leuconostoc spp. as surface coatings and their applications in pharmaceutical industries.

Dextran from Leuconostoc mesenteroides is a linear α-1,6-linked glucose polymer with α-1,3 branches, produced by the fermentation of sucrose by the bacteria Leuconostoc mesenteroides. It has a molecular weight range of 5 to 2,00 kDa and is used in various applications [37, 38]. Dextran from Leuconostoc spp., on the other hand, is a highly branched α-1,6-linked glucose polymer with α-1,2 and α-1,3 branches. It is also produced by the fermentation of sucrose by bacteria of the genus Leuconostoc [39]. It has a molecular weight range of 1,000 to 15,000 kDa and is used in various applications, including as a thickener, stabilizer and pharmaceutical industries [39]. Both types of dextrans have different molecular structures and properties, which make them suitable for different applications.

1.2. APPLICATION OF NANOPARTICLES IN CANCER RESEARCH

Cancer cells are genetically mutant cells that are physiologically different from normal human cells [40]. Nanotechnology has become a powerful tool worldwide for cancer treatment because of its advantageous features compared to conventional therapy. The complexity and heterogeneity of this disease is displayed in Figure 1.3. Nanobiotechnology promotes the fusion of diagnostics and therapeutics, a vital component of a specialized way overcome malignancy [41].

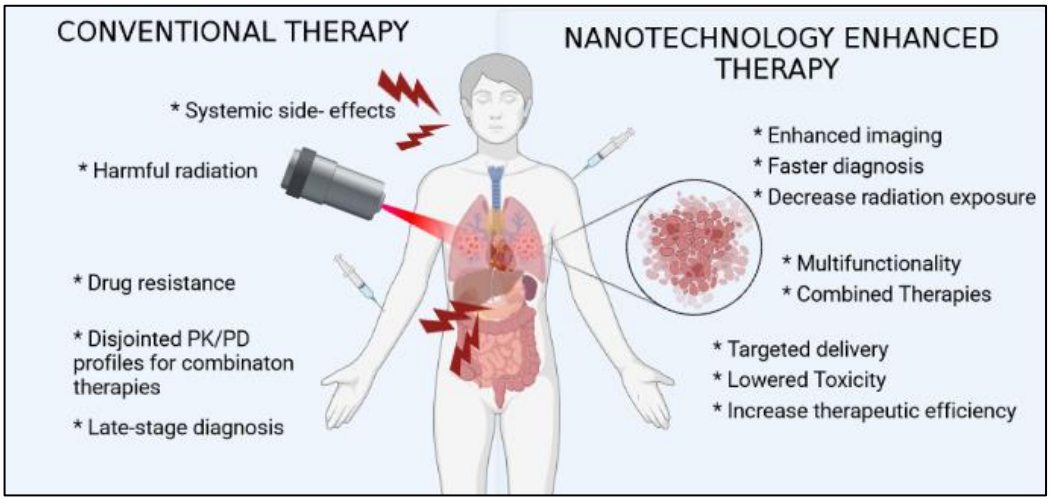

Figure 1.3. Comparison between conventional therapy and nanotechnology enhanced therapy.

Although nanotechnology has a place in almost every field of medicine, 65% of clinical studies in the field of nanomedicine fall under the share of cancer research. The reason for this is that nanomaterials have the potential to increase the effectiveness and reduce the toxicity of chemotherapy and radiotherapy, which are the oldest and primary treatment methods for cancer. Nanoparticles can improve the therapeutic index of the currently available drug by reducing the toxicity level of the drug while increasing the drug efficacy, overcoming drug resistance and accomplishing the steady-state therapeutic level of medications over a long period [42]. To use them for clinical trials, The clinical success of nanoparticles is dependent on (i) stability and time in the bloodstream, (ii) bioactivity to overcome physiological barriers and easy access to the disease site, (iii) biocompatibility, and (iv) toxicity profile [43]. The administration of nanoparticles into organisms can be performed via nasal, oral, intraocular, intratracheal (pulmonary toxicity), injection and other routes.

There are two approaches for diagnosis with the usage of nanomaterials which are biomolecule detection and imaging techniques. Biomolecule detection is used to identify tumor markers present in a small number of biological samples [44]. Modifying nanoparticles by specific ligands with an evaluated affinity for tumor markers can enhance the distinction and evaluating target substances [45, 46]. This technique is known as active targeting of tumor cells. Active targeting of tumor tissue is based on selective targeting of cancer tissue with nanoparticles carrying ligands that can bind to receptors that are over-

expressed on the membranes of cancer cells. With the assistance of antibody (anti-EGFR) [47], peptide (cIBR) [48], sugar [49], RNA, chemotherapeutic drugs etc. surface-modified nanoparticles are able to target cancer cells. The fact that tumor cells have different surface markers from healthy cells allows them to be selectively targeted with modified nanoparticles. However, it has also been shown that nanoparticle-based drug delivery systems can be effective in breaking MDR (multi-drug resistance), which is one of the most important obstacles in cancer treatment [50]. Another targeting method of tumor cells is passive targeting. This technique aims to turn disadvantages into advantages in cancer development and treatment. For example, *Hanahan et al.* have used [51], one of the major cancer markers, as the basis of passive nanotechnological targeting; namely, hypoxia-induced stimulation of Vascular Endothelial Growth Factor (VEGF) to create abnormal vascular structure [52].

These vascular structures formed by cancer cells are quite dense and permeable. Although molecules with a size of less than 2 nm can pass through vessels with normal structures, the size of molecules and particles passing through vessels formed in cancerous tissues can increase up to 50 nm [53]. This situation creates an advantage for nanotechnological applications by providing more nanoparticle release and accumulation in cancerous tissue compared to healthy tissues. *Maeda et al*. reported that they succeeded in passively targeting the tumor tissue with nanoparticles coated with PEG and confirmed that 7-10 times more accumulation of drugs in cancer tissue compared to healthy tissue with the effect of EPR (Enhanced Permeability and Retention) [54].

Over the past 20 years, medical imaging and diagnosis techniques developed rapidly for identifying tiny tumors to detect cancer formation at early stages [55]. This development has formed by combining classical imaging techniques (MRI, PET and SPECT) and nanoparticles [56, 57] All these techniques combine with nanoparticle-mediated drug delivery for accumulation in the target tissue [46]. Currently, many agents are available for the treatment of cancer, depending on the stage of the disease, location, tissue type, age, and condition of the patient [58, 59]. Classical chemotherapeutic agents, radiation treatments, and surgery are still helpful and extensively used to treat cancerous tumors; on the other hand, the side effects are severe concerns for patient health [60, 61]. Also, cancer recurrence due to incomplete removal of malignant cells is a compelling cause of poor prognosis [62, 63]. The use of nanoparticles for early and precise evaluation of cancer cells can prevent late

diagnosis, and direct delivery of tiny amounts of drug to cancer cells can effectively reduce conventional therapy-related side effects by keeping the healthy cells safe [64-66].

One of the main reasons for failures in cancer treatment is MDR (multi drug resistance). Nanoparticle-based drug delivery systems, with their high affinity, stability, and biocompatibility features, offer us new opportunities to combat this reason. MDR overexpression of drug efflux transporters have a complex mechanism such as anomalies in the DNA repair system and apoptotic pathways, hypoxia environment etc., targeting these mechanisms with nanoparticles can result in success. As our knowledge about cancer, its formation and development mechanism increase with new research, new nanotechnological applications are put forward against them. Recent developments in nanomedicine aim to form hybrid nanoparticles using nanoparticles with different properties for drug release in chemotherapy, immunotherapy and targeted therapy applications [50]. Also, using nanoparticles can assist in bypassing the drug resistance of some tumors along with circulation time in the bloodstream, i.e. melanoma, with the assistance of some coating to make them unrecognizable from the immune system [67, 68]. In conclusion, the surface alterations of nanoparticles represent an essential method to successfully develop specific and biocompatible nanomaterials for accurate, sensitive cancer therapy and diagnosis.

The development of nanoparticle biomaterial properties is expected to increase efficacy and help them become a part of conventional cancer therapy. Alterations can understand development in particle design in the tumor microenvironment, which significantly impacts particle deposition. Therefore, the issue of effectiveness can be pointed to accompanying selective and interference of cancer, where nanoparticle-based drug delivery is advantageous. Also, combining these strategies is an option in cleverly designed, meticulous clinical trials that will lead us to the aim of improvement in nanomedicine's efficacy.

As a result of nanomedicine studies in the field of cancer, DOXIL® with liposome-PEG formulation against Karposi’s Sarcoma, multiple myeloma, MBC (metastatic breast cancer) and metastatic ovarian cancer [69]; Eligard® with PLGA formulation developed against prostate cancer [70]; Abraxane® with Albumin® against MBC, NSCLC and Pancreatic cancer and Genexol PM® [71] with mPEG-PLA against MBC [72], for Pancreatic cancer Onivyde® [73] drugs containing liposomes against cancer have been developed and approved by the FDA.

1.2.1. Dex-CeNPs in Cancer Treatments

Dex-CeNPs are being investigated for their potential use in cancer treatments due to their unique properties that make them attractive as drug delivery transporters. Dex-CeNPs can be functionalized with a variety of therapeutic agents, such as chemotherapy drugs and monoclonal antibodies. They can also be designed to target specific cancer cells and deliver the therapeutic agent directly to the site of the tumour which makes them an important candidate for cancer therapies [14, 74-77].

Asati et al. observed that, unlike iron oxide nanoparticles, the intrinsic oxidase-like activity of Dextran-coated nanoparticles could be achieved without the need for using hydrogen peroxide as an electron acceptor or an oxidizing agent for peroxidase-like activity in Dex-CeNPs. They reported that this activity not only depends on the pH change but also varies depending on the particle size and the thickness of the surface coating [78]. Accordingly, it has been observed that the smallest particle and the thinnest surface coating give the most effective results. In the experiment they carried out, they observed that Dex-CeNPs catalyzes rapid oxidation at pH 4, but they did not observe significant oxidation catalysis at pH 7. In line with these results, the pH-dependent oxidase-like activity of Dex-CeNPs has been proven. To validate this research, they selected dopamine (DOPA), which is low in oxidation at low pH levels and observed that DOPA oxidized at pH 4 in the presence of Dex-CeNPs. However, in the control group, no oxidation activity was detected at pH 4, even after days of incubation in the absence of Dex-CeNPs [78].

In the light of this information, it has been observed that Dex-CeNPs are very suitable nanomaterials for targeted cancer therapy, since the cancer microenvironment has an acidic pH due to the lactic acid produced because of anaerobic respiration, while the normal cell microenvironment is known to be close to neutral pH. As important as cell microenvironments are, once inside cells, nanoparticle toxicity may depend on whether they are localized in a particular cellular organelle. For example, the lysosome is acidic, while the cytosol is near neutral pH. In another study by *Asati et al.*, it was observed that dextran-coated nanoceria accumulated mostly in the cytoplasm of cells, did not show any toxic activity, and provided antioxidant properties for these cells. In line with this result, dextran-coated nanoceria may play a role in the protection of healthy cells for radiotherapy, which is one of the recently used cancer treatment method [79].

1.2.2. Dex-CeNPs in Colon Cancer Treatments

GLOBACON data, which shows the world cancer burden according to the morbidity and mortality rates in different populations in the last year, is announced by the International Agency for Research on Cancer. For 2020, the results showed that the number of new cancer cases worldwide was 19.3 million and there were 10.0 million deaths due to cancer. These figures do not include non-melanoma skin cancers (approximately 18.1 million new cases and 9.9 million deaths). Colon cancer accounts for 6% of cancer cases (1,148,515) and 5.8% (576,858) of cancer-related deaths in 2020. When we look at the distribution of colon cancer by world regions, we see that while it has a low incidence in Africa and Asia, it has the highest incidence in North America, New Zealand, Australia and Europe [80]. Also, it is estimated that colon cancer will increase by 56% between 2020 and 2040, to more than 3 million new cases per year. The estimated increase in the number of deaths from the disease is even larger, by 69%, to about 1.6 million deaths worldwide in 2040. These case numbers are considerable despite the availability of effective screening techniques that can reduce the rate of death from colorectal cancer. The death rate due to malignant tumors of the colon, given by TUIK (Turkish Statistical Institute), covers 7.6% of cancer-related deaths in 2018 and 7.4% in 2019. There have been attempts to use dextran coated Cerium Oxide nanoparticles (Dex-CeNPs) in the diagnosis, imaging, and treatment of different diseases of the gastrointestinal tract (GIT), such as inflammatory bowel disease (IBD). One of them is the study of Pratap C. *Naha et al.* using Dex-CeNPs for non-invasive imaging of IBD time GIT. FDA-approved iopamidol-enriched computed tomography (CT) is used as a CT contrast agent for imaging GIT in the clinic [81]. The aim of the research group is that the CT image of iopamidol is not clear and specific in overweight and obese patients, [82, 83] extravasation of the drug in patients [84], to minimize such shortcomings by using Dex-CeNPs. In a study with mouse models, it was shown that Dex-CeNPs-produces strong CT contrast, provides an effective protection against oxidative damage by removing >97% of the drug from the body within the first 24 hours, and it has been argued that Dex-CeNP- is a candidate contrast agent for CT imaging [15]. Another study was conducted by *Zhang et al.* In the study with colon cell lines and mouse models, a hybrid nanoparticle was formed to provide pH-dependent release of Paclitaxel (PTX). First, the PTX-BSA (bovine serum albumin) complex was formed, then it was coated with Dextran by cross-linking method. The release rate of PTX from the pH-sensitive Dex–BSA–PTX NPs complex was

significantly increased at pH 5 compared to pH 7.5. As a result of the study, it was determined that the hybrid NP-inhibited cell proliferation, inducing apoptosis, increasing the half-life of PTX-in in the blood, briefly having a good anti-tumor effect [85].

The study by Aparna *Datta et al.* is based on the anti and pro-oxidant properties of Cerium oxide nanoparticles [86]. CeO_2-in acts as a pro-oxidant at acidic pH (Exp: tumor microenvironment). Cancer cells with higher ROS production compared to healthy tissues [87], CeO_2 NPs cause DNA damage by providing additional ROS production. As a result, the activated TP53 gene activates apoptosis via the mitochondrial pathway. As a result of the study, it has been shown that CeO_2 NP has a dose-dependent anti-proliferative effect in the HCT-116 colon cancer cell line and induces apoptosis by increasing ROS production [86]. In another study with HT-29 colon cancer cell line is biosynthesized 15-20 nm CeO_2-NPs using the extract method. It has been stated that even at 800 µg/mL and higher concentration, it does not show any significant cytotoxicity in the cell line and can be used in the clinic trials [88].

In addition, the surface charge of nanoceria can be altered by changing the pH of the solution in which they are suspended. This can affect the stability, dispersion, and interaction of the CeO_2 NPs with other molecules / materials [89, 90]. Also, the antioxidant and ROS scavenging properties of nanoceria are thought to be pH-dependent which determine the cytotoxicity properties of CeO_2 NPs. Studies have shown that CeO_2 NPs exhibits higher antioxidant activity at more acidic pH values [77, 91]. At pH values below 7, nanoceria is thought to readily accept and donate electrons, allowing it to effectively scavenge ROS and neutralize them. As the pH increases above 7, the activity of CeO_2 NPs as an antioxidant and ROS scavenger is thought to decrease [92]. pH-dependence of CeO_2 NPs antioxidant and ROS scavenging properties may vary depending on the specific conditions and factors present in the system being studied. In the field of cancer research, understanding the effect of pH on the behavior of CeO_2 NPs is important for developing targeted drug delivery systems that can effectively deliver therapeutic agents to cancer cells. In this case, further research is needed to fully understand the role of pH in modulating the activity of CeO_2 NPs as an antioxidant and ROS scavenger.

This study aims to understand the behaviour of synthesized two Dex-CeNPs on five colon cancer cell lines (DLD-1, COLO-201, HT-29, LoVo and SW48). After detailed

characterization (UV-Vis, DLS, FTIR, Raman, XRD, XPS, TGA) of two synthesized Dex-CeNPs (SD1, SD2), their cytotoxicity, reactive species (ROS) scavenging properties and cell health status were evaluated in colon cancer cell lines. Cells were tested in cell culture at concentrations of 100, 250, 500 and 1000 μg/mL. The IC50 values of all cell lines were determined and SD2 synthesis was determined to be effective at lower doses between the two syntheses. However, flow cytometry experiments were continued over SD2 synthesis. With the high cytotoxicity observed in SD1 synthesis, UV-Vis and DLS characterization of the synthesis at pH 6 and pH 7 was performed. Two cell lines with relatively high ROS production (DLD-1 and COLO 201) compared to other three line was chosen for cytotoxicity assay at different pH values of tumors and healthy cells (pH 6 and pH 7).

2. MATERIALS AND METHODS

This section covers the materials and methods used in both characterization analyses and cell culture experiments of Dex-CeNPs.

2.1. SYNTHESIS OF DEX-CeNPS

This study was performed synthesizing two Dex-CeNPs with using two types of dextran according to two protocols published by *Alparslan et al.* and *Naha et al.* with slight modifications [15, 93]. Experimental labels were given to all syntheses and each dextran type to prevent any confusion. Dextran from Leunostoc Mesentoroides (Sigma, Cat#D9260) and Dextran Leuconostoc spp, (Sigma, Cat#31388) were given experimental labels D1 and D2 respectively. Due to the dextran types, synthesis were named as SD1 and SD2.

1 M Cerium nitrate hexahydrate (Ce $(NO_3)_3.6H_2O$) was shortly dissolved in 2 mL water. Alongside, 0.375 M D1 and D2 were dissolved in 2 mL ultrapure water (Hyclone, Cat#SH30529.02). Dextran solution and dissolved Cerium nitrate hexahydrate were mixed in another tube and then while stirring at 1800 rpm for 18 h at 25^{o}C, added dropwise to 6 mL of a 30% ammonium hydroxide solution. The solution turned light yellow after the addition of the precursor into ammonium hydroxide. The solution turned to dark brown colour for SD1 and bright yellow for SD2 Dex- CeNPs. To discard the excess amount of dextran and any other large compounds or agglomerates, particles were centrifuged at 4000 rpm for 30 min two times after 18 hours of stirring. In order to get rid of still remaining excess amount of non-binding elements, all samples were filtered through a 0.45 μm and then 0.22 μm syringe filter after the centrifugation step. The final Dex-CeNP solution was stored in dark at 4^{o}C in order to sustain its stability before all characterization experiments. Relative to the dextran types SD1 and SD2, each synthesis was labelled as stated above.

2.2. CHARACTERIZATION OF DEX-CeNPS

The characterization of the syntheses is very important to see how suitable they are for use. It provides information about the surface charge, size, whether the surface coating is

successful or how long it can remain stable, and shows the compatibility of the synthesized nanoparticles with the characterization data in the literature.

2.2.1. UV-Visible Spectrophotometry

Dex-CeNPs present us quantitative information about the change in oxidation states of Cerium by means of its UV-Visible Spectroscopy. The synthesized dextran-coated nanoceria was diluted at first in cell culture grade dH_2O (Hyclone, Cat # SH30529) at different dilution ratios (1:10, 1:100, 1:1000). Among all dilution ratios, 1:100 taken as a reference for both syntheses. A blank measurement was taken with 1 mL dH_2O in a 10 nm path-length quartz cuvette at Beckman Coulter DU800 Spectrophotometer before performing any measurement. UV-Visible Spectra of all diluted samples were taken at 200-800 nm wavelength ranges.

2.2.2. Dynamic Light Scattering (DLS) and Zeta Potential Measurements

To analyse the particle size, charge, and distribution of nanoparticles, Dynamic light scattering (DLS) experiments were performed. To understand the suitability of surface charge properties of nanoparticles, zeta potential measurements were conducted parallel to the DLS. The same dilution factor (1:100) in dH_2O was chosen according to the best UV-Vis profile to conduct all the DLS and zeta potential measurements. Both Dex- CeNP were analysed by using Zetasizer, NanoZS and Malvern Instruments.

2.2.3. Attenuated Total Reflectance Fourier-transform Infrared (ATR-FTIR) Spectroscopy

As FTIR spectroscopy is an effective tool to determine the type of chemical bonds in molecules, it was performed to evaluate the nanoceria synthesis properties by analysing the binding properties of dextran on the nanoceria surface. For this experiment, each dextran type (D1 and D2), $Ce(NO_3)_3.6H_2O$, synthesis types (SD1, SD2) and each synthesis (undoped nanoparticle) without the addition of $Ce(NO_3)_3.6H_2O$ were compared in liquid form. Two types of dextran (D1, D2) and $Ce(NO_3)_3.6H_2O$ were dissolved in dH_2O and synthesis was

prepared without the addition of Ce $(NO_3)_3.6H_2O$ (undoped) according to the synthesis protocol described above. The FTIR spectra was conducted via Perkin Elmer 100 T spectrometer equipped with MCT detector. Then, the data obtained by the FTIR analysis of the liquid samples were plotted using the Origin 7.5 program.

2.2.4. Raman Spectroscopy

Raman spectroscopy provides a structural fingerprint of Dex-CeNP. The measurements were conducted in using Reflex Raman Microscopy System (Renishaw Plc., New Mills, Wotton-under-Edge Gloucestershire, U.K.). Calibration of system wavelength was carried out automatically at 520 cm^{-1} which belongs to an internal silicon wafer peak. The power of laser was 10 mW and for diode laser, exposure time was 10 seconds for 532 nm. Raman Measurements were performed with 50x (NA:0.25) objective.

2.2.5. High Resolution Transmission Electron Microscopy (HRTEM)

HRTEM image analysis was conducted on JEOL JEM 2100 HRTEM at 200 kV to observe and analyse Dex-CeNP core size, distribution and morphology properties at 80 keV accelerated voltage. SD1 and SD2 were analysed on a carbon-coated copper grid.

2.2.6. X-Ray Diffraction (XRD)

XRD is the experimental tool to define the structure of the Dex-CeNPs along with TEM analysis. XRD analysis was conducted on a D2 Phaser Bruker with a copper anode source. The powders were flattened on a metal holder and data were recorded with a 0.02 2θ° step for a total recording time of 75 minutes. The detector recording time was 1 s per point. A total of 4500 points were recorded.

2.2.7. X-Ray Photoelectron Spectroscopy (XPS)

X-ray photoelectron spectroscopy (XPS) was used to determine the valence state of Dex-CeNPs. XPS spectra were obtained using the PHI 5000 Versa probe (Physical Electronics,

Inc., Chanhassen, MN, USA) model XPS spectrometer equipped with Al Ka X-rays (1486.6 eV) at 100 W. Analysis of the obtained data were evaluated via XPS PEAKFIT 4.1 software. Calibration of charge shifts were done with the C1s peak at 284.8 eV. All obtained peak positions matched with the standard National Institute of Standards and Technology (NIST) XPS database.

2.2.8. Thermogravimetric Analysis (TGA)

TGA is a technique that analysis the change in material properties with temperature. Thermal analysis measurements were carried out by TGA 6300, SII Nano Technology, Japan, system controlled by an EXSTAR 6300 controller. Experiments were conducted using simultaneous TG/DTA analysis by heating the sample in nitrogen atmosphere at 10 Celsius per minute within the temperature range 20℃ and 1400℃.

2.2.9. Stability Analysis of Synthesized Dex-CeNPs

To determine the stability of dextran-coated nanoparticles over a time of up to 6 months, UV-Vis Spectroscopy and DLS measurements were performed. On Day 0, Day 7, Day 14, Day 21, Day 28, 1 month, 2 months, 4 months, and 6 months, SD1 and SD2 were examined in terms of aging characteristics by performing UV-Vis and DLS measurements. As described in UV-Vis Spectroscopy and DLS measurement sections above (section 2.2.1 and 2.2.2), the same experimental protocol was followed.

2.3. MAMMALIAN ADHERENT CELL CULTURE

In this section, general cell culture procedures are described with subsections that include description of colon lines and media, thawing frozen cells, passage of cell lines, cell counting, and mycoplasma detection.

2.3.1. Colon Cell Lines and Media

As a frozen cell line was used, colon cancer cell lines were purchased from the American Cell Culture Collection (ATCC, Manassas, VA, USA). As shown in Table 2.1, each cell line was cultured in a complete medium of its proper media containing 10% Fetal Bovine Serum (FBS, HyClone, Cat#SV30160.03HI), 1% Penicillin/ Streptomycin (Gibco, Cat#15140-122).

Table 2.1. Cell lines and cell culture media.

	Cell Types	Media
Colon Cancer Cell Lines	DLD-1 (ATCC, CCL-221)	RPMI-1640 (ATCC, Cat#30-2001)
	HT29 (ATCC, HTB-38)	McCoy's 5A (Sigma, Cat#M9309)
	Lovo (ATCC, CCL-229)	F-12K Medium (HyClone, Cat#SH30526.01)
	Colo 201 (ATCC, CCL-224)	RPMI-1640 (ATCC, Cat#30-2001)

2.3.2. General Cell Culture Procedure

For cultivation of any cell lines, cryovials preserved in a liquid nitrogen tank for each cell lines till the time of use, they are placed in 37^{o}C water bath until the cell mixture were thawed. Cells were suspended in 5 mL of complete medium and centrifuged at 1300 rpm for 5 min once thawed. Supernatants were discarded and cell pellets were resuspended in 6 mL of fresh medium and transferred to 75cm^2 flasks after centrifugation. The cells were incubated at 37^{o}C in air supplemented with 5% CO_2 until a total confluence of 75% was reached, the old medium was removed from the bottles. The bottles were washed with 1-1.5mL of 1xPhosphate Buffered Saline (PBS) (Sigma, Cat#806544). 1-1.5 mL of Trypsin-EDTA (0.25%; Gibco, Cat#25200-056) was added to the flasks and incubated for 3-5 minutes at 37^{o}C, 5% CO_2. A complete medium was added to the flasks and transferred to centrifuge tubes to be centrifuged at 1300 rpm for 5 minutes at the end of the incubation time. The supernatant was removed after and the cell pellet was gently homogenized in a fresh medium to seed into 75cm^2 flasks. According to given ATCC protocol, the seeding density of each cell line into 75cm^2 flasks was chosen. A live cell count was performed using LUNA-II™ Automated Cell Counter before seeding the cell into proper flasks. Cells were

incubated for 1 minute by mixing with 0.5% trypan blue (Sigma, Cat#T8154) at a ratio of 1: 1 (v / v) for this procedure, 10µL prepared mixture was inserted to the area A and B on LUNA™ Cell Counting Slides (Logos Biosystems). When the cell suspension was diluted with trypan blue, living cells are expected to appear white, small and round as they are not permeable to the dye. On the other hand, dead cells are expected to become large and dark blue, as their membranes are permeable to dye. The Luna Cell Counter device gives the number of cells/mL.

2.3.3. Mycoplasma Detection

The most important danger in the cell culture laboratory is contamination. Common and important contaminants of cell cultures are mycoplasmas. Mycoplasmas are bacteria in the 0.2-0.8 micrometre range, lacking a cell wall. The absence of a cell wall renders these bacteria insensitive to antibiotics. Mycoplasma contamination, which is not usually observed under the microscope, is detected with special staining techniques, biochemical and genetic detection kits.

Two methods were used for the mycoplasma test, which was routinely performed during the cell experiments. The first method was the biochemical MycoAlert™ PLUS Mycoplasma Detection Kit. The operation of this kit is based on the activity of mycoplasma enzymes, which are not found in eukaryotic cells. The mentioned enzymes catalyse the conversion of ADP to ATP. The ATP level before (A) and after (B) adding MycoAlert ® Substrate to each other is below 1-in, indicating the absence of contamination and vice versa. According to the MycoAlert™ PLUS Mycoplasma Detection Kit manual, approximately 200 µL of cell growth media were sampled on day 3 of the cells incubation and centrifuged at 1300 rpm for 5 minutes. 100 µL of the centrifuged sample's supernatant was added to the luminometer tube and 100 µL of MycoAlert™ PLUS reagent was added and incubated at room temperature for 5 minutes. In this process, MycoAlert™ PLUS reagent converts the ATP-i luciferase enzyme to light signal. Before adding 100 µL of MycoAlert™ PLUS substrate to the tube, this signal reads as Read A, and after adding and incubating for 10 minutes, the reading we get is Read B.

Another method is based on detecting mycoplasma DNA in cell culture. The experiment was performed using the N-GARDE Mycoplasma PCR Reagent kit. For the detection of

mycoplasma using the PCR kit, approximately 1 ml of the cell culture supernatant was transferred to a 2 ml Eppendorf tube and centrifuged briefly at 250 x g in accordance with the protocol of the kit. The supernatant was transferred to a new sterile Eppendorf tube and centrifuged at 15,000-20,000 x g for 10 minutes to precipitate mycoplasma. After centrifugation, the supernatant was carefully discarded, Buffer Solution was added to the pellet, mixed well with a micropipette, and then incubated at 95°C for 3 minutes. The resulting test sample can be stored at -20°C or used directly for use for the PCR reaction.

Reaction mix containing primers required for kit DNA polymerization and capable of hybridizing to the genome sequence of interest, includes positive control. The volume of each PCR reaction is equal to a total of 20 µl (10 µl reaction mix, 5 µl test sample and 5 µl dH_2O). The amplification samples obtained as a result of the PCR reaction performed under the conditions shown in Table 2.2 were visualized by running on a 2% agarose gel. The positive control will produce a 270 bp fragment. Performing the Mycoplasma test is a necessary quality control for the correct conduct of experimental research.

Table 2.2. PCR reaction conditions for mycoplasma analysis.

PCR Condition		**Temperature (°C)**	**Time**
Initial Denaturation		94	1 min
35 cycles	Denaturation	94	30 sec
	Annealing	60	20 sec
	Extension	72	1 min
Final Extension		72	5 min

2.4. CELL CULTURE PROCEDURES

Cell Culture experiments were conducted in order to understand the effect of Dex-CeNPs on colon cancer cell lines via cytotoxicity assays, ROS scavenger analysis and flow cytometry analysis were performed.

2.4.1. Cytotoxicity (WST-1) Assay Procedure for Colon Cancer Cell Lines

WST-1 assay was performed to test the cytotoxicity properties of Dex-CeNPs and to determine IC50 values for each cell line. WST-1 (2 - (4 - iodophenyl)-3 - (4 - nitrophenyl)-5 - (2,4 - disulphophenyl)-2H - tetrazolium) test is the cleavage of the tetrazolium salt (WST-1) by cellular mitochondrial dehydrogenases to formazan. In this assay, the yellow tetrazolium salt is directly proportional to the number of viable cells turning dark red due to mitochondrial dehydrogenase activity. To determine viable cell amount, this colour change can be measured spectrophotometrically. Four sets of WST-1 experiments were carried out at different concentration ranges, to determine the cytotoxic behaviour of Dex-CeNPs and also the determination of IC50 values of each cell lines. Four initial concentrations between 100 and 1000 μg/mL range (100, 250, 500, 1000 μg/mL) were tested in the first set for all colon cancer cell lines. The second experimental set was performed with new concentration series depending on the obtained data from the first set. The purpose for performing the second test is to calculate the IC50 value accurately. Possible concentration ranges, which may include IC50 values were chosen in the second set.

The WST-1 experiment basically consisted of four main experimental steps. First, the seeding and incubation of cells for 24 hours, then treatment with Dex-CeNPs at determined concentrations and another 24 hours of incubation. Then the WST-1 protocol was conducted and measurements were taken at 450-650 nm on Day 1 and Day 3 following the treatment Day 0. Each set of experiments was performed in triple wells, each set was repeated three times. All data are presented as mean ± standard deviation.

The cells in the complete medium were seeded with a final concentration of 5000 cells/ 100 μL into 96-well plates at the beginning of the experiment. The 96 well plates then were incubated at 37°C, in a 5% CO_2 incubator for 24 hours. The Dex-CeNPs were diluted in a complete medium to a final concentration of 200, 500, 1000, and 2000 μg/mL at the end of the 24 hours of incubation. 100 μL of concentrated Dex-CeNPs were added directly to the 24 hours incubated 96-well plate. Final Dex-CeNPs doses in the wells therefore were 100, 250, 500, 1000 μg / mL with a 1:1 ratio. Cells without any treatment were used as a negative control group in addition to Dex-CeNPs treated samples. After the incubation of 24 hours and 72 hours with Dex-CeNPs treatment, 200 μL of media+ Dex-CeNPs were removed and 100 μL of a WST-1 reagent (1:10 ratio with cell culture media) was added to each well and

incubated for 2 hours. At the end of incubation, absorbance values of the cells were measured at 450 /650 nm range via using Cytation™ 5 Cell Imaging Multi-Mode Reader.

An additional WST-1 assay was conducted with narrowed down concentration ranges in addition to the first concentration series, to calculate accurate IC50 values for colon cancer cell lines. The concentration range was varied according to synthesis and cell line type, even though the same dilution principle was used. Table 2.3 lists the concentration ranges of SD1 and SD2 for colon cancer cell lines.

Table 2.3. Concentration range of Dex-CeNPs (SD1 and SD2) for colon cancer.

Cell Lines	SD1 (µg/mL)	SD2 (µg/mL)
DLD-1	700, 750, 800, 850, 900, 950, 1000	100, 125, 150, 175, 200, 225, 250
COLO 201	250, 275, 300, 350, 400, 450, 500	100, 125, 150, 175, 200, 225, 250
LoVo	1000, 1100, 1250, 1400, 1500, 1750, 2000	500, 550, 600, 750, 800, 900, 1000
HT-29	500, 550, 600, 750, 800, 900, 1000	500, 550, 600, 750, 800, 900, 1000
SW48	2000, 3000, 5000	2000, 3000, 5000

2.4.1.1. pH-dependent Cytotoxicity Assay of Colon Cancer Cell Lines

After obtaining the first WST-1 Assay set with high concentration requirement, the idea of change in pH in the environment may affect the concentration increase. All the concentrations for each cell line (DLD-1 and COLO 201) were determined regarding the first set of WST-1 Assay experiment results. To perform pH adjustment, first, 5000 cells were seeded in 96 well plates per well in a 100 µL medium and incubated for 24 hours.

After the pH meter was calibrated, preparation of 2.5 mL of nanoparticle concentrations of 2000 µg/mL, 1000 µg/mL, 500 µg/mL, and a blank medium was prepared in a non-sterile environment. 2 mL of the medium was added to the concentrations, 500 µL space was allowed for and acetic acid and medium to adjust pH. The pH solution was adjusted to pH 6 and pH 7.

2.4.1.2. Half Maximal Inhibitory Concentration (IC50) Calculation

The most widely used value to measure drug efficacy is half-maximal inhibitory concentration (IC50). The IC50 values for each cell line exposed to Dex-CeNPs in this study were calculated depending on cytotoxicity results, which were obtained through the WST-1 assay with using Graph-Pad Prism 5.0.

2.4.2. Reactive Oxygen Species (ROS) Measurements

During regular physiological processes, ROS act as signalling molecules in cells, the formation of ROS however may also result in damage to a variety of cellular organelles and activities, thus impairing normal physiology. It is an assay for determination of ROS production in the cells effected by both Dex-CeNPs. Firstly, cells were seeded in 96-well plates in a total 100 µg/mL total medium per well. After 24 hours of attachment and incubation, the cells were treated with 100, 250, 500, and 1000 µg/mL of Dex-CeNPs.

2 ', 7'- Dichlorofluorescein Diacetate (DCFDA) was used to measure cellular H_2O_2. The old medium was vacuumed after 24 hours of treatment with Dex-CeNPs, and each well washed once with 1xPBS. 100 µL DCFDA+medium mixture was added to the wells at 10 µM DCFDA per millilitre. The plates were incubated at 37ºC and 5% CO_2 for 45 minutes away from light. The absorbance of each well was measured in 485/535 nm range by Cytation™ 5 Cell Imaging Multi-Mode Reader at the end of the 45 minutes.

2.4.3. Flow Cytometry Analysis

To perform flow cytometry, colon cell lines were seeded in 6-well plates with 500.000 cells/well seeding density and incubated 24 hours. At the end of incubation, each cell line was treated with three different concentrations including IC50 values, lower concentrations and higher concentrations of SD2. The reason why the experiments we conducted with SD2, is the high concentrations required for the IC50 values of SD1 for each cell line in other sets of experiments. therefore, Flow cytometry experiments were conducted on SD2 synthesis only.

After 24 hours incubation with the media, the old media was transferred to the FACs tubes from 6-well plates. The attached cells were washed with 1xPBS. 250 µL/well of Trypsin-EDTA 1X (0.25%) solution was added to the plates and incubated for 5 minutes at 37 °C in 5% CO_2 incubator. De-attached cells were collected with 750 µL of media, approximately 500 µL of media+cell mixture transferred to 1mL Eppendorf tubes and counted with Trypan Blue while the rest of the cells were transferred into the Falcon tubes. Falcon tubes were centrifuged at 1300 rpm for 5 minutes. The supernatant was vacuumed. Pellet was dissolved in a required amount of media and transferred to FACs tubes, centrifuged for 5 min at 1300 rpm. The supernatant was discarded and then 1 mL of PBS-FBS buffer (1xPBS and 2% FBS) was added to the tubes and centrifuged again for 5 min at 1300 rpm. After the centrifugation, the supernatant was vacuumed. 100 µL of Binding/Annexin Buffer was added to the tubes. According to the number of counted cells, Pacific Blue Annexin V and PI dyes were added to the tubes at a ratio of 1:2 respectively. It was incubated in the dark for 15 minutes. 100 µL of Binding/Annexin Buffer and analysis was performed on the FacsCanto II Flow Cytometer. All obtained results were evaluated with FlowJo V10 program.

2.4.4. Statistical Analysis

All of the data was evaluated via two-way Anova Statistical programs. The Graph-Pad Prism 5.0 (GraphPad Software, San Diego, CA, USA) statistical program was used to evaluate the data obtained because of this study with the appropriate analysis method. One-way analysis of variance (one-way ANOVA) was used to compare group data. A value of $p<0.001$ was accepted as statistically significant.

3. RESULTS

This chapter contains the results of both the characterization and cell culture experiments for Dex-CeNPs in the following sections.

3.1. SYNTHESIS AND CHARACTERIZATION OF DEX-CeNPS

By using two types of Dextran (Dextran from *Leuconostoc mesenteroides* with molecular weight in between 9-11kDa (Sigma, Cat#D9260) (D1), Dextran *Leuconostoc spp* with 6 kDa molecular weight, (Sigma, Cat#31388) (D2), two Dex-CeNPs syntheses (SD1, SD2) were synthesized and their UV-Vis Spectroscopy, DLS, FTIR, XRD, TEM, XPS and TGA as material characterization methods were performed to define properties of synthesized Dex-CeNPs.

3.1.1. Synthesis Strategy of Dex-CeNPs

The first indicator to determine successful Dex-CeNPs synthesis is the change in color during the synthesis process. To visualize color change during synthesis, each synthesis was followed up for 18 hours, in which two crucial time points at the beginning (1 hour) and at the end (18 hours) were recorded. Various Dex-CeNPs with color change turning from yellow to brown have been reported in the literature until now. In case of SD1 and SD2, similar color change was also observed. With SD1, a bright yellow color was observed at the end of 1 hour, following the color turning to dark brown at the end of synthesis (Figure 3.1a, left). Expecting the dark yellow color at 1 hour and bright yellow at 18 hr., SD2 had different color change than SD1 (Figure 3.1b, left). Similar color results were reported by *Yazici et al.*, and *Perez et al.* [79, 94].

3.1.2. Characterization of Dex-CeNPs

Nanoceria was successfully coated with two different dextran molecules (SD1 and SD2). The characterization of the synthesized Dex-CeNPs was performed via UV-Vis spectroscopy, DLS, FTIR, TEM, Raman, XRD, XPS and TGA analyses.

3.1.2.1. Ultraviolet-Visible (UV-Vis) Spectroscopy

UV-Visible Spectra was conducted at the wavelength range of 200-800 nm with different dilution ratios for each synthesis. The UV-Vis Spectra results gives an overall information about oxidation states (Ce^{+4} and/or Ce^{+3}) in the Dex-CeNPs according to its peak shape and peak maxima as visualized in Figure 3.1. However, XPS data gives us more quantitative information about the Ce^{+4} / Ce^{+3} ratio. Characteristic UV-Vis Spectra peaks were observed broad peak in between 260 nm to 360 nm for each synthesis. However, peak maxima of 275 nm UV- Vis profile showed minimal differences among SD1 (275 nm) and SD2 (287 nm).

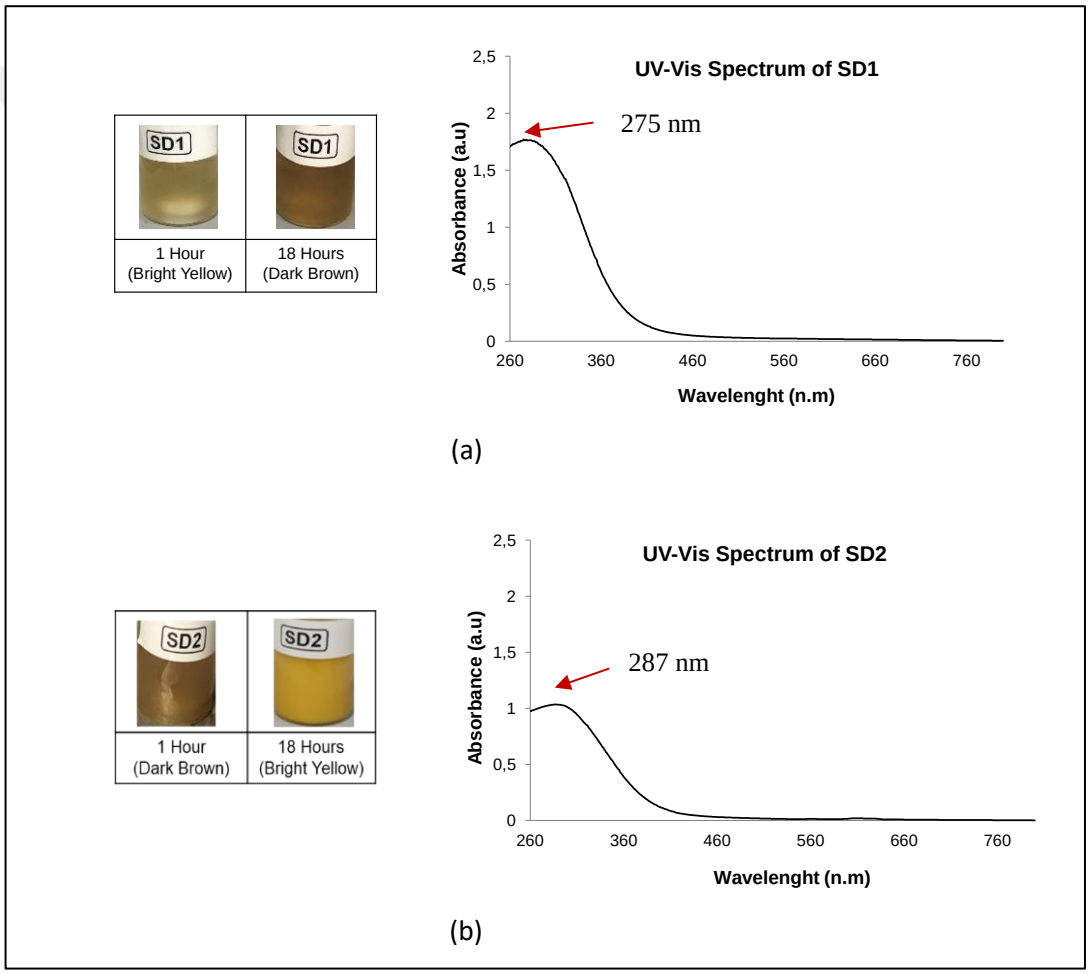

Figure 3.1. The colour change during synthesis of (a) SD1 from 1 hour to 18 hours (left) and UV-Vis spectrum of SD1 (right) (b) colour change during synthesis of SD2 1 hour to 18 hours (left) and UV-Vis spectrum of SD2 (right).

3.1.2.2. Dynamic Light Scattering (DLS) Measurement

Following UV-Vis Characterization, DLS measurement was conducted to evaluate particle size and surface charge properties via zeta potential measurements of Dex-CeNPs (SD1, SD2) in Figures 3.2a and 3.2b. The size distribution of syntheses was varied. Whereas the hydrodynamic diameter of SD1 was around 10±0.34 nm with 30% intensity ratio while SD2 was around 18±0.4 nm with 25% intensity ratio as shown in Figure 3.2a. The polydispersity index (PDI) values of SD1 and SD2 were 0.318 and 0.430 respectively, which was an indicator of their quality with respect to their size distributions. As it was visualized in Figure 3.2b, zeta potential of SD1 and SD2 were measured as -0.029 and 0.0756 respectively. While SD1 had slightly negative surface charge, SD2 had slightly positive surface charge.

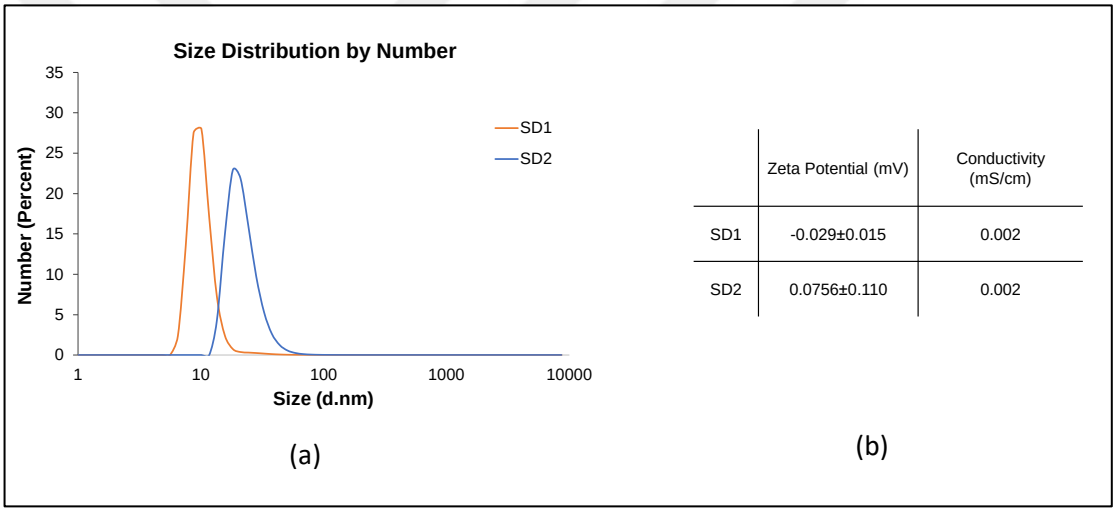

	Zeta Potential (mV)	Conductivity (mS/cm)
SD1	-0.029±0.015	0.002
SD2	0.0756±0.110	0.002

Figure 3.2. DLS and zeta potential measurements of Dex-CeNPs. (a) size distribution by number and (b) zeta potential values of SD1 and SD2.

3.1.2.3. Attenuated Total Reflectance-Fourier Transform Infrared (ATR-FTIR) Spectroscopy

After UV-Vis and DLS Characterization, all compounds were characterized by ATR-FTIR spectroscopy. For the ATR measurements a multi reflection horizontal ATR unit was used. Dextran (D1, D2), Cerium doped dextran (SD1, SD2) and the doping agent Ce $(NO_3)_3.6H_2O$ were characterized via ATR-FTIR spectroscopy. Additionally, the doping reaction process was conducted without doping agent yielding undoped USD1 and USD2 (denoted in the graphs as SD1 w/o Ce $(NO_3)_3.6H_2O$) samples for comparison.

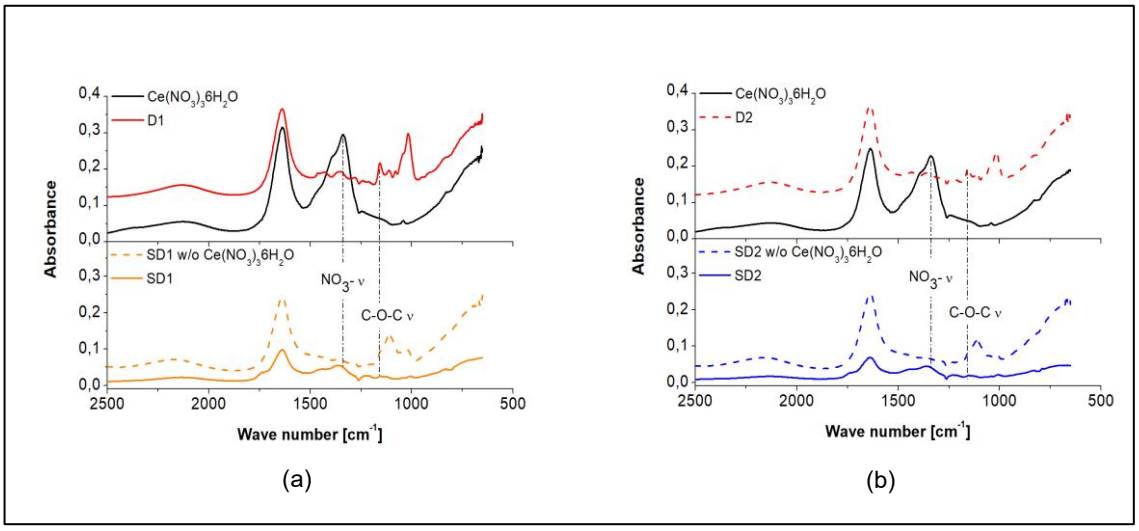

Figure 3.3. ATR-FTIR spectra of Dex-CeNPs. (a) SD1 and (b) SD2.

ATR spectra of the dextran D1 and D2 were shown in top of both graphs (red and red dashed) of the Figures 3.3(a-b). The FTIR profiles of both dextran showed similar spectra and the expected bands of the IR sensitive vibration modes in the molecules were observed. A broad band from 3500 to 2500 cm^{-1} which is not shown in the graph corresponds to H-bonded OH vibration modes and water vibration modes. Hence, it is not possible to detect the hidden C-H vibration modes of dextran hidden under this intense vibration. The expected C-O-C vibration modes of the glycosidic bridge between saccharide unit were detected at 1158 cm^{-1}. ATR-FTIR spectra of the doping agent $Ce(NO_3)_3.6H_2O$ were represented in top graphs (black lines) of the Figure 3.3(a-b). The characteristic nitrate ion (NO_3^-) vibration mode appeared as a broad band from 1470 to 1250 cm^{-1} range. The orange line at the bottom of 3.3a represents doped SD1 whereas the orange dashed line belongs to spectra of the products of same process without $Ce(NO_3)_3.6H_2O$ addition (USD1). The blue line at the bottom of 3.3b represents doped SD2 whereas the blue dashed line belongs to spectra of the products of same process without $Ce(NO_3)_3.6H_2O$ addition (USD2). The presence of vibration modes which belong to NO^-_3 ions and disappearance of absorption bands between 1000 and 1250 cm^{-1} of the C-O-C vibrations indicates successful dextran coating of both syntheses.

3.1.2.4. Raman Spectroscopy

The graphic of SD1 and D1 in the spectral region of 100 to 3100 cm^{-1} was given in Figure 3.4A. Raman spectra of both D1 and D2 had characteristic bands were parallel to literature [95]. Band at 714 cm^{-1} of SD2 was observed unlike SD1. The band of SD1 at 1036 cm^{-1}

shifted to 1050 cm^{-1} on the SD2 spectrum and got more intense which can be described as second-order longitudinal optical (2LO) Mode which corresponds to oxygen vacancy site presence [96]. Except for these differences, both syntheses had similar Raman patterns as seen in Figure 3.4(a-b). The fingerprint band of Nanoceria at approximately 460 cm^{-1} [97] which indicates the symmetrical stretching mode of Ce-O vibration, didn't appear because of the surface coating with Dextran. This shows that Cerium Oxide was coated with dextran successfully.

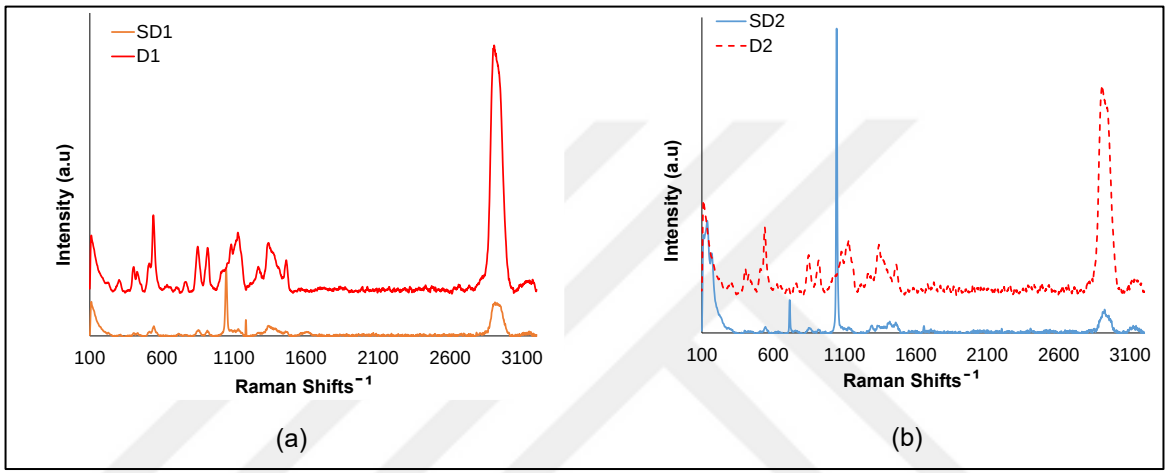

Figure 3.4. Raman spectra of SD1 and SD2. (a) Raman spectra of SD1 and D1, (b) Raman spectra of SD2 and D2.

3.1.2.5. High Resolution Transmission Electron Microscopy (TEM)

HRTEM characterization gave the information about the core diameter of Dex-CeNPs. The core diameter of both syntheses did not exceed 5 nm as shown in Figure 3.5. Although the core diameters of SD1 and SD2 were similar with minimal difference, the differences in hydrophilic diameter of SD1 (8-10 nm) and SD2 (30-60 nm) which obtained from the DLS data are due to the dextran coating on their surfaces. No considerable agglomerates and aggregates were observed during the analysis.

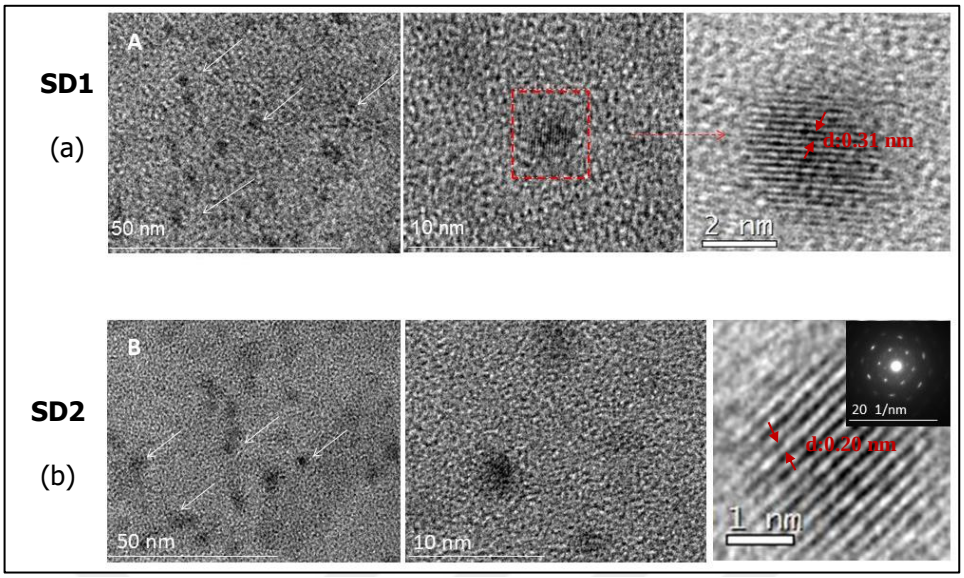

Figure 3.5. TEM characterization of Dex-CeNPs. (a) SD1 and (b) SD2.

3.1.2.6. X-Ray Diffraction (XRD)

In addition to obtained data from TEM characterization, the powder X-ray diffraction (XRD) pattern analysis demonstrated characteristic diffraction peaks of cubic core Cerium Oxide nanoparticles inside the Dextran coating. XRD pattern of both syntheses had (111), (220), (311) and (331) planes which indicates face centered cubic (FCC) structure also confirmed by HRTEM analysis.

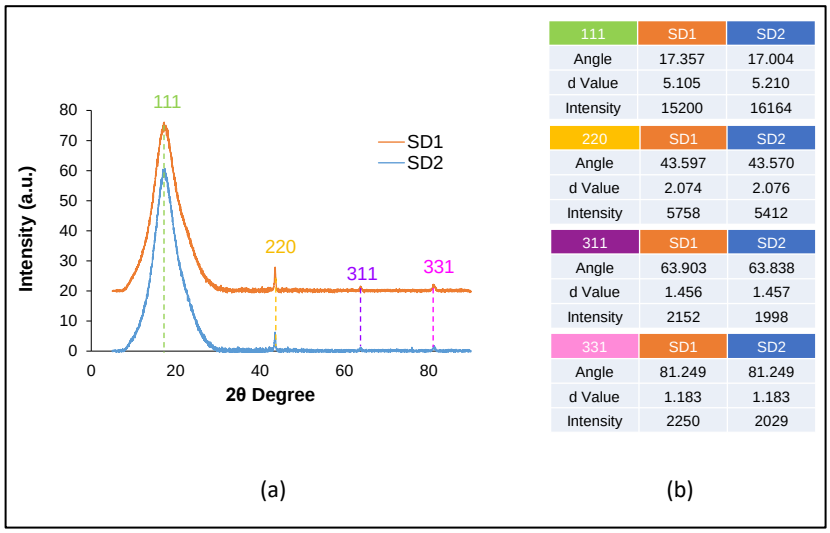

111	SD1	SD2
Angle	17.357	17.004
d Value	5.105	5.210
Intensity	15200	16164
220	SD1	SD2
Angle	43.597	43.570
d Value	2.074	2.076
Intensity	5758	5412
311	SD1	SD2
Angle	63.903	63.838
d Value	1.456	1.457
Intensity	2152	1998
331	SD1	SD2
Angle	81.249	81.249
d Value	1.183	1.183
Intensity	2250	2029

Figure 3.6. XRD results of SD1 and SD2. (a) XRD patterns (b) angle, intensity and d value table of both Dex-CeNPs.

3.1.2.7. X-Ray Photoelectron Spectroscopy (XPS)

The separated XPS spectra for the Ce^{3+} and Ce^{4+} states of SD1 and SD2 were given in Figures 3.7a and 3.7b, respectively. The peaks obtained at 881.9, 898.0, 900.5 and 906.4 eV were compatible with presence of Ce^{4+} state, while the peaks at 885.8 and 903.6 eV indicated to presence of Ce^{3+} state. While both synthesis contained Ce^{3+} and $Ce^{4+,}$ the (Ce4+/ Ce3+) % ratio for SD1 was calculated as (66.7 /33.3) % respectively. For SD2, the (Ce4+/ Ce3+) % ratio was determined as (40.8/ 59.2).

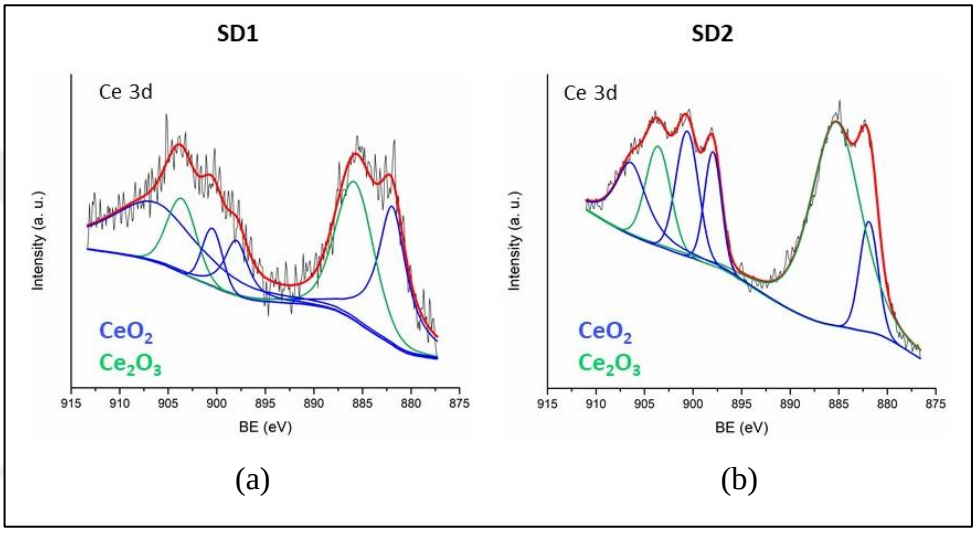

Figure 3.7. XPS spectra of SD1 and SD2. (a) XPS spectra of SD1, (b) XPS spectra of SD2.

3.1.2.8. Thermogravimetric Analysis (TGA)

Thermal stability of both syntheses (SD1 and SD2) was determined via thermogravimetric analysis (TGA) between 25 and 825 °C range with gradually heating 10 °C per minute. The whole procedure took 80 minutes to perform. In Figure 3.8 the TGA plots of SD1 and SD2 respectively demonstrating the five-stage decomposition pattern on the TGA plot of SD1. First stage of SD1 was initiated by a weight loss of ~14% between 25 to 197 °C which is attributed to the water evaporation, the second stage contributes a weight loss of 54% at 204 °C also attributed to the degradation of dextran, the third stage shows weight loss of 72% at 313 °C, and final stage showed 89% weight loss up to 825 °C. SD2 decomposition profile consisted of three-stages, with the initial stage starting with a 11% weight loss between 25 and 182 °C, the second stage contributes a maximum weight loss of 90% from 182 to 235 °C, and at the third stage 96.7% of weight loss at 420–825 °C was observed.

In conclusion, first stage of both Dex-CeNPs can be attributed due to the excess amount of water and/or moisture dehydration. As seen in Figure 3.8, the results indicated first two-step weight loss process occurred for both Dex-CeNPs up to maximum 235 °C with minimal differences. The initial ~11% weight loss started in between 25 and ~182 °C for both Dex-CeNPs, which indicated to the removal of adsorbed water in the crystalline structure of Cerium Oxide. SD1 lost ~89% of its weight while SD2 lost ~97% of its weight at 825 °C. This indicated that SD2 had more immobilized Dextran around than SD1 [98]. Which can be imply that SD2 was more stable than SD1.

It can be decided from all these characterization results of SD1 and SD2 that, although their structures are similar, physicochemical properties have differences. Their biological activity in vitro affected by these differences, which will be discussed in the following sections.

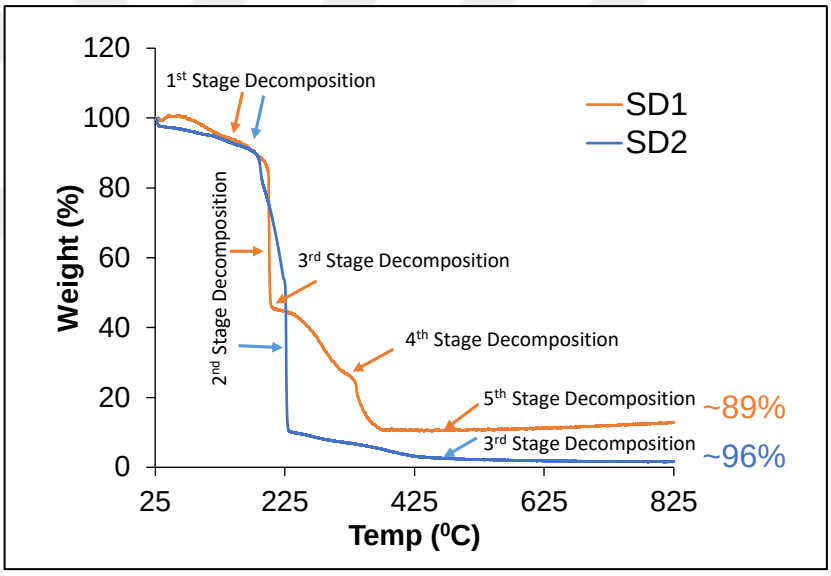

Figure 3.8. TGA plots of SD1 and SD2.

3.1.2.9. Stability of Dextran-Coated Nanoceria

Stability of nanoparticles is important as its physiochemical properties which can be influenced by various factors such as light, radiation, moisture, pH, temperature, ionic strength, density and other factors that come from a microenvironment. Without any proper characterization, handling and storage circumstances of nanoparticles, it can cause various random and uncertain properties which is not possible to detect easily between each synthesis, resulting in different responses in vitro studies as the synthesis changes.

Change in the microenvironment and environment in which the synthesis process is carried out and stored can cause sensitive changes through Van der Waals, Columbic forces, and electrostatic interactions can be regulated and stabilized by surface functionalization. Also, the addition of chemicals that can stabilize the ionic strength along with pH environment instabilities. To overcome these obstacles CeO_2 nanoparticles were coated with dextran and to determine the stability of SD1 and SD2, UV-Vis, DLS and zeta potential measurements were conducted up to 6 months. UV–Visible spectrophotometry of nanoceria provides us quantitative information about the change in oxidation states of Ce. The decrease in the absorbance values of the peak corresponding to Ce^{4+} indicates the decrease in concentration of Ce^{4+} on the surface of nanoceria. The decrease in concentration of Ce^{4+} directly indicates an Spectrophotometry experiments, DLS and Zeta potential were performed to determine the increase in concentration of Ce^{3+} as the surface of nanoceria. Following to UV-Vis change in size and charge properties of two syntheses (SD1 and SD2).

Initially, the UV-Vis Spectrum of SD1 was observed over a 6-month period at different time intervals, during this period, the change in absorbance unit and wavelength maxima were evaluated according to UV-Vis Spectrophotometry data. These two crucial parameters inform us about the Ce^{4+}/Ce^{3+} ratio on the Dex-CeNPs surface. In case of SD1 synthesis, the absorbance units for all time points increased compared to Day 0, containing some minor fluctuations on Day 14 and month 2. Unit of absorbance at 260 nm Day 0 (1.6 a.u.), Day 7 (3.35 a.u.), Day 14 (2.5 a.u.), Day 21 (3.2 a.u.), Day 28 (3.35 a.u.), 2 months (2.1 a.u.), 4 months (4.5 a.u), 6 months (4.5 a.u) was observed. After the month 4, it was detected that the absorbance of Dex-CeNPs was saturated. This increase in absorbance units indicates an increase in Ce^{4+} on the Dex-CeNPs surface. Peak maximums for each time point were recorded as 287 nm for Day 0, 288 nm for Day 7 and 14, 289 nm for Day 21, 286 nm for Day 28, 287 nm for Day 60, 120 and 180. The variation between the peak maximums only changed by 2nm over the 6-month period. No shift was observed for days 60, 120, 180 compared to day 0.

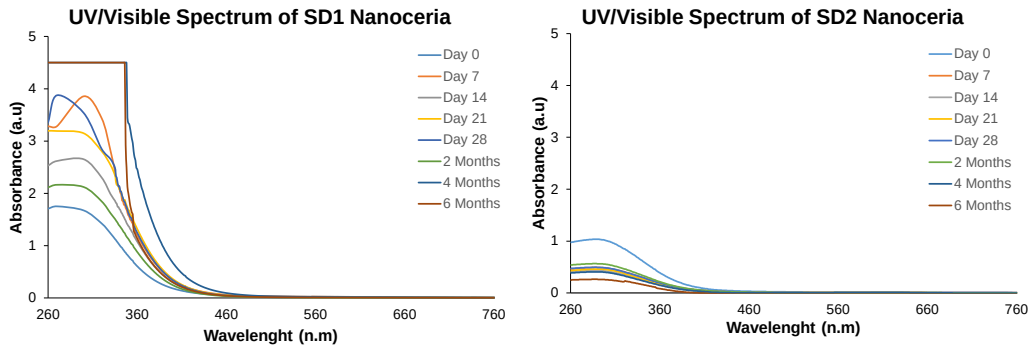

(a)

(d)

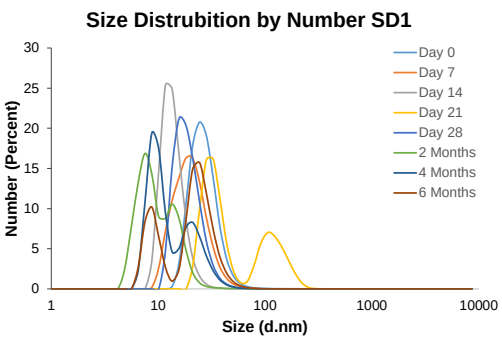

(b)

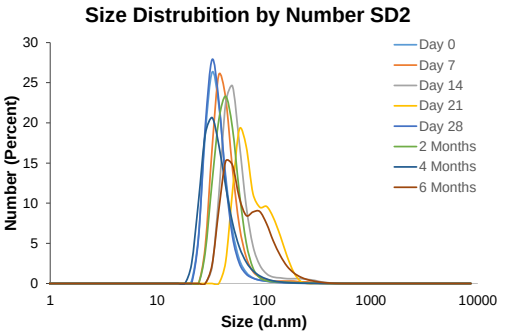

(e)

SD1	Zeta Potential (mV)	Zeta Deviation (mV)	Conductivity (mS/cm)
Day 0	-0.029	0.015	0,002
Day 7	0.030	0.001	0,004
Day 14	-0.214	0.195	0,001
Day 21	-0.018	0.044	0,012
Day 28	-10.13	0.39	0,017
2 Months	-15.38	0.110	0.532
4 Months	-20.43	1.684	0.466
6 Months	-6.24	0.492	4.400

(c)

SD2	Zeta Potential (mV)	Zeta Deviation (mV)	Conductivity (mS/cm)
Day 0	0.0756	0.110	0,002
Day 7	-0.0007	0.0409	0,006
Day 14	-0.252	0.264	0,020
Day 21	-0,024	0.025	0,012
Day 28	-20.98	0.940	0,001
2 Months	-28.93	0.787	0.365
4 Months	-31.91	0.346	0.408
6 Months	-17.01	0.947	4.063

(f)

Figure 3.9. 6- month period stability analysis of Dex-CeNPs (SD1 and SD2) via UV-Vis spectroscopy and DLS. (a) UV-Vis spectrum of SD1, (b) DLS analysis of SD1, (c) zeta potential analysis of SD1, (d) UV-Vis Spectrum of SD2.

Following the UV-Vis Spectrophotometry of SD1, the size distribution and zeta potential measurements were conducted. Following the UV-Vis Spectrophotometry of SD1, the size distribution and zeta potential measurements were conducted. One broad peak between 10-100 nm was observed with similar 20%- 25% intensity on Day 0, Day 7, and Day 14 of synthesis. On Day 21, two peaks were observed with different intensities. The intense peak is around 10-100 nm range with 15%, another minor peak was around 100 nm with 7% intensity. A single intense peak was observed in between the 10 and 100 nm range on Day 28. All observations indicate that Day 21 was a critical time point in terms of the equal size distribution for SD1 synthesis. Fundamentally, the size distribution of SD1 at different time points was in the same range with similar intensity and peak shape until the size diversity and fluctuations started to appear with two peak characteristics on day 21. (Figure 3.9a and 3.9b).

SD1 was also evaluated in terms of surface charge at the parallel time intervals for UV-Vis and DLS measurements. SD1 was mainly negatively charged with a similar surface charge (-0.029/-0.018 mV) as Day 0, Day 7, Day 14, and Day 21. An initial drastic decrease in the surface charge of Dex-CeNPs started on Day 28 approximately a hundred times lower (-10.13 mV) than the charge value observed from Day 0 to Day 21. Zeta potential values were continuously decreased for up to 4 months. Although there was a sharp increase at month 6, the surface charge of SD1 was generally negative. All primal characterization data indicate us Day 21 is the most crucial time point for the stability of SD1.

The same stability procedure was applied to SD2 as well. Firstly, UV-Vis spectra were conducted for 6 months period. The absorbance units showed decreasing profile during 6 months period compared to Day 0. The obtained 0. 97 absorbance unit at 260 nm was on Day 0. The total fluctuation in absorbance units from Day 7 to Month 4 was approximately 0.5 a.u. The drastic absorbance drop was observed at 6 months as the 4-fold difference (0.25 a.u.) compared to Day 0. The decrease in absorbance units indicates an accumulation of Ce^{3+} on the surface of Dex-CeNPs. The peak maxima for each time point changed by 2 nm from day 0 to month 6. Overall, no considerable peak maxima shift was observed during the 6 months of the period.

By evaluating the size and charge properties of nanoceria for 6 months periods as SD1, SD2 stability has also been analyzed. For mostly all-time points except Day 21 and 6 months with 20-30% intensity interval, SD2 has narrow peak profiling in 10-100 nm range. Except Day

21 and 6 months, the peaks mostly were overlapped at 30-60 nm size range with one narrow major peak. The size of dextran-coated nanoceria was 30 nm and 38 nm range with the same 25% intensity respectively on Day 0 and Day 7. The peak was shifted to 50 nm size with 25% intensity on Day 14. The major pick was around 50 nm range with 20% intensity, whereas minor peak was around 106 nm with 10% intensity on Day 21. Day 28 and Day 0 had similar size properties including size (33 nm) and peak intensity (28%). On the Months 2 and 4 respectively, nanoceria was around 44 nm and 33 nm in size with 23% and 20% intensity. 6 months two peaks were observed. The minor peak was observed around 92 nm with 8% intensity and the major peak was around 44 nm with 15% intensity.

The Dex-CeNPs charge properties were followed for 6 months through Zeta potential measurement as SD1. On Day 0, SD2 was positively charged (0.0756 mV). It showed negatively charged profiling starting at Day 7 however, and its negatively charged properties were very similar in between the time period of Day 7 and Day 21. For the charge properties a sharp decrease (20-fold, -20.98 mV) on Day 28 has been observed. The obtained decrease from day 0 continued gradually until month 4. With lower value than 4 months the charge properties of SD2 were negative on 6 months (-17.01 mV).

Although there was not any remarkable change over the 6 months period in terms of size properties of SD2, after 21 Days significant change in size properties of nanoceria was observed. 21 Days was therefore the critical time point for SD2 stability. To conclude that, UV-Vis spectra gave us the increase of Ce^{4+} on the surface of SD1, while the SD2 showed an increase of Ce^{3+} on its surface. Cancer drug candidates can show different properties between them and these differences are caused by the various mechanisms of action derived from both syntheses. The size features of SD1 and SD2 on the other hand are slightly different. SD1 has a smaller size range (8-33 nm) and vary over 6 months compared to SD2 with its larger size range (30-60 nm). However, the variation in size properties of SD2 did not vary over the period of 6 months. Over 6 months period the charge profiling of SD1 and SD2, which was mostly negative charge had similar profiles. The critical time point for each synthesis was the 21^{th} Day.

3.2. DEX-CeNP AS A DRUG CANDIDATE FOR COLON CANCER

Cellular-based assays such as cytotoxicity, reactive oxygen species (ROS), and flow cytometry analysis were performed on Dex-CeNPs treated colon cell lines. Following, pH-dependent cytotoxicity experiments were conducted depending on the data that was observed via initial cytotoxicity experiments. This will be discussed in the following sections.

3.2.1. Cellular Impact of Dex-CeNPs (SD1 and SD2) Against Colon Cancer

The colon cancer cell lines for this study were selected according to three main criteria; EGFR expression level, mutation type, and MSI Status. In most common cancer types including colon cancer, EGFR expression level is inversely linked with prognosis due to mutation or overexpression. In addition to EGFR expression levels, KRAS, TP53, SMAD4, PIK3CA, APC, BRAF, and CTNNB1 mutations are potential prognostic and predictive markers, as well as targets for pharmacological intervention. Besides, Microsatellite instable (MSI) tumors have always been associated with an improved prognosis and Microsatellite stable (MSS) tumours generally do not respond to immunotherapies.

Table 3.1. Mutation types and MSI status in colon cancer cell lines.

Cell Type	EGFR Expression Level	Mutation Type	MSI Status
DLD-1 (ATCC,CCL-221)	Wild type	**PIK3CA:**p.Glu545Lys (c.1633G>A);p.Asp549Asn (c.1645G>A) **KRAS:** p.Gly13Asp (c.38G>A) **TP53:** p.Ser241Phe (c.722C>T) **APC:** p.Arg2166Ter (c.6496C>T)	MSI
COLO 201 (ATCC,CCL-224)	Wild type	**APC:**p.Thr1556Asnfs*3 (c.4666dupA) (c.4666_4667insA) **BRAF:** p.Val600Glu (c.1799T>A) **CTNNB1:**p.Asn287Ser (c.860A>G)	MSS
LoVo (ATCC,CCL-221)	Wild type	**KRAS:** p.Gly13Asp (c.38G>A) **APC:**p.Arg1114Ter (c.3340C>T)	MSI
HT-29 (ATCC,HTB-38)	Wild type	**TP53**: p.Arg273His (c.818G>A) **BRAF:** p.Val600Glu (c.1799T>A) **APC:** p.Glu853Ter (c.2557G>T); p.Thr1556Asnfs*3 (c.4666dupA); (c.4666_4667insA) **SMAD4:** p.Gln311Ter (c.931C>T)	MSS
SW48 (ATCC,CCL-231)	Mutant	**EGFR**: p.Ser492Arg (c.1476C>A) **APC**: p.Arg2714Cys (c.8140C>T) **CTNNB1**: p.Ser33Tyr (c.98C>A)	MSI

Among selected colon cancer cell lines in this study, HT-29 cell line was determined as a reference cell line due to its wild-type EGFR, BRAF, APC and SMAD4 mutations. The DLD-1 cell line has a KRAS, TP53 and APC with one point mutation while PIK3CA with two-point mutations. EGFR is wild type in the COLO 201 cell line, it has a point mutation in the CTNNB1 and BRAF gene as well as duplication and insertion mutation in the APC gene. There is one point mutation in the KRAS and APC gene in the LoVo cell line. In the SW48 cell line, there are one-point mutations in the EGFR, APC and CTNNB1 genes. As for the colon cancer cell line signature features, MSI status (microsatellite instability status) were important to understand its effect on the response of these cell lines when treated with Dex-CeNPs. All the cell lines that were used in this study are shown in Table 3.1.

Before freezing and during cell culture experiments, mycoplasma analysis was performed and confirmed with two different methods. E-Myco™ Mycoplasma PCR detection kit was used to determine mycoplasma contamination before the cells were frozen to avoid risk of tank contamination and cross contamination risk for the other cell lines which remain in the tank. MycoAlert™ PLUS Mycoplasma Detection Kit was used for every 3rd-4th passage of the cells in order to prevent any lab contamination. PCR products on Agarose Gel image (Figure 3.10a) and quantitative mycoplasma results (Figure 3.10b) are shown in Figure 3.10.

In Figure 3.10a, the appearance of the 160 bp internal control and positive bands indicates that the PCR is working properly. Five different cell lines were tested and despite no band for any cells and negative control were observed, at 270 bp band was appeared in the positive control as expected which shows no mycoplasma contamination was detected on analyzed cell lines. In Figure 3.10b, B/A (substrate / background ATP) ratio of each colon cancer cell lines were less than 0.8 which indicated no mycoplasma contamination was detected for each cell line.

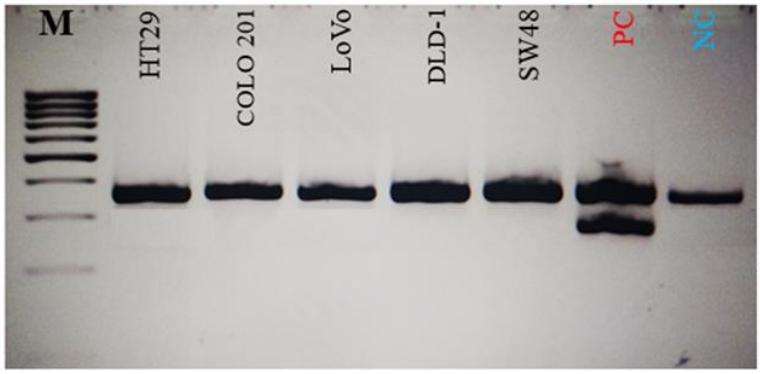

(a)

Cell lines	A	B	B/A	Contamination State
HT-29	124	32	0.2	CLEAN
COLO 201	170	60	0.3	CLEAN
LoVo	95	63	0.8	CLEAN
DLD-1	377	108	0.3	CLEAN
SW48	154	110	0.7	CLEAN

(b)

Figure 3.10. Mycoplasma detection results of colon cancer cell lines. (a) agarose gel image of PCR products, (b) MycoAlert™ PLUS mycoplasma detection kit contamination results.

3.2.1.1. Determination of Dex-CeNPs Concentration Ranges

In order to understand the cytotoxic effects of SD1 and SD2 five initial concentrations were determined according to the previous studies and WST-1 assay was performed for five colon cancer cell lines to precise evaluation of Half-Maximal Inhibitory concentration (IC50) value.

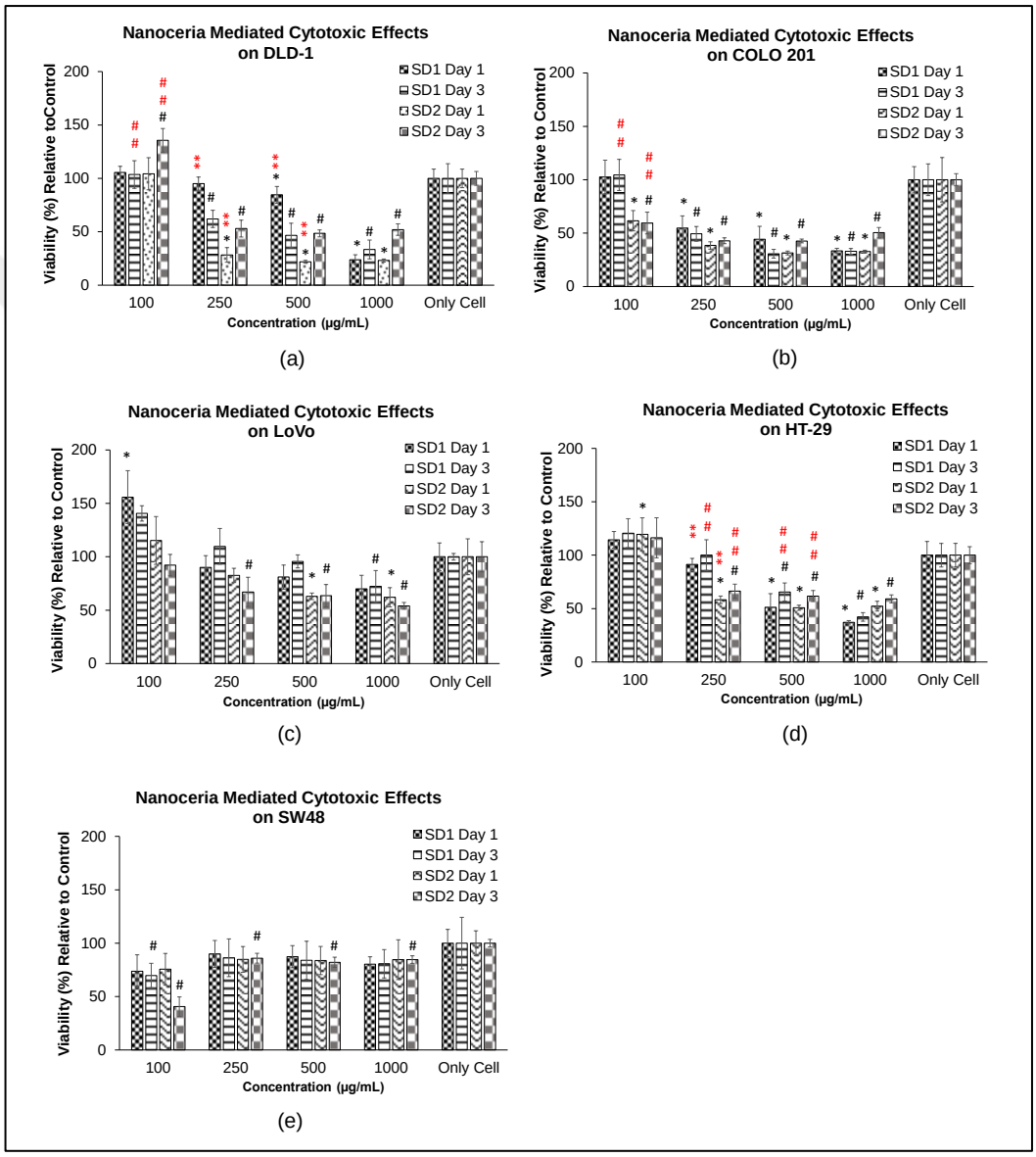

Figure 3.11. Cytotoxic properties of two Dex-CeNPs (SD1 and SD2) against (a) DLD-1, (b) COLO 201, (c) LoVo, (d) HT-29, (e) SW48 cell lines at 100, 250, 500, 1000 µg/mL concentrations after 1 and 3 days of treatment. * Represents comparison between SD1 control group and each concentration (p-value≤0.001), # Represents comparison between SD2 control group and each concentration.(p-value≤0.001), ** Represents comparison between SD1 and SD2 at the same concentration. (p-value≤0.001), ## Represents comparison between SD1, Day3 and SD2, Day3 at the same concentration (p-value≤0.001).

Figure 3.11a indicates the cytotoxic properties of SD1 and SD2 against DLD-1 cell line. Day 1 at 100 μg /mL did not show any toxicity in either synthesis. While no change was observed in SD1 synthesis in Day 3 compared to Day 1, 30% increase in viability was observed in SD2 synthesis compared to Day 1 in Day 3. For 250 μg /mL concentration, SD1 did not show any toxicity on Day 1, while SD2 synthesis reduced cell viability by 70% on the same day compared to control group. On the Day 3 of the same concentration, SD1 showed approximately 40% toxicity, it was observed that the viability for SD2 increased by 20% compared to Day 1 and the toxicity decreased to 50%. While a negligible decrease in viability was observed for SD1 synthesis at 500 μg /mL concentration, severe (80%) viability decrease was observed in SD2 synthesis on Day 1. In contrast to the large viability difference at Day 1, the Day 3 toxicities of the two syntheses were parallel to each other. The toxicity profile at 1000 μg/mL, which was determined as the highest concentration, was approximately 80% with a sharp decrease for SD1 compared to 500 μg /mL. Toxicity for SD2 did not show any change compared to 500 μg /mL. However, the toxicity of both syntheses at this concentration was the same for Day 1. On Day 3 of 1000 μg /mL, SD1 showed 70% toxicity, while this rate was 50% for SD2. As Figure 3.11a shows, each Day 3 of SD2 synthesis increased compared to Day 1 for each concentration. In addition, approximately 50% toxicity was observed on Day 3 at concentrations of 250 μg /mL, 500 μg /mL and 1000 μg /mL.

Figure 3.11b indicates the cytotoxic properties of SD1 and SD2 against COLO 201 cell line. line, SD1 synthesis at a concentration of 100 μg/mL did not show any toxicity for Day1 and Day 3, while SD2 synthesis showed a toxicity of approximately 40% for both time points compared to control group. SD1 toxicity at 250 μg /ml concentration increased on Day 1 compared to 100 μg/mL and cell viability decreased to 54%. SD2 toxicity is around 60% on the same day and concentration. On the 3rd day of the treatment, both synthesis profiles were similar to the Day 1 toxicities. The toxicity of both syntheses was observed below 50% at a concentration of 500 μg/mL. No significant difference was observed between their toxicity at the two time points in either synthesis. An increase in cell viability was observed on Day 3 in SD2 synthesis with the same concentration, which was also observed in the DLD-1 cell line (Figure 3.11a), but this increase was not as significant for the COLO 201 line as in the DLD-1 line. Toxicity for SD1 at a concentration of 1000 μg/mL was approximately 70% at both time points. While 70% toxicity was observed for SD2 on Day 1, this rate decreased to

50% on Day 3. The increased viability profile for SD2 on Day 3 was seen in the COLO 201 line as well as in DLD-1.

In Figure 3.11c represents cytotoxic properties of SD1 and SD2 against LoVo cell line. No toxic effects were observed at a concentration of 100 µg/mL. On the contrary, on Day 1, an increase in cell viability by 50% for SD1 and 15% for SD2 was observed compared to the control group. These increases may be due to the presence of free dextran in solution and its uptake by cells is thought to increase their viability. At a concentration of 250 µg/mL, 10% and 20% toxicity were observed in the SD1 and SD2 syntheses for Day 1, respectively, compared to the control group. For day 3, SD1 viability increased by 10% compared to the control group, while SD2 viability decreased by approximately 30%. Up to 80% viability in SD1 synthesis was observed for Day 1 at a concentration of 500 µg/mL, while at the same concentration the viability was 60% for SD2. Day 3 toxicities for both syntheses showed no significant differences from Day 1 toxicities. Even at the highest concentration of 1000 µg/mL, no significant toxic effect was observed for SD1, and cell viability was observed at approximately 70% at both time points. However, cell viability was observed approximately 60% on Day 1 for SD2, compared to 50% for Day 3 compared to control group. In contrast to the DLD-1 and COLO 201 line, no increase in viability was observed at any concentration at Day 3 of SD2 synthesis in the LoVo line.

Figure 3.11d represents the cytotoxic properties of SD1 and SD2 against the HT-29 cell line. As the concentration increased on Day 1, the toxicity level of SD1 increased significantly. No toxicity was observed on Day 1 and Day 3 for SD1 at 100 µg/mL also slight increase compared to control group was observed. These increases in viability may be due to the presence of free dextran in solution and its uptake by cells causing a boost to their viability. 250 µg/mL had a similar trend of viability on Day 3, while a slight decrease (10%) in viability was obtained on Day 1. Initial significant cytotoxicity (49%) was achieved on Day 1 at 500 µg/mL. The 1000 µg/mL viability profile is about 63% for both time points. In the case of SD2, no change in viability was observed at Days 1 and 3 for 100 µg/mL compared to the control group. In contrast, initial significant cytotoxicity (42%) was achieved at 250 µg/mL on Day 1 and 34% on Day 3. At a concentration of 500 µg/mL, SD2 achieved exactly 50% toxicity on Day 1, while on Day 3 the toxicity was slightly reduced to 40%. This concentration trend observed at 500 µg/mL is the same for 1000 µg/mL. As a result, SD2 is more effective on HT-29 than SD1.

Figure 3.11e shows the cytotoxic properties of SD1 and SD2 against the SW48 cell line. In the SD1 state, mild toxicity (25%) was observed at a concentration of 100 µg/mL on Day 1 and 60% toxicity on Day 3. At concentrations of 250, 500 and 1000 µg/mL, SD1 slightly affects cytotoxicity (10% - 20%). In line with the cytotoxic behavior of SD1, SD2 also has 10-20% toxicity on Days 1 and 3 at all concentrations. In conclusion, the selected concentrations had no significant effect on SW48 except 100 µg/mL on Day 3 for both time points and were determined to require higher concentrations of treatment.

3.2.1.2. Determination of Higher Concentrations

Due to low cytotoxic effects of SD1 and SD2 on LoVo and SW48 as shown in previous WST-1 assay results (see Figure 3.11(c-e)) , the selected concentrations were readjusted as 500,1000, 1250,. 1500, 2000 µg/mL for LoVo and 500, 1000, 1250, 1500, 2000 µg/mL were exposed for SW48 cell lines and WST-1 assay was performed.

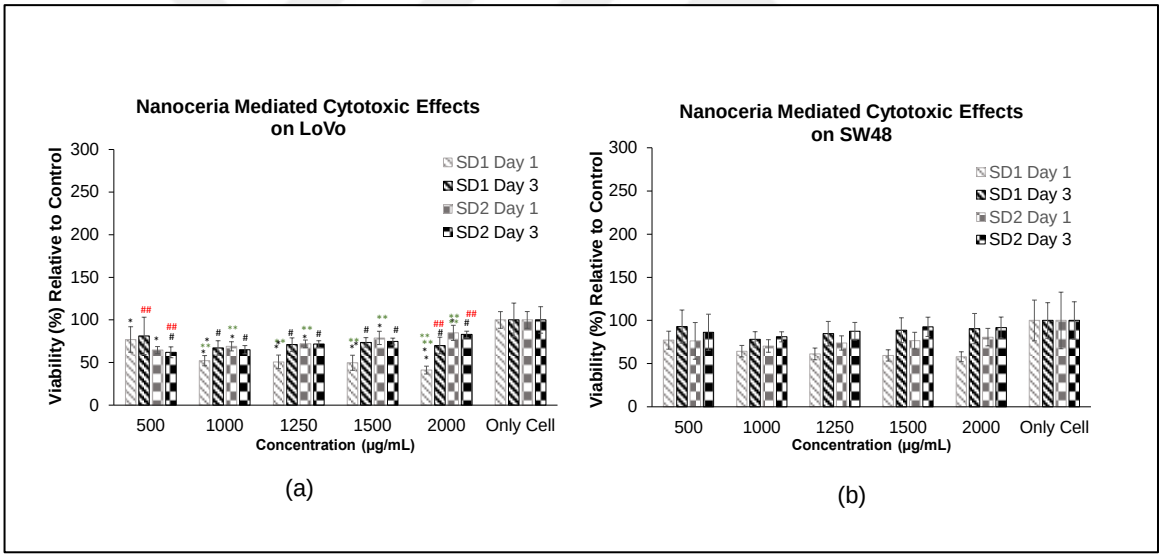

Figure 3.12. Cytotoxic properties of two Dex-CeNPs (SD1 and SD2) against, (a) LoVo, (b) SW48 cell lines at readjusted concentrations after 1 and 3 days of treatment. * Represents comparison between SD1 control group and each concentration (p-value≤0.001), # Represents comparison between SD2 control group and each concentration.(p-value≤0.001), ** Represents comparison between SD1 and SD2 at the same concentration. (p-value≤0.001), ## Represents comparison between SD1, Day3 and SD2, Day3 at the same concentration (p-value≤0.001).

In Figure 3.12a, the cytotoxic effects of SD1 and SD2 on LoVo cell line is represented. By regarding SD1, approximately 20% toxicity was obtained at 500 µg/mL on Day 1 and Day 3. At 1000 µg/mL, significant decrease on viability (48%) was observed on Day 1 whereas on Day 3, viability decreased by 25%. At 1250 µg/mL, 50% and 30% decrease on viability

was observed on Day 1 and Day 3 respectively. 1500 μg/mL indicated the same profile as 1250 μg/mL. At 2000 μg/mL, toxicity increased by 60% and the ratio between Day 1 and Day 3 remained same as it was observed for lower concentrations. In case of SD2, viability profile of all concentrations for each time points were similar and interestingly, the viability increased as the concentration increased. This profile can be explained as the saturation of the concentration on LoVo cells.

In Figure 3.12b the cytotoxic effects of SD1 and SD2 on SW48 cell line is represented. In case of SD1, only 20% increase on toxicity between the lowest (at 1500 μg/mL) and the highest (at 2000 μg/mL) concentraiton was observed on Day1. For SD2, 500 μg/mL and 1500 μg/mL has the same viability value (76%) on Day 1 and similar viability profile was observed for Day 3. As it was observed for SD2 on LoVo in Figure 3.12a, viability fluctuates between the concentrations and increased as the concentration increases for SW48 as well.

3.2.1.3. Determination of Narrowed Concentrations

After the first concentrations of SD1 and SD2 syntheses were given, the IC50 calculations made with GraphPad Prism were narrowed down in line with the intervals given by the program so that it was possible to determine the most accurate IC50 value.

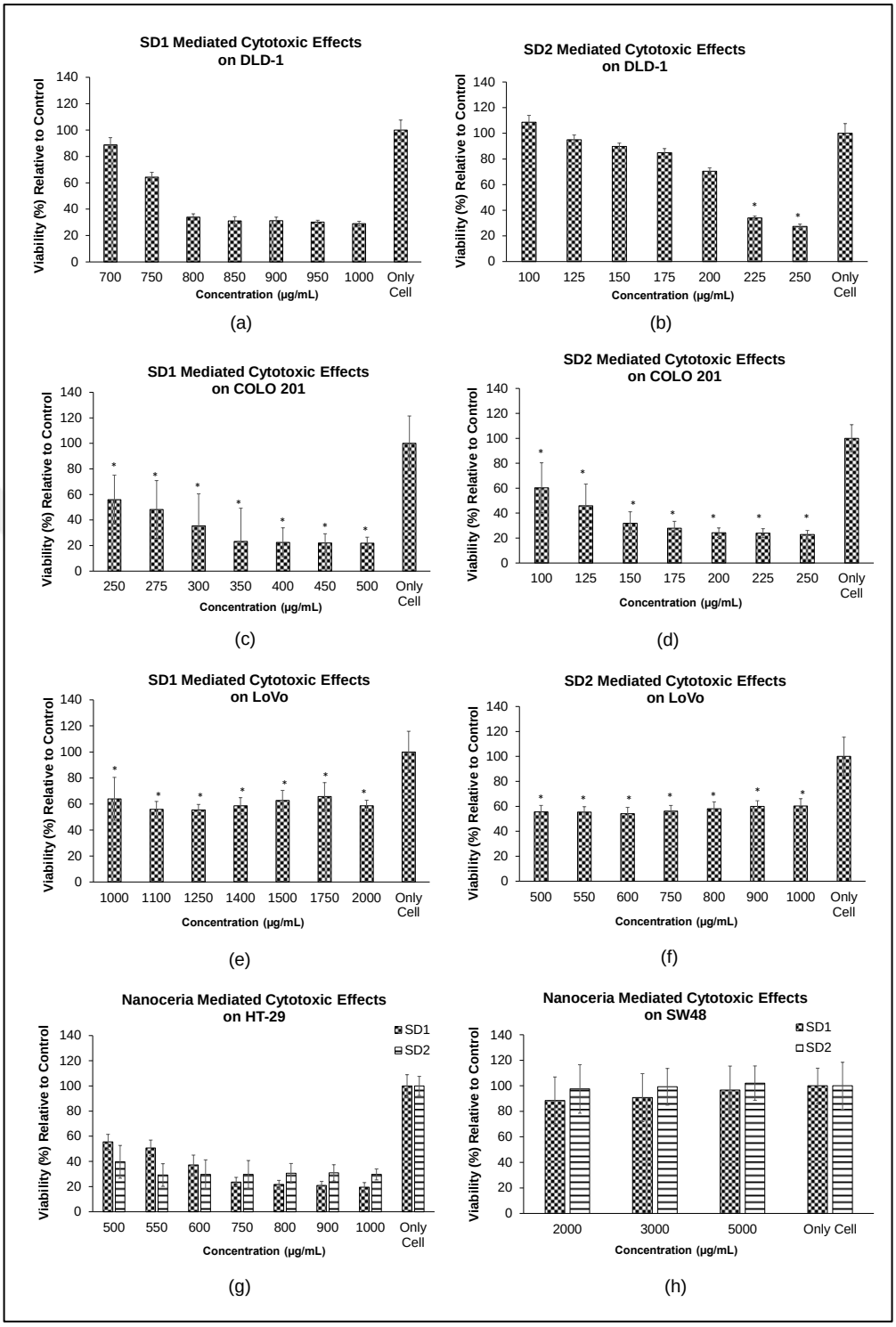

Figure 3.13. Cytotoxic properties of two Dex-CeNPs (SD1 and SD2) with narrowed concentrations. (a) DLD-1 with SD1, (b) DLD-1 with SD2, (c) COLO 201 with SD1, (d) COLO 201 with SD2, (e) LoVo w SD1, (f) LoVo with SD2 (g) HT-29 with SD1 and SD2, (h) SW48 with SD1. * Represents comparison between control group and each concentration (p-value≤0.001).

Figure 3.13a indicates SD1 cytotoxicity on DLD-1 cell line. As it was shown in Figure 3.11a, the IC50 value was in between 500 µg/mL and 1000 µg/mL. Therefore, narrowed concentrations were determined in order to find the best IC50 value. At a concentration of 700 µg/mL, cell viability was reduced by 22%. When increased to 750 µg/mL, toxicity increased to 40% compared with control and cell viability was observed 60%. Toxicity of approximately 70% was observed at all concentrations from 800 µg/mL to 1000 µg/mL.

Figure 3.13b indicates SD2 cytotoxicity on DLD-1 cell line. Narrowed concentrations for SD2 was less than SD1 as it was shown in Figure 3.11a. Hence, initial concentration for SD2 synthesis was 100 µg/mL. At 100 µg/mL to 150 µg/mL, almost no toxic effects were seen compared to the control group. 15% toxicity was detected at 175 µg/mL and 30% toxicity at 200 µg/mL. When the concentration of 225 µg/mL was reached, the toxicity profile increased drastically, reducing the viability rate up to 30% compared to the control. 250 µg/mL had the same toxicity profile as the 225 µg/mL concentration.

Figure 3.13c indicates the cytotoxic properties of SD1 against COLO 201 cell line. In case of SD1, 40% toxicity at 1250 µg/mL was observed while 50% toxicity was observed at 275 µg/mL. The least viability profile was observed at 500 µg/mL with 79% toxicity rate. The increase in concentration resulted with higher toxicity on COLO 201 cell line gradually.

Figure 3.13d indicates the cytotoxic properties of SD2 against COLO 201 cell line. In case of SD2, 40% toxicity at 100 µg/mL was observed while 55% toxicity was observed at 125 µg/mL. The increase in concentration resulted with more toxicity on COLO 201 cell line gradually which also obtained for SD1 (Figure 3.13c).

Figure 3.13e represents cytotoxic properties of SD1 against LoVo. The cytotoxic effect of SD1 on LoVo slightly from 1000 µg/mL to 2000 µg/mL in between 45% and 40% respectively. The toxicity profile showed fluctuations among concentrations.

Figure 3.13f represents cytotoxic properties of SD2 against LoVo. The cytotoxic effect of SD2 on LoVo varies minimally from 500 µg/mL to 1000 µg/mL in between 45% and 40% respectively. The toxicity profile decreased as the concentrations increased. As the concentration increased, as observed in the previous set of WST-1 Assay (Figure 3.12a), a slight difference in viability rate was obtained.

Figure 3.13g represents cytotoxic properties of SD1 and SD2 against HT-29 cell line. ~50% toxicity was obtained for SD1 at 500 μg/mL was obtained, as it was parallel to its previous cytotoxicity assay shown in Figure 3.11. At 600 μg/mL, approximately 60% toxicity was observed while significant toxicity (80%) observed from 750 μg/mL to 1000 μg/mL concentration. In case of SD2, similar profile was obtained for all concentrations with slightly more toxicity at 500 μg/mL. 550 μg/mL and 600 μg/mL concentrations. For higher concentrations, the toxicity profile reversed as SD1 became more toxic than SD2.

Figure 3.13h indicates the cytotoxic properties of SD1 and SD2 against SW48 cell line. Slight toxicity (10%) was observed at 2000 μg/mL and 3000 μg/mL concentration while no toxicity was observed at 50000 μg/mL depending on SD1 and no toxicity was observed for SD2 by regarding each concentration. In conclusion, selected concentrations exhibit no cytotoxic effect on SW48 including both syntheses.

After the first concentrations of SD1 and SD2 syntheses were given, the IC50 calculations made with GraphPad Prism were narrowed down in line with the intervals given by the program so that it is possible to determine the most accurate IC50 value.

3.2.1.4. IC50 Determination of Colon Cancer Cell Lines

The calculation of half-maximum inhibitory concentration (IC50) value is a major and informative measure of a drug's efficacy. It is an indication of the amount of required to inhibit the Colon Cancer's biological process by half.

The IC50 value calculations were performed by following the same procedure as described in Section 2.4.1.2. half maximal inhibitory concentration (IC50) calculation was shown at Table 3.2.

Table 3.2. IC50 values of colon cancer cell lines with respect to SD1 and SD2.

IC50 (μg/mL)	SD1	SD2
DLD- 1	745	215
COLO 201	232	124
LoVo	1242	623
HT-29	494	482
SW48	>5000	>5000

3.2.2. Cell Number Determination of Colon Cancer Cell Lines

Various cell densities (0,1000, 2000, 3000, 4000, 5000, 7500 and 10.000 cell per 96-well plate) were seeded first and then incubated for 24 hours to proceed with the WST-1 assay. At the end of incubation, absorbance value to versus to cell number were graphed. The straight-line formula was calculated for each cell line as shown in Figure 3.14. Depending on straight-line formula, all kinds of absorbance data can be converted to number of cell data.

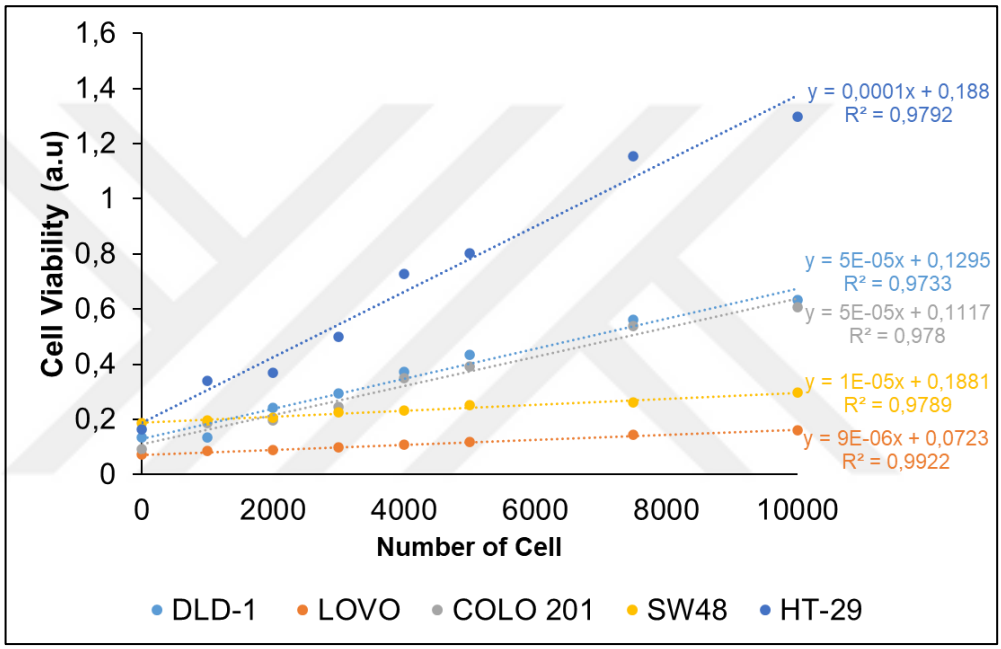

Figure 3.14. Cell viability of colon cancer cell lines.

3.2.3. Reactive Oxygen Species Generation of Dextran-coated Nanoceria on Colon Cancer Cell Lines

The data was calculated depending on fold increase in comparison with control group. One-fold was given to control group and the data for the other concentrations were calculated relative to the control group. While making fold-based calculation, two

methodologies were followed. One is direct comparison with WST-1 absorbance data and ROS absorbance, the second way is conversion of WST-1 data to number of cell data and compare to ROS absorbance data. In the following section, ROS formation based on fold difference of dextran-coated nanoceria for each colon cell lines were shown.

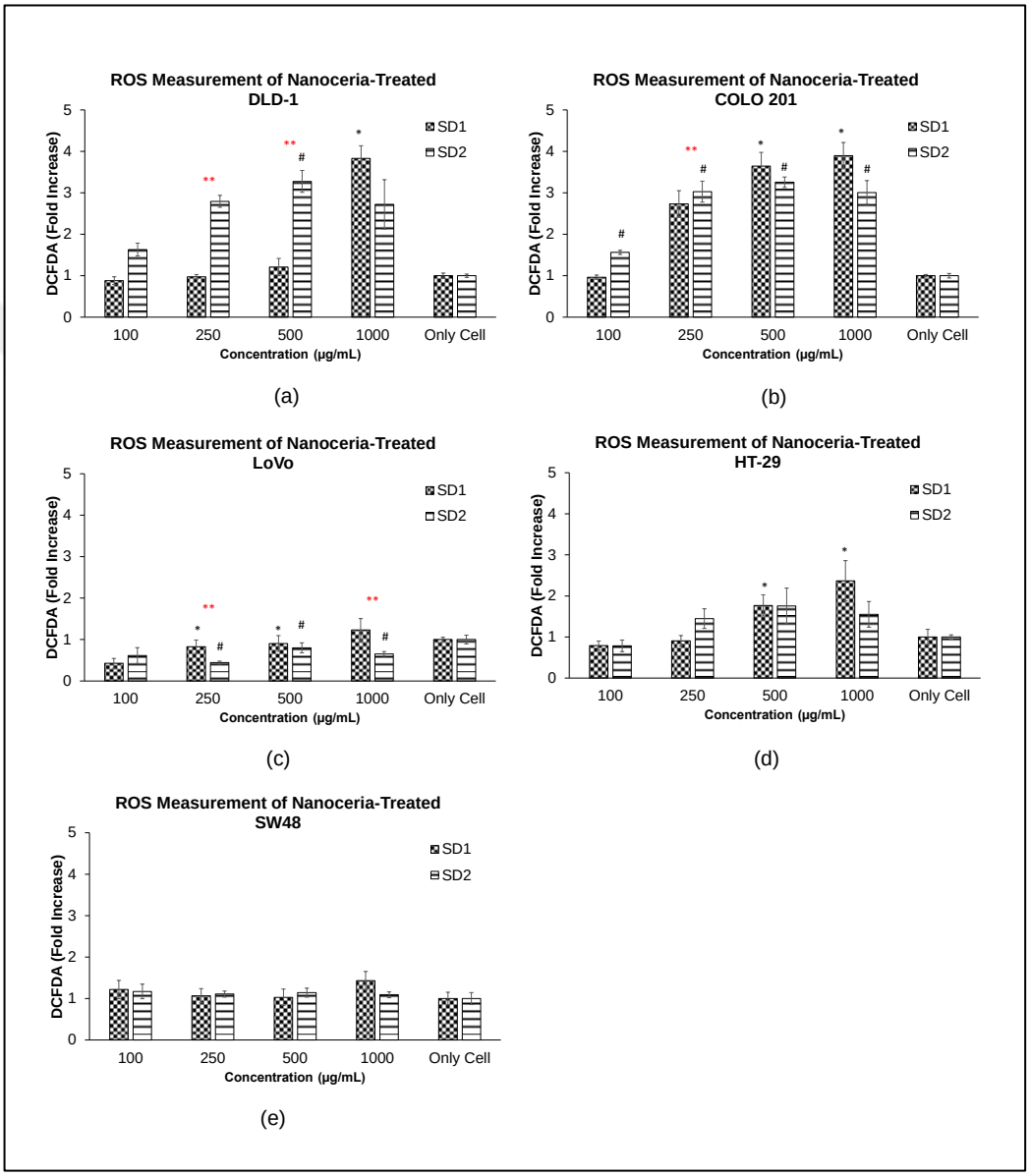

Figure 3.15. ROS formation based on two Dex-CeNPs (SD1 and SD2). (a) DLD-1, (b) COLO 201, (c) LoVo, (d) HT-29, (e) SW48. * Represents comparison between SD1 control group and each concentration. (p-value≤0.001) # Represents comparison between SD2 control group and each concentration. (p-value≤0.001)** Represents comparison between SD1 and SD2 at the same concentration. (p-value≤0.001)

In Figure 3.15a represents ROS formation based on fold difference after one-day treatment of SD1 and SD2 against DLD-1. In case of SD1, ROS generation is same with the control group for 100 µg/mL concentration. At 250 µg/mL concentration, approximately same ROS formation was observed with respect to control group. Also, similar ROS generation profile was detected at 500 µg/mL concentration compared to control group. On the contrary, prominent increase (4X) on ROS formation was obtained by 1000 µg/mL. In case of SD2, ROS generation showed an increasing trend from the initial concentration to 500 µg/mL. Hence, 1-fold drop was obtained at 1000 µg/mL compared to SD1. At 100 µg/mL, SD2 has approximately 1.5-fold ROS formation value compared to control group. However, roughly 2-fold difference in between two syntheses is shown. At 250 µg/mL, SD2 has 3X higher ROS generation compared to control group and approximately 1-fold difference in between SD1 and SD2 detected. At 500 µg/mL, SD2 had 3.2-fold higher ROS formation with respect to the control group. Besides, SD2 has 2X-fold more ROS formation compared to SD1 at the same concentration. At 1000 µg/mL, SD2 had approximately 3X more ROS generation with respect to control group. Therefore, 1X less ROS formation compared to SD1 was observed. In conclusion, among all concentrations, only significant difference in ROS generation was observed at 250 µg/mL and 500 µg/mL in between SD1 and SD2.

In Figure 3.15b represents ROS generation based on fold difference after one-day treatment of SD1 and SD2 against COLO 201. At a concentration of 100 µg/mL the ROS formation is similar with the control group by regarding SD1. At 250 µg/mL SD1 had 3-fold more ROS generation with respect to control group. At 500 µg/mL, SD1 showed 4-fold ROS formation compared to control and 1-fold difference regarding 250 µg/mL. The highest ROS formation among all concentrations were at 1000 µg/mL with a 4-fold difference compared to control group regarding SD1. No drastic ROS formation for all concentrations was obtained for SD2. The effect of SD2 on COLO 201 cell line was 1.5-fold more than control group at 100 µg/mL while 3-fold ROS formation differences compared to control group at 250, 500 and 1000 µg/mL concentration was observed. In conclusion, ROS generation profile of SD1 was more than SD2 on COLO 201 cell line.

In Figure 3.15c, represents ROS generation based on fold difference after one-day treatment of SD1 and SD2 against LoVo, among all concentrations, only 1000 µg/mL had

approximately 1.5-fold ROS formation concerning the control group while the other concentrations had lower formation compared to the control group related to SD1. SD2 did not trigger the ROS formation on any of concentrations. All concentrations had lower ROS generation than the control group. In conclusion, both SD1 and SD2 has no effect on LoVo cell line.

In Figure 3.15d, represents ROS formation based on fold difference after one day treatment of SD1 and SD2 against HT-29. The effect of SD1, Initial considerable ROS formation of SD1 against HT-29 was observed at 500 μg/mL with approximately 2-fold increase compared to control group. This ratio increased to 2.5-fold as the concentration increased to 1000 μg/mL. Below these concentrations (100 and 250 μg/mL), no ROS formation for SD1 was observed. In case of SD2, ROS formation profile was similar to SD1. On contrary, 1000 μg/mL had 1.5-fold lower ROS generation compared to SD1. Also, 250 μg/mL had 1.5-fold higher ROS generation regarding control group.

In Figure 3.15e, represents ROS formation based on fold difference after one-day treatment of SD1 and SD2 against SW48. By regarding the effect of SD1, initial ROS formation was observed at 1000 μg/mL with 1.5-fold ROS generation increase compared to control group and below this concentration, ROS formations remained similar as the control group. In case of SD2, all concentrations showed similar ROS formation profile with respect to control group.

3.2.4. Flow Cytometry Analysis

In this section, death effect of Dex-CeNPs against colon cancer cell lines were analyzed. Flow cytometry experiments were continued with SD2 synthesis, which was effective at lower concentrations, since SD1 synthesis required high concentrations as observed for previous experiments. Concentrations of SD2; IC50 value along with a lower and a higher concentration value of IC50 concentration were chosen among the five initial concentrations.

Table 3.3. Diagrammatic representation of the expected flow cytometry results.

PB Annexin V	PB Annexin V^+ / PI^- Early Apoptosis Stage	PB Annexin V^+ / PI^+ Late Apoptosis Stage
	PB Annexin V^- / PI^- Healthy Stage	PB Annexin V^- / PI^+ Necrosis Stage
	PI	

Flow cytometry analysis was used to determine PB Annexin V binding and PI uptake in each colon cancer cells. Annexin is a protein that is found on the surface of cells and is involved in several biological processes, including cell death, inflammation, and blood clotting. Annexin can be detected using a specific annexin-binding dye, such as PB Annexin V. When the annexin-binding dye is added to a sample containing cells, it binds to the annexin protein on the surface of the cells. It is preferable to work with annexin because it is a marker of early apoptosis, or programmed cell death, and can be used to identify cells that are undergoing or are at a risk of undergoing apoptosis [99]. PI uptake is important in flow cytometry analysis because when a cell's membrane is damaged or compromised, it becomes permeable to PI, which can enter the cell and bind to the DNA within the nucleus. This binding results in fluorescence that can be detected by the flow cytometer, allowing researchers to identify cells with damaged membranes [100]. It can help understanding the health and viability of the cells being analysed, and can provide insights into various biological processes such as cell proliferation, differentiation, and apoptosis (programmed cell death) [101]. In each figure, lower left which is PB Annexin V^- and PI^-represented healthy cells, upper left quadrant which is PB Annexin V^+ and PI^- referred to early apoptosis stage, upper right which is PB Annexin V^+ and PI^+ demonstrated late apoptosis stage, and lower right quadrant PB Annexin V^- and PI^+ represented cells in necrosis stage.

For DLD-1 cell lines, while non treated cells show % 96 viability (Figure 3.16a) 100 µg /mL showed approximately 3% Late and early apoptosis with slightly decrease in cell health (6%) (Figure 3.16b). When treated with 215 µg /mL (IC50 Value) the rate of healthy cells decreased by 85% and 77% rate late apoptosis was observed (Figure 3.16c). As 250 µg /mL concentration is close to IC50 value, drastic decrease in healty cells by 70% and 65% late apoptosis was observed (Figure 3.16d). As it was shown in the Figure 3.16, after 100 µg /mL treatment, according to FSC-A (forward scattering area) / SSC-A (side scattering area) graph, granularity of the cells increase due to the apoptosis stage. At all concentrations, no significant changes in early apoptosis and necrosis was observed. To evaluate the quantity analysis, ANOVA test was applied for significancy and standard deviation of all concentrations were given at Table 3.4.

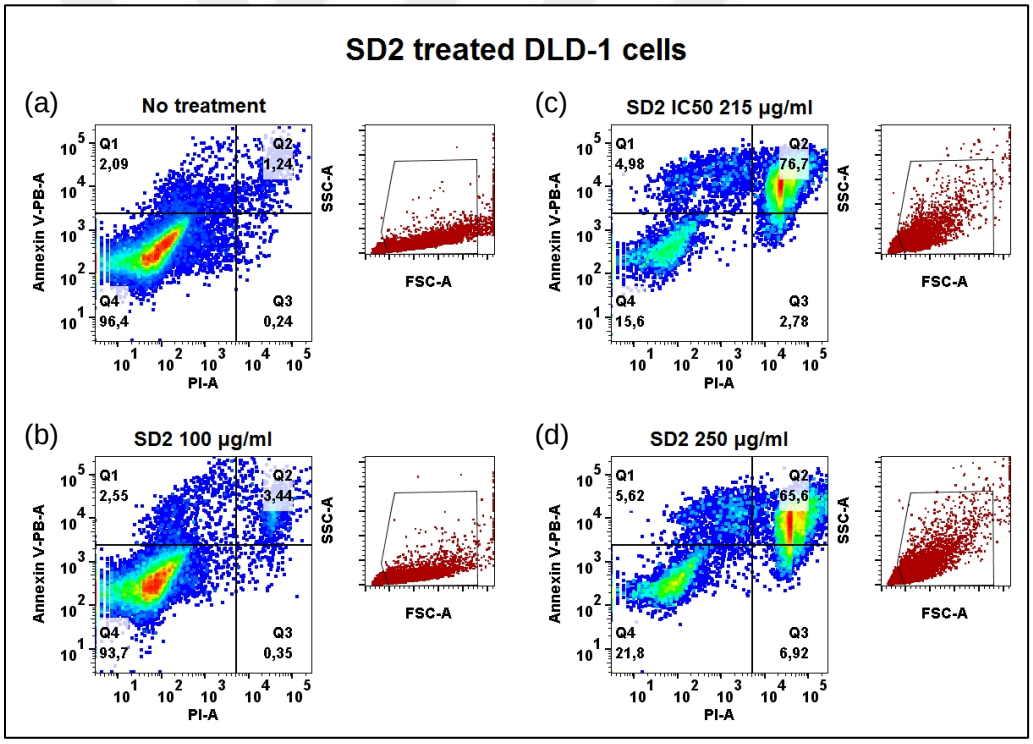

Figure 3.16. Effect of Dex-CeNPs (SD2) on apoptosis profile of DLD-1 cells. (a) no treatment, (b) 100 µg /mL, (c) 215 µg /mL and (d) 250 µg /mL Dex-CeNPs treatment.

Table 3.4. The percentage of DLD-1 cells corresponding to each apoptotic level (mean ± sd).

		Healthy	Early Apoptosis	Late Apoptosis	Necrosis
No treatment		95,88% ± 1,7%	1,29% ± 0,69%	2,36% ± 1,95%	0,46% ± 0,26%
SD2	*100 µg/ml*	90,54% ± 8,36%	1,32% ± 0,87%	6,56% ± 6,32%	1,61% ± 1,78%
	215µg/ml (IC50)	29,38%±30,28% ***	8,66% ± 6,52%	54,58% ± 29,9% ***	5,33% ± 8,45%
	250 µg/ml	9,83% ± 8,48% ***	8,04% ± 3,63%	78,74% ± 7,58% **	3,39% ± 2,34%

Two-way ANOVA test with Tukey correction across each row is used to indicate statistical significance in relation to the control group (* P<0.05, ** P<0.01, *** P<0.001).

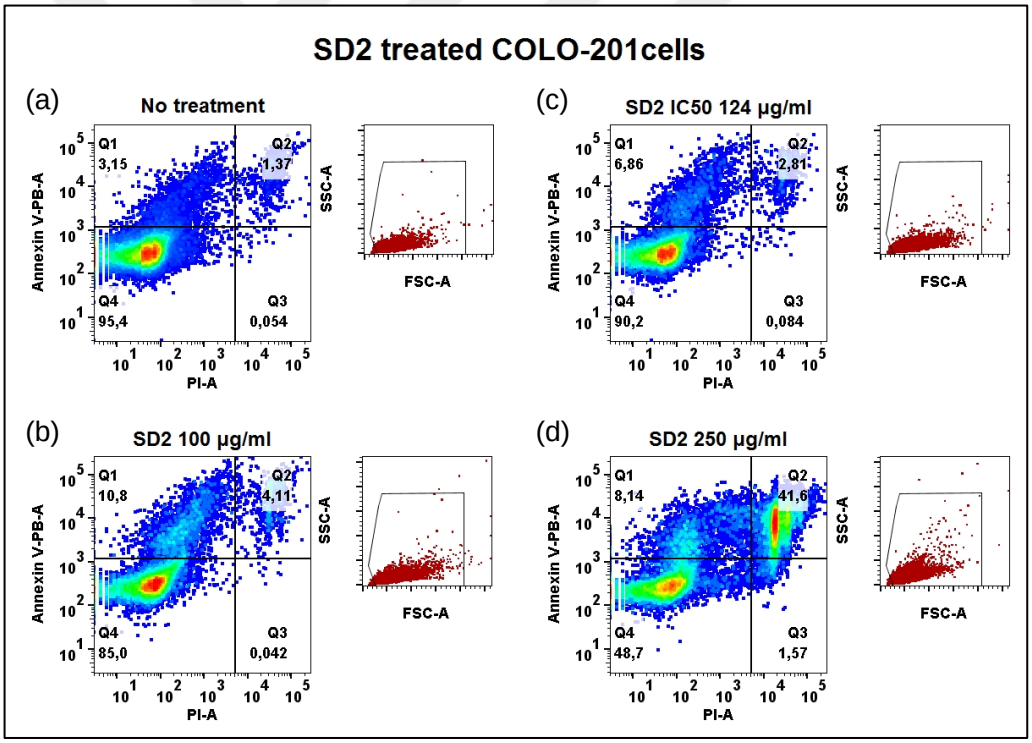

Figure 3.17. Effect of Dex-CeNPs (SD2) on apoptosis profile of COLO 201 cells. (a) no treatment, (b) 100 µg /mL, (c) 124 µg /mL and (d) 250 µg /mL Dex-CeNPs treatment.

For COLO 201, cell health profile was approximately 96% (Figure 3.17a), similar to DLD-1 (see Figure 3.16) and HT-29 (See Figure 3.19) cell lines. It had a similar profile as DLD-1 at a concentration of 100 µg /ml, with 85% health. This shows that the cells are slightly affected by the given concentration (Figure 3.17b). However, no considerable health

change was observed at the 124 µg /mL (IC50 Value) ratio, which is very close to 100 µg/ml with 90% rate (Figure 3.17c). Different from these two lower doses, 250 µg /mL showed approximately 50% health and 40% showed late apoptosis (Figure 3.17d). There were no necrotic cells observed for all concentrations. Unlike DLD-1 and HT-29, the granularity started at the highest concentration for COLO 201 cell line. To evaluate the quantity analysis, ANOVA test was applied for significance and standard deviation of all concentrations (Table3.5.)

Table 3.5. The percentage of COLO 201 cells corresponding to each apoptotic level (mean ± sd).

		Healthy	**Early Apoptosis**	**Late Apoptosis**	**Necrosis**
No treatment		94% ± 1,44%	3,47% ± 0,45%	2,43% ± 1,08%	0,1% ± 0,03%
SD2	*100 µg/ml*	90,68% ± 2,67%	5,29% ± 1,71%	3,64% ± 1,6%	0,39% ± 0,45%
	124 µg/ml (IC50)	87,6% ± 4,1%	7,69% ± 2,8%	4,44% ± 1,6%	0,25% ± 0,29%
	250 µg/ml	63,7% ± 19,79% ***	8,51% ± 1,18%	26,71% ± 18,47% ***	1,09% ± 0,6%

Two-way ANOVA test with Tukey correction across each row is used to indicate statistical significance in relation to the control group (* P<0.05, ** P<0.01, *** P<0.001).

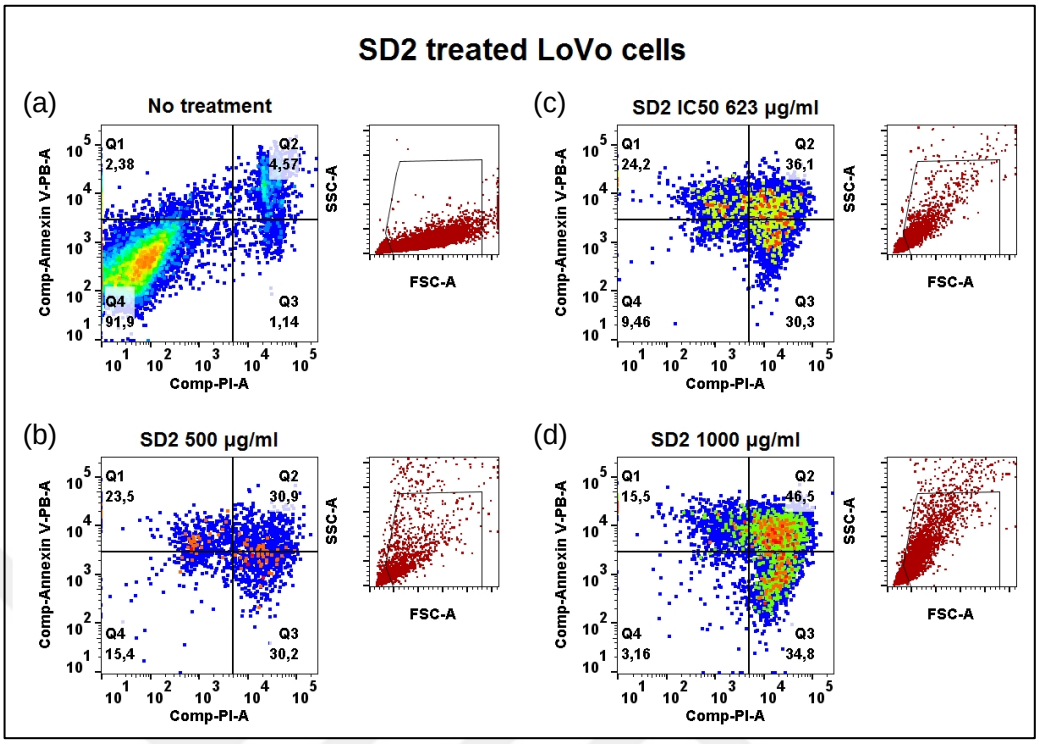

Figure 3.18. Effect of Dex-CeNPs (SD2) on apoptosis profile of LoVo cells. (a) no treatment, (b) 500 µg /mL, (c) 623 µg /mL and (d) 1000 µg /mL Dex-CeNPs treatment.

For LoVo, the cell health profile of untreated cells was considerably lower than other cell lines with 90% rate (Figure 3.18a). Cells treated with 500 µg/ml which was the lowest concentration for LoVo, showed approximately 15% health. As a result of this low health, late apoptosis and early apoptosis were 30% and 25% respectively. Unlike other lines, a necrosis rate of up to 30% was also observed (Figure 3.18b) which can be explained with the amount of clusters that this cell line is tend to be because of its nature and got damaged due to harsh pipetting and ultrasound bath. As the concentration increased, the cell health rate decreased at 623 µg /mL (IC50 value) by around 10%. Early Apoptosis at the rate of 25% and 40% of late apoptosis was observed. There was a considerable increase in late apoptosis stage with respect to 500 µg /mL was determined. The rate of Necrosis stage was parallel to 500 µg /mL (Figure 3.18c). At 1000 µg /mL, the healthy state of the cell was 3%. Late Apoptosis rate was around 50%, Early Apoptosis rate was 15% and necrotic cells were observed around 35%. The rate of necrotic cells was higher than the other concentrations (Figure 3.18d). The most granularity which can be estimated with the FSC-A (forward scattering area) / SSC-A (side scattering area) graph, seen at 1000 µg /mL

furthermore, granularity at 500 µg /mL was higher than 623 µg /mL. To evaluate the quantity analysis of LoVo cells, ANOVA Test was applied for significancy and standard deviation of all concentrations were given at Table 3.6.

Table 3.6. The percentage of LoVo cells corresponding to each apoptotic level (mean ± sd)

		Healthy	**Early Apoptosis**	**Late Apoptosis**	**Necrosis**
No treatment		90,65% ± 2,83%	4,58% ± 2,55%	4,16% ± 1,42%	0,63% ± 0,4%
SD2	*500 µg/ml*	18,32% ± 9,24% ***	31,93%±17,54% ***	31,85% ± 4,87% ***	17,94%± 14,29% *
	623 µg/ml (IC50)	14,93% ± 7,46% ***	32% ± 5,34% ***	36,03% ± 5,39% ***	17,05% ± 8,98% *
	1000 µg/ml	9,55% ± 4,99% ***	28,75% ±12,3% **	33,15%±12,88% ***	28,55% ± 5,3% ***

Two-way ANOVA test with Tukey correction across each row is used to indicate statistical significance in relation to control group (* P<0.05, ** P<0.01, *** P<0.001).

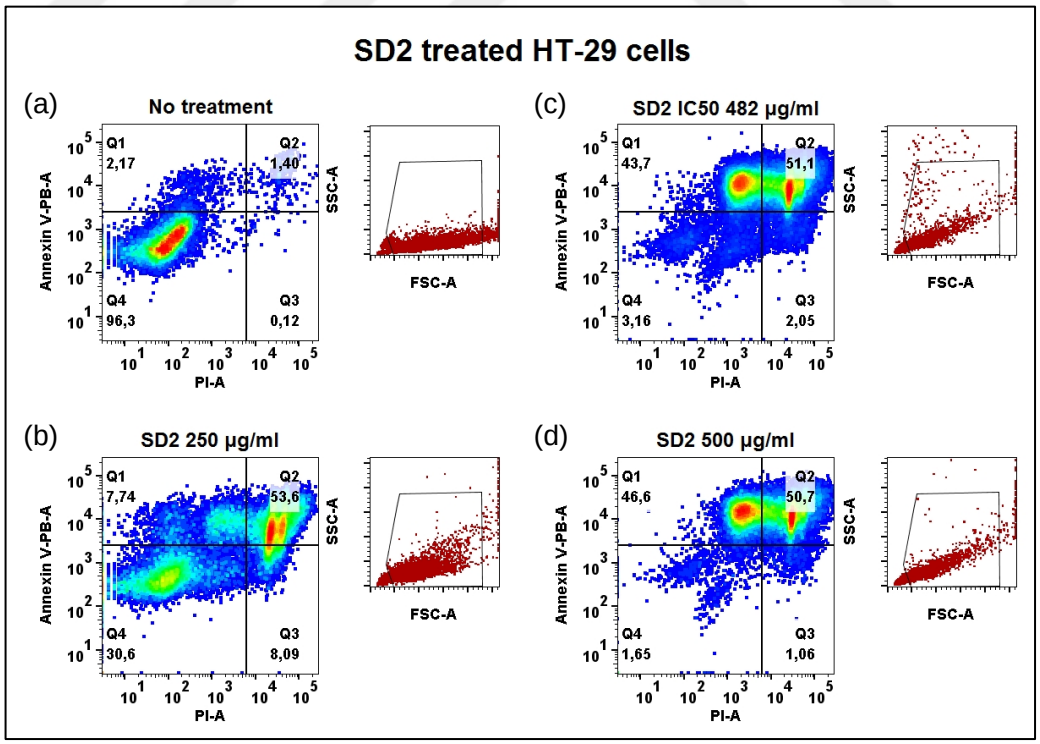

Figure 3.19. Effect of Dex-CeNPs (SD2) on apoptosis profile of HT-29 cells. (a) no treatment, (b) 250 µg /mL, (c) 482 µg /mL and (d) 500 µg /mL Dex-CeNPs treatment.

For HT-29 cell line, health of non- treated cells were 96% (Figure 3.19a). At 250 µg /mL, approximately 30% healthy cells were observed while 53% Late apoptosis was present (Figure 3.19b). At a concentration of 482 µg /mL (IC50 value), cell health was sharply reduced by up to 3%. However, while the rate of cells found in late apoptosis was 51%, this rate was observed as 44% for early apoptosis (Figure 3.19c). The health ratio for the 500 µg/mL concentration was 2%, in parallel to the 482 µg /mL concentration which was close to it. In addition, Late and Early Apoptosis rates are similar to IC50 values (Figure 3.19d). No visible change was detected in necrosis rates. Despite 500 µg /mL being the highest concentration, the most granularity was observed at IC50 value.

Table 3.7. The percentage of HT-29 cells corresponding to each apoptotic level (mean ± sd).

		Healthy	**Early Apoptosis**	**Late Apoptosis**	**Necrosis**
No treatment		95,38% ± 2,5%	4,19% ± 2,43%	2,08% ± 1,39%	0,16% ± 0,08%
SD2	*250 µg/ml*	67,6% ± 29,11% ***	5,8% ± 1,75%	20,68% ± 21,87%	5,94% ± 8,86%
	482 µg/ml (IC50)	**13,93% ± 7,93%** ***	23% ± 13,91%	**54,66% ± 7,41%** ***	8,41% ± 7,18%
	500 µg/ml	**10,06% ± 6,47%** ***	22,6% ± 15,54%	**62,96% ± 12,21%** ***	4,38% ± 5,21%

Two-way ANOVA test with Turkey correction across each row is used to indicate statistical significance * $p<0.05$, ** $p<0.01$, *** $p<0.001$ in relation to the control group.

3.3. PH DEPENDENT ANTI-CANCER PROPERTIES OF DEXTRAN-COATED NANOCERIA

Cytotoxicity properties of two Dex-CeNPs against colon cancer cell lines have very different profiles in terms of high IC50 values. After obtaining the first WST-1 Assay set with high concentration requirement, the idea of change in pH in the environment may affect the concentration increase. The efficacy of Dex-CeNPs (SD1) is low for colon cancer. In the literature, there are many studies on pH-dependent increased efficacy of nanoceria as a drug candidate. Therefore, to increase the efficacy of nanoceria for aggressive colon cancer cell lines, pH dependent effect of nanoceria were evaluated for SD1 treated COLO 201 and DLD-1 cell line at pH 6 and pH 7 as a case study. Before

performing cytotoxicity determination via WST-1 Assay, UV-Vis Spectra and DLS measurements were performed to understand any change in UV- Vis profile and size distribution.

3.3.1. Characterization of SD1 with pH6 and pH7

In order to observe the effects of change in nanoceria concentrations by changing its pH, UV-Vis Spectra and DLS measurements were compared with non-pH adjusted SD1.

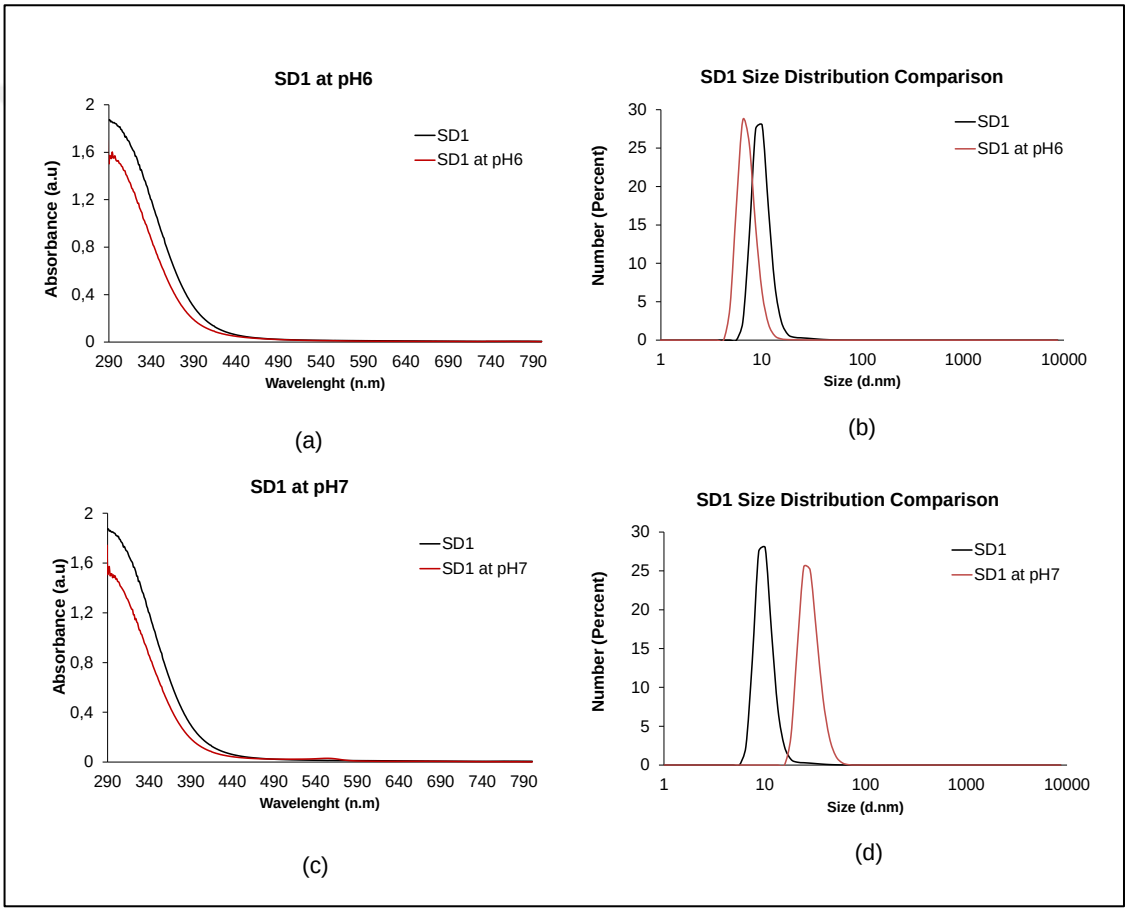

Figure 3.20. The size and size distribution of Dex-CeNPs studied using UV-Vis spectroscopy and DLS. (a) UV-Vis Spectrum of SD1 at pH 6 , (b) DLS measurement of SD1 at pH 6, (c) UV-Vis spectrum of SD1 at Ph 7, (d) DLS measurement of SD1 at pH 7.

In Figure 3.20a, the UV-Vis Spectrum of SD1 at pH 6 is shown. The expected nanoceria peak was in between 260 nm-320 nanometer and it was obtained at 294 nm with 1:100 dilution ratio. The peak is at the right nm range and has no difference compared to SD1 without any pH adjustment by regarding absorbance.

In Figure 3.20b, DLS measurement data of SD1 at pH 6 is shown. In this measurement, average nanoparticle size is less than 10 nm and ~30% of the nanoparticles have a size in between 5-10 nm with a ~5% decrease from 5 nm to 10 nm which also shows similar intensity profile as SD1 without any pH adjustments.

In Figure 3.20c, the UV-Vis Spectrum of SD1 at pH 7 is shown. The expected nanoceria peak was in between 260 nm - 320 nanometer range and it was obtained at 292 nm with 1:100 dilution ratio. The peak is at the right nm range and has slight difference compared to SD1 without any pH adjustment and SD1 at pH 6 by regarding absorbance.
In Figure 3.20d, DLS measurement data of SD1 at pH 7 is displayed that the average nanoparticle size is greater than 10 nm and 25% of the nanoparticles have a size in range of forming 15-30 nm, 20 nm and 22 nm for 25% of the sizes for each. It's been observed that pH 7 had larger particle size than SD1 without any pH adjustment. Unfortunately due to the high acidity of SD1, it was not possible to accurately measure the surface charge (zeta potential measurements) at pH 6, and due to the lack of comparison according to pH 7 zeta potential measurements, data is not shown.

3.3.2. WST-1 Assay with pH Adjusted Dex-CeNPs

Cytotoxic behaviors of SD1 with acidic (pH 6), neutral (pH 7), and basic pH values were analyzed against two different colon cancer cell lines; DLD-1 (ATTC CCL-221) and COLO 201 (ATTC CCL-224). The experiments were conducted at three different concentrations dextran-coated pH adjusted nanoceria. WST-1 assay was performed and measurements were taken on Day 1 and Day 3.

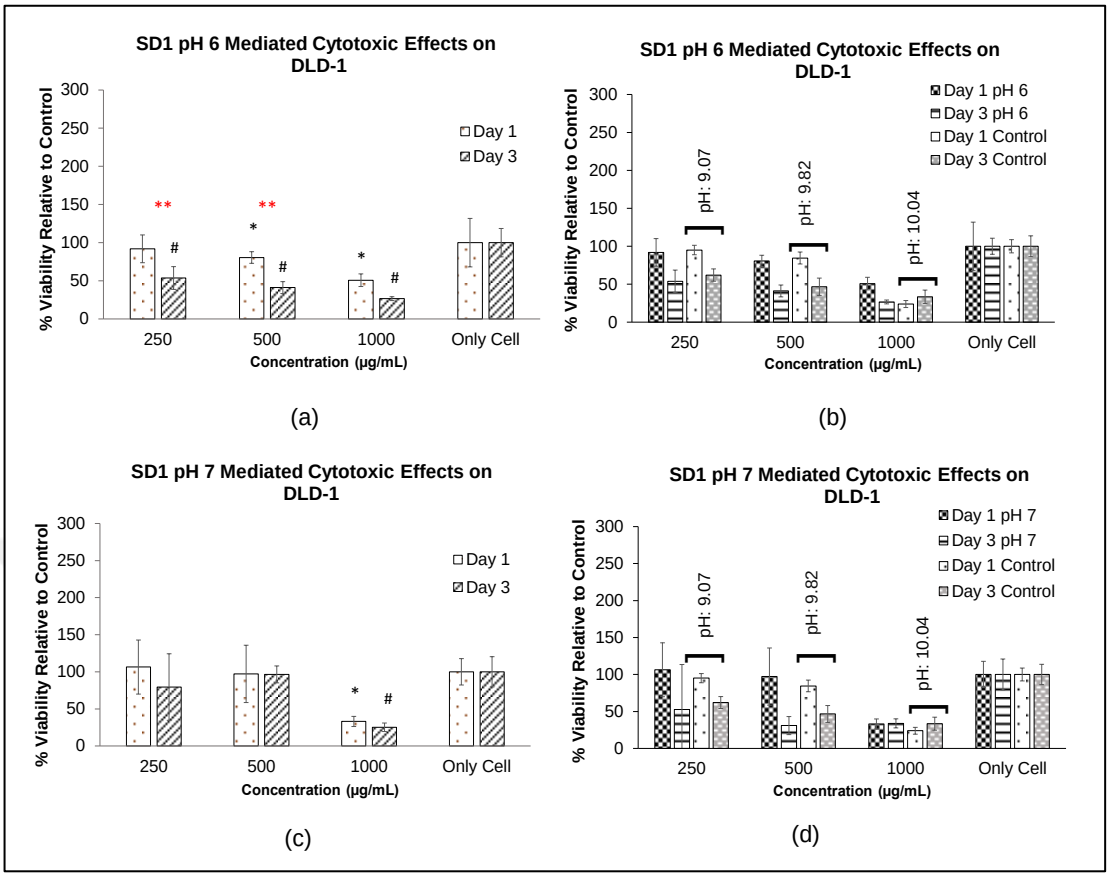

Figure 3.21. Cytotoxic properties of Dex-CeNPs (SD1) at pH 6 and pH 7 on DLD-1. (a) SD1 at pH 6 on DLD-1, (b) SD1 at pH 6 and not adjusted pH on DLD-1, (c) SD1 at pH 7 on DLD-1, (d) SD1 at pH 6 and not adjusted pH on DLD-1. * Represents comparison between SD1 control group and each concentration (p-value≤0.001), # Represents comparison between SD2 control group and each concentration.(p-value≤0.001), ** Represents comparison between SD1 and SD2 at the same concentration. (p-value≤0.001).

In Figure 3.21a, cytotoxic effect of pH 6 adjusted SD1 against DLD-1 at 250, 500, 1000 µg/mL concentrations at two time points (Day 1 and Day 3) were depicted compared to the control group (untreated cells) in terms of viability (%). At 250 µg/mL, slightly toxic effect was obtained on Day1 furthermore 50% toxicity was observed on Day 3. Initial toxic effect of SD1 against DLD-1 was observed at 500 µg/mL on Day 1 by 20% and approximately 2X more toxicity on Day 3. The most toxic concentration of SD1 against DLD-1 was 1000 µg/mL for each time-points with 50% toxicity on Day 1 and 75% toxicity on Day 3.

In Figure 3.21b, cytotoxic effect of pH 6 adjusted SD1 against DLD-1 at 250, 500, 1000 μg/mL concentrations at two time points (Day 1 and Day 3) were depicted compared to the control group (cell treatment without any pH adjustment) in terms of viability (%). At 250 μg/mL, both pH 6 and control group on Day1 showed no toxicity on DLD-1 cell line. On the contrary, pH 6 has ~50% toxicity and control group have 10% less toxicity than pH 6 adjusted SD1 on Day 3. In case of 500 μg/mL, slight toxicity (20%) for pH 6 and 25% toxicity for control group on Day 1 was observed. Toxicity trend was similar on Day 3 for pH 6 and control group with 40% toxicity. The most toxic concentration of SD1 against DLD-1 was 1000 μg/mL and for Ph 6, the toxicity was detected as 50% while the toxicity on control group was 80%. Day 3 of each group had slight toxicity differences. In Figure 3.21c, cytotoxic effect of pH 7 adjusted SD1 against DLD-1 at 250, 500, 1000 μg/mL concentrations at two time points (Day 1 and Day 3) were depicted compared to the control group (untreated cells) in terms of viability (%). At 250 μg/mL, no toxic effects were obtained on Day1 and 50% toxicity was observed on Day 3 similar with pH 6. At Day 1, there was 20% toxicity at pH 6 500 μg/mL, while no toxicity was observed at pH7 500 μg/mL. Toxicity for Day 3 at the same concentration was 59% at pH 6 and around 70% at pH 7. The most toxic concentration of SD1 against DLD-1 was 1000 μg/mL for each time-points with 70% toxicity on Day 1 and 75% toxicity on Day 3.

In Figure 3.21d, cytotoxic effect of pH 7 adjusted SD1 against DLD-1 at 250, 500, 1000 μg/mL concentrations at two time points (Day 1 and Day 3) were depicted compared to the control group (cell treatment without any pH adjustment) in terms of viability (%). At 250 μg/mL, while no toxic effects were obtained for pH 7 similar with pH 6 and control group on Day1. Besides, pH 7 has similar ~50% toxicity profile and control group have 10% less toxicity than pH 7 adjusted SD1 on Day 3. In case of 500 μg/mL, no toxicity observed for pH 7 and 15% toxicity for control group on Day 1. Viability profile was similar on Day 3. For pH7, approximately 50% toxicity detected and control group showed 10% less toxicity than pH 7 adjusted SD1 on Day 3. The most toxic concentration of SD1 against DLD-1 was 1000 μg/mL for each time-points and each group with slight differences.

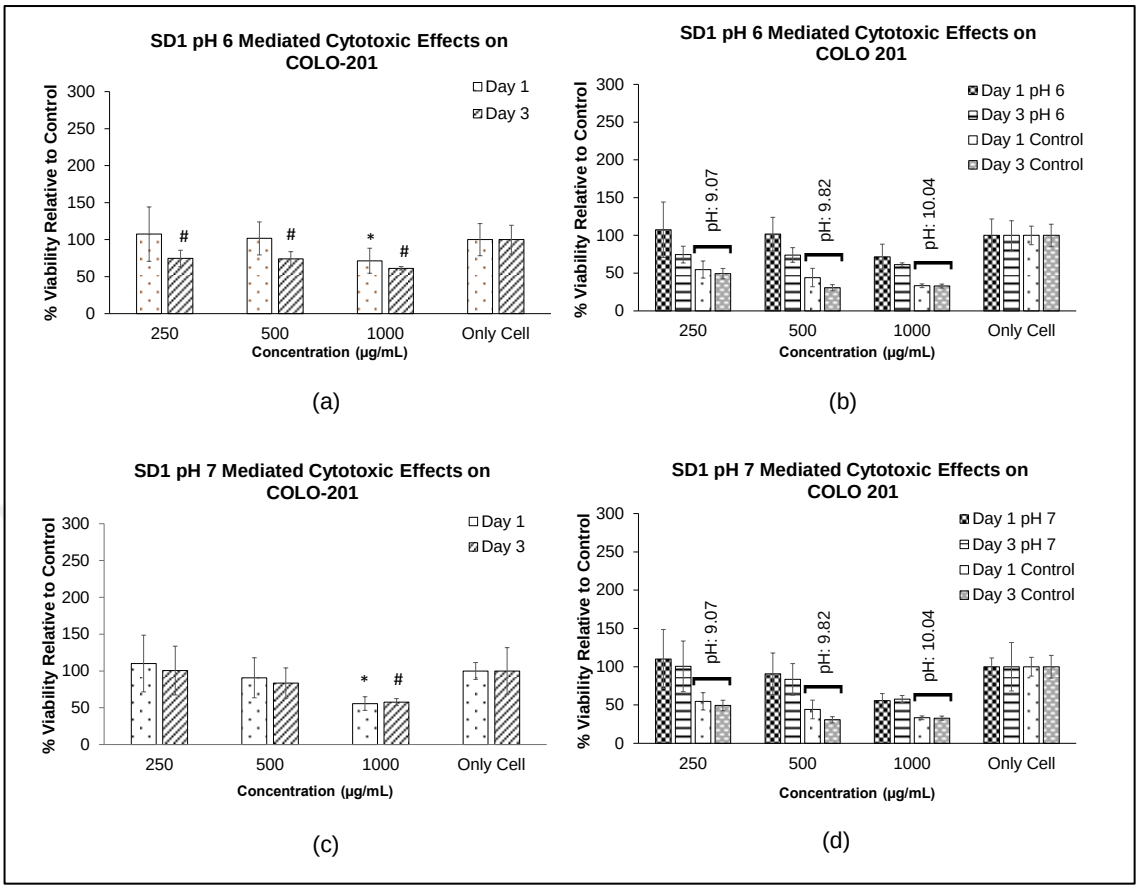

Figure 3.22. Cytotoxic properties of Dex-CeNP (SD1) against COLO 201 cell line at pH 6 and pH 7. (a) SD1 at pH 6 on COLO 201, (b) SD1 at pH 6 and not adjusted pH on COLO 201, (c) SD1 at pH 7 on COLO 201, (d) SD1 at pH 6 and not adjusted pH on COLO 201. * Represents comparison between SD1 control group and each concentration (p-value≤0.001), # Represents comparison between SD2 control group and each concentration.(p-value≤0.001).

In Figure 3.22a indicates the cytotoxic effect of pH 6 adjusted SD1 against COLO 201 cell line. No viability decrease was observed at 250 µg/ mL and 500 µg/mL on Day 1. Also, slight decrease on viability on Day 3 was obtained for both concentrations was detected. At 1000 µg/mL on Day 1, viability decreased by 30% and 40% Day 3 compared to control group.

In Figure 3.22b, cytotoxic effect of pH 6 adjusted SD1 against COLO 201 at 250, 500, 1000 µg/mL concentrations at two time points (Day 1 and Day 3) were depicted compared to the control group (cell treatment without any pH adjustment) in terms of viability (%). At 250 µg/mL, while no toxic effects were obtained for pH 6 on Day1, approximately 50% toxicity was observed for control group. Besides, pH 6 has 75% viability and control group

had a similar viability on Day 3 compared to Day 1. At 500 μg/mL, similar viability profile was observed for pH 6 on COLO 201 cell line Day 1. Similar profile for control group at the same concentration was also observed compared to 250 μg/mL on Day 1. On contrary, control group has ~20% slight toxicity difference with respect to 250 μg/mL for Day 3. In case of 1000 μg/mL, viability on Day 1 decreased by 30% for pH 6 and 70% toxicity was observed for control group. 10% increase in toxicity obtained on Day 3 compared to 500 μg/mL for pH 6 and no toxicity with respect to 500 μg/mL was detected for control group. Figure 3.22c indicates the cytotoxic effect of pH 7 adjusted SD1 against COLO 201 cell line. No viability decrease was observed at 250 μg/mL for each time points. However, slight decrease (10%) on viability on Day 1 was obtained at 500 μg/mL and 20% toxicity was observed on Day 3 compared to control group. At 1000 μg/mL on Day 1, viability decreased by 45% and approximately 40% on Day 3 compared to control group.

In Figure 3.22d, cytotoxic effect of pH 7 adjusted SD1 against COLO 201 at 250, 500, 1000 μg/mL concentrations at two time points (Day 1 and Day 3) were depicted compared to the control group (cell treatment without any pH adjustment) in terms of viability (%). At 250 μg/mL, no toxicity profile was observed at pH 7 for each time points. At 500 μg/mL, control group has ~45% more toxicity than pH 7 on Day1. On contrary, toxicity difference was more than 2 fold between control group and pH 7 on Day 3. At concentration 1000 μg/mL, viability on Day 1 decreased by 45% for pH 7 and 67% toxicity was observed for control group. Besides, pH 7 viability profile was ~20% more on Day 3 than control group.

3.3.2.1. IC50 Values pH Adjusted Dex-CeNPs on Colon Cancer Lines

To understand the effect of pH change on SD1 deeply, the quantitative analysis was performed by calculating the IC50 value. This value comparison to non- pH adjusted SD1 (Table 3.8) showed that both pH 6 and pH 7 increased the required concentrations.

Table 3.8. IC50 values of DLD-1, COLO 201 cell lines with respect to pH 6 and pH 7.

IC50 (μg/mL)	**pH 6**	**pH 7**	**Not adjusted pH**
DLD- 1	390	495	745
COLO 201	535	318	232

4. DISCUSSION

In this study, nanoceria was successfully coated with two different dextran molecules. Dextran, prevented the aggregation of nanoceria, increased the solubility of the suspension in the medium and maintained the stability of the nanoparticle. The characterization of the synthesized Dex-CeNPs was performed using different methods such as (Uv-Vis, DLS, FTIR, TEM, Raman, XPS, TGA and XRD).

The UV-Vis spectrophotometry results of two synthesized Dex-CeNPs (SD1 and SD2) indicate the dominance of Ce^{+4} state in both syntheses. The size differences between SD1 and SD2, as measured by dynamic light scattering, may be due to the difference in molecular weight of the dextran used to coat the nanoceria. SD1 has slightly positive, SD2 has slightly negative zeta potential values within the expected biological range. The FTIR spectra of both syntheses show the successful dextran surface coating of nanoceria along with confirmation using Raman spectra. High-resolution transmission electron microscopy (HR-TEM) images indicate small core sizes for both syntheses, as well as the (111) and (220) face-centered cubic planes characteristic of CeO_2. X-ray photoelectron spectroscopy (XPS) results show the presence of cerium and oxygen on the surface of both syntheses, with a higher concentration of Ce^{+4} on SD2 than SD1. The TGA results indicated that higher stability of SD2 than SD1 at high temperatures. Six-month stability results showed three-week stability and safety of both syntheses. Successful characterization of the processes led to testing of both syntheses in cell culture. The cytotoxic effect of the syntheses was evaluated using WST-1 assay on various colon cancer cell lines. The results showed that SD2 was more effective in colon cancer cell lines, but the toxicity rate for HT-29 was approximately the same for both syntheses. No toxicity was observed for either synthesis on the SW48 line. In the other three cell lines, approximately 2-fold cytotoxic differences were observed between the IC50 values of SD1 and SD2. The results showed that SD2 was more effective in colon cancer cell lines and had the ability to scavenge ROS at all concentrations below the IC50 value for each cell line. The synthesis of SD1 resulted in increased production of ROS in the COLO 201 and DLD-1 lines and had a lower response in colon cancer cell lines at high concentrations. Due to the difference in toxicity and ROS production profiling in between two syntheses,

the flow cytometry analysis was conducted on SD2. In order to decrease the required concentration for IC50 values, SD1 was adjusted to pH 6 and pH 7 in order to understand the effects of pH on the synthesis toxicity and the change of characteristics of the nanoparticle. The UV-Vis data of both adjusted pH syntheses correlated with the unadjusted pH data. However, the size of the pH 6 synthesis was similar to that of the unadjusted synthesis (10 nm), while the size of the pH 7 synthesis was as large as that of SD2 (100 nm). It was suggested that the size of the pH 7 synthesis may be larger due to increased agglomeration at this pH. The pH-dependent cytotoxic effect of SD1 was also evaluated on the DLD-1 and COLO 201 cell lines. The results showed that a higher concentration was needed at pH 6 than at pH 7 and pH 9. It was concluded that the response of nanoceria to different pH levels may vary depending on the cell line. Overall, the results showed that both Dex-CeNPs were successfully synthesized with potential use in biological applications.

The synthesis color of SD1 [74, 93] correlated with the results given as in the literature. The color difference of SD2 [102] was found in the literature in accordance with the obtained data. Naha et al. [15] synthesized dextran coated nanoceria using the precipitation method with small differences to the results of our study. According to the UV-Vis spectrophotometry results they obtained, maxima peak of Dex-CeNPs was at 290 nm [15]. Also, *Davoodbasha et al.* synthesized the biocompatible cellulose-coated nanoceria with the UV-Vis peak maxima profile at 300-310 nanometers [103]. Both results correlate with the UV-Vis results obtained for both syntheses in this study. Size differences between the two Dex-CeNPs synthesis was significant. As in the literature, there are also differences in hydrodynamic sizes of the Dex-CeNPs. According to *Perez et al.*, dextran coated cerium oxide nanoparticles were synthesized by alkaline-based precipitation method with the size of the particle being approximately 10 nm [74] which is similar to SD1.

The FTIR profiles of both dextran types used to coat syntheses were very similar, and all the expected bands of IR-sensitive vibrational modes were observed in the molecules, as seen in the literature [15]. Since the intense OH vibration has a wide band gap, it hides the C-H vibration. The C-O-C vibration observed at 1158 cm^{-1} belongs to the glycosidic bonds formed between the saccharides. A wide band of characteristic nitrate ion (NO_3^-) vibrational modes is observed between 1470 and 1250 cm^{-1}. in the ATR-FTIR spectra of

the doping agent $Ce(NO_3)_36H_2O$. The appearance of the vibrational band attributed to NO_3^- ions in the FTIR plots of dextran-coated SD1 and SD2 and the disappearance of the C-O-C resonance band observed in the dextran plot confirm the successful coating of both syntheses with dextran. The peak observed at 630 cm^{-1} in the fingerprint region and attributed to the O-Ce-O band indicates the presence of nanoceria [104]. The vibration band at 1738 cm^{-1} in the graph is associated with C=O bonds. The peaks of H_2O (H–O–H) molecular bonds were observed at almost the same point: 1640 cm^{-1} for SD1 and 1639 cm^{-1} for SD2 [105]. In addition, weak C-H bending peak at 1467 cm^{-1} point in the graph [106] and N-O characteristic vibration bands [104] in 1340 and 1361 cm^{-1} region were detected. In conclusion, the results from FTIR show that both syntheses are successfully coated with dextran.

Raman Spectroscopic data confirmed the FTIR data and indicated the purity of the syntheses, as well as the success of dextran coating. As it is shown in the literature, the fingerprint band for CeO_2 at 464 cm^{-1} [107] was not observed for SD1 and SD2 due to the dextran coating on their surface.

Despite their hydrodynamic size differences, TEM data showed each synthesis is below 5 nm had an FCC structure, and was homogenously distributed in solution, which is in correlation with literature [15, 108]. *Yazici et al.* synthesized 0.1 M dextran coated nanoceria by the same precipitation method with the core size 3-4 nm with FCC structure [94]. Also, according to study on ethylene glycol coated nanoceria formulated using alkaline precipitation method by *Hanafy et al.* confirms that the core size of the nanoceria does not exceed 5 nanometers (4 nm averagely) and is distributed homogenously [109].

XRD data is in correlation with TEM data as well as the literature. Both syntheses showed cerium oxide characteristic (111) planes with diffraction peaks at approximately 17^o, (220) plane at 43.5^o , and (311) plane at 63.8^o. The study conducted by *Li et al.* on water-soluble ultrafine monodisperse dextran (T-10) coated cerium oxide nanoparticles which were synthesized by precipitation method displayed similar peaks. Also, the significant broadness of (111) plane implies the small size and low-crystallinity of cerium oxide nanoparticles [110]. In addition, the excess amount of water remaining in the dextran as a polymer, was the cause of the broad diffraction patterns as visualized in the pristine

hydrogel by *Cha et al.* resulting in an XRD pattern with broad peak on (111) plane [111]. Their antimicrobial studies indicates that the high intensity and wider peak at the (111) plane may be due to water retention as dextran is a polymer.

As it is known that the CeO_2 has a valence switch from Ce^{3+} to Ce^{4+} so, the ratios of Ce^{3+}/Ce^{4+} was distinguished in detail using UV-Vis spectroscopy data, which showed that SD1 had more Ce^{4+} compared to Ce^{3+}. On the other hand, opposite electrical state profile was detected for SD2 where the Ce^{3+} ratio was more than Ce^{4+} ratio. In comparison with the literature, *Li et al*. reported presence of both Ce^{+3} and Ce^{+4} with a Ce^{+3} /Ce^{+4} of 0.80 on cerium oxide nanoparticles [112]. Another study published by *Costantino et al*. with cellulose acetate nanoceria synthesis also showed mixture of Ce^{+3} and Ce^{+4} at a % ratio of 30:70 for Ce^{+3}:Ce^{+4} [113].

TGA results published by *Kaygusuz et al.*, showed that the decomposition profile of their alginate based functionalized nanoceria was similar to what we obtained from both syntheses. Also, to show the importance of functionalization they compared the non-functionalized and functionalized nanoceria, which indicated that the functionalized nanoceria lost its 88% of initial mass with slow and steady decomposition, while the non-functionalized nanoceria retained 92% of its initial mass [114]. *Mohammadi et al*. reported that the first stage of weight loss of double dextran/PEG coated iron oxide nanoparticles was due to the evaporation of water molecules. But for second stage, it was reported 220-440^{o} attributed to dextran and PEG degradation [98]. Similar TGA profiles were obtained for both syntheses with a weight loss of 89% for SD1 and 97% for SD1.

Based on these results, six-month stability experiments were carried out to determine the shelf life of the syntheses. In this process, absorbance, charge and size values of the syntheses were evaluated with UV-Vis, Zeta Potential and DLS techniques at different time periods (Day 0, Day 7, Day 14, Day 21, Day 28, Month 2, Month 4, Month 6). In accordance with the obtained UV-Vis results, while the Ce^{4+} status on the SD1 surface increased as time passed, the Ce^{3+} status on the SD2 surface increased. The stability deterioration of SD1 synthesis started with very high absorbance values, with shifts in the peaks and even absorbance saturations after 21st day. However, the changes in absorbance values and peak shifts did not show drastic differences for SD2. On the other hand, the

size characteristics of SD1 and SD2 exhibited different profiles. SD1 has a smaller size (8-33 nm range) compared to SD2 and shows more variability over 6 months compared to SD2 according to DLS data. According to the results, SD2 has a larger size (60-100 nm range) compared to SD1. However, changes in the particle size properties of SD2 showed very minimal changes over the 6-month period compared to SD1. The charge profile of SD1 and SD2 were very similar for 6 months, and both syntheses started to become out of the charge range required to penetrate cells after the 21st day. The surface charge data also proves that these syntheses are not suitable for use after the 21st day due to loss in stability as displayed by UV-Vis and DLS. As a result of the stability experiments, the syntheses were not considered suitable for use in experiments after three weeks.

In line with the difficulties encountered in cell culture studies, the characterizations of the syntheses with pH adjusted to 6 and 7 for SD1 were examined. When we compare the characterization data with our unadjusted pH data, it was seen that the UV-Vis data of both syntheses were complementary. However, in DLS measurements, the size of pH 6 synthesis was about the same (10 nm) as the size of pH unadjusted synthesis, which is correlated with the data published by *Alparslan et al.* [93], while the size of pH 7 was as large as the size (100 nm), probably due to higher potential of agglomeration at pH 7.
The knowledge about the cytotoxicity of Dex-CeNPs on colon cancer cell lines are limited in the literature due to the novelty of this work. The data obtained on colon cancer cell lines, indicated that each cancer cell line the responses to each synthesis was different. *Miri et al.* reported cytotoxicity of biosynthesized cerium oxide nanoparticles on HT-29 cell line of 0-800 μg/mL concentration of 24 hours had maximum 20% toxicity at 800 μg/mL concentration according to the MTT assay [88]. In our study, both Dex- CeNPs had 50% toxicity at approximately 500 μg/mL concentration, which can be contributed to the importance of coating. According to *Akhtar et al.*, the cytotoxic activity of cerium oxide nanoparticle on different cell lines displayed no significant cell death in MCF-7 and HT-1080 cell lines at concentrations below 200 μg/mL of cerium oxide nanoparticles [115]. Meanwhile, Dex-CeNP (SD2) is toxic under 200 μg/mL for COLO 201 cell line. They also reported that in contrast to the previous studies, MCF-7 and HT-1080 cell lines showed a tendency towards a slight increase in cell numbers when treated with Cerium oxide nanoparticles at concentrations up to 100 μg/ml. Same profile was observed for LoVo and HT-29 cell lines treated with Dex-CeNPs at low concentrations after 24 hours

of treatment. Another study reported by *Yazici et al.* shows the importance of Dextran coating of nanoceria. Which is based on the comparison of two different molarity of T-10 dextran (0.1 M vs 0.01 M) coated nanoceria toxicity on MG-63 cell line. Results indicate that while 0.01 M dextran coaated nanoceria does not show any toxicity to the MG-63 cell line, 0.1 M dextran coated nanoceria has IC50 value at approximately 1000 μg/mL concentration [94]. Despite the molarity difference of the dextran (0.375 M for both SD1 and SD2) and type of dextrans, LoVo and DLD-1 cell lines showed similar cytotoxicity profile according to WST-1 assay as MG-63 cell line for SD1 after 24 hours of treatment. Comparison of poly(acrylic acid) PNC, aminated poly(acrylic acid) ANC, and dextran coated cerium oxide nanoparticles, *Asati et al.* reported that while ANC shows cytotoxicity for H9c2 cardiac myocytes, HEK293 human embryonic kidney cells and A549 lung carcinoma cells, no toxicity is observed for MCF-7 breast cancer cell lines. PNC only cytotoxic to A549 lung carcinoma cells and dextran shows no toxicity to any of cancer cells [79]. In our study, SW48 cell line did not show any response to SD1 and SD2 syntheses.

From the pH dependency aspect, *Alparslan et al.* reported that at pH 9 on day 1 compared to control group for all concentrations (from 10 to 1000 μg/mL) given to the osteosarcoma cell lines, after 3 days of treatment 500 μg/mL shows cytotoxicity. Also, slight increase at low concentrations (10 to 250 μg/mL) is demonstrated in the graph. pH 7 shows the same cytotoxicity profile compared to pH 9 after 24 and 72 hours of treatment. However, pH 6 cytotoxicity on osteosarcoma cells was significantly effective after 500 μg/mL concentrations [14]. In our study, DLD-1 cell line showed approximately 2- fold greater cytotoxicity on pH 6 compared to pH 9 on IC50 values after 24 hours of treatment with SD1.Another study published by *Perez et al.*, focused on two healthy cell lines and two carcinomas with Dextran coated nanoceria at pH 4. Their data showed that Dextran coated nanoceria protected the healthy cell lines, while their viability severely decreased for carcinomas [74].

Along with the cytotoxicity assays, ROS assays were also performed. The reason for this was to look at the ROS production of the cell at the given concentrations and to observe whether the Dex-CeNPs were ROS scavenger. *Lord et al.* compared ROS production of nanoceria and heparin functionalized nanoceria. Their results show that after 24 hours of treatment on BaF32 cells, ROS production decreased compared to control group (medium)

for nanoceria. Also, heparin nanoceria shows slightly decreased ROS formation profile compared to control group. On contrary, after 72 hours of treatment with nanoceria, ROS formation was similar as treatment of 24 hours while heparin functionalized nanoceria shows greater ROS production compared to 24 hours of treatment [116]. According to the experimental results, SD2 showed the ability to scavenge ROS at all concentrations below the IC50 value for each cell line, while the synthesis of SD1 showed 4 times the production of ROS in the COLO 201 and DLD-1 line compared to the control group, and this rate was higher than in all other cell lines. Based on this result, it deemed appropriate to test these two cell lines (DLD-1 and COLO 201) with pH adjustments. Almost the same ROS generation profiles were observed for the LoVo and SW48 lines compared to the control. Compared to literature, it is understandable that ROS production responses varies for every cell line.

Li et al. reported 200 μg/mL of treatment for BGC-803 cells is affected by the type of surface functional group present on the particles. The ultrafine monodisperse water-insoluble (CeO_2 –P) nanoparticles had higher intensities of SS and were more easily uptaken by the BGC-803 cells compared to the CeO_2-dextran, poly-acrylic acid (CeO_2-PAA), and ethylenediamine (CeO_2-EDA) nanoparticles. The cell uptake of nanoceria followed the order CeO_2-P > CeO_2-EDA > CeO_2-dextran > CeO_2-PAA, indicating that the surface functional groups on the nanoceria particles greatly influence their uptake by cells. The size of the cells did not change, as indicated by the constant FS value. Overall, the results suggest that the type of surface functional group on nanoceria particles plays a significant role in their uptake by BGC-803 cells [110]. The same profile was observed for COLO 201 cell line in our study at 100, 124 (IC50) and 250 μg/mL concentrations. *Datta et al*. reported that flow cytometry analysis of HCT 116 cell lines treated with 30, 50 and 70 μg/mL nanoceria showed that the percentage of cells undergoing early apoptosis (as indicated by Annexin V-FITC labeling) and late apoptosis (as indicated by Annexin V-FITC and DAPI labeling) increased significantly when the cells were treated with increasing concentrations of cerium dioxide. This suggests that the treatment may have a toxic effect on the cells, leading to cell death [86], which also correlates with the data obtained for DLD-1, HT-29 and LoVo cell lines treated with SD2.

According to obtained data from characterization analyses and cell culture experiments performed with SD1 and SD2 on colon cancer cell lines, Dex-CeNP is a subject with

remarkable features which can be modified via various methods and worth for future analysis.

5. CONCLUSION

Dex-CeNPs are promising nanoparticles due to their remarkable valence electron switch in between Ce^{+3} to Ce^{+4} states depending on the pH differences which makes nanoparticles to be selective to the cancer cells and stromal cells. According to obtained experimental data, although the successful characterization profiles of these two syntheses were compatible with each other, differences in size and weight was discerned, supporting the critical role of the different dextrans used in production of SD1 and SD2; and thus, their resultant cytotoxicity on colon cancer cell lines. Based on the low-dose efficiency of SD2, the stage at which cells undergo death was examined and promising results, which could be used in further research, were obtained. Aiming to reduce the high dose requirement in SD1, the response of colon cell lines was tested at various pH values. The results pointed to the higher protectivity of nanoceria at acidic than neutral pH values. The novelty of this study was not only the synthesis and testing of two different types of Dextran–coated nanoceria on multiple colon cancer cell lines for the first time in the literature, but also the comparison of two types of nanoceria at altered pH values. The results of this research contribute to the understanding of the effects of nanoceria on colon cancer cell lines with different mutations and MSI status, which provides a broader perspective to the field of nano science.

6. FUTURE DIRECTIONS

In future studies, pathway analyzes can be performed to better understand the gene-based effect mechanisms of the syntheses. Also, investigations of the apoptotic or proliferation protein expression levels of western blotting syntheses can be performed. A healthy colon cell line can be added to the cell sets and studies can be carried out comparatively. Detailed characterizations (FTIR, TEM, Raman, XRD, XPS, TGA etc.) of pH modified syntheses can also be done for better understanding the structure of synthesis. 3D cell culture models can be used for microenvironmental investigation of pH change. In order to observe the cellular responses due to pH change more sharply, the pH of the acidic environment can be further reduced and *in vivo* experiments of nanoparticles can be conducted.

REFERENCES

1. Yadav N. Cerium oxide nanostructures: properties, biomedical applications and surface coatings. *3 Biotech*. 2022;12(5):1-20.

2. Jeevanandam J, Barhoum A, Chan YS, Dufresne A, Danquah MK. Review on nanoparticles and nanostructured materials: history, sources, toxicity and regulations. *Beilstein journal of nanotechnology*. 2018;9(1):1050-74.

3. Ray SS, Bandyopadhyay J. Nanotechnology-enabled biomedical engineering: Current trends, future scopes, and perspectives. *Nanotechnology Reviews*. 2021;10(1):728-43.

4. Sajid M. Nanomaterials: Types, properties, recent advances, and toxicity concerns. *Curr Op Environ Sci Health*. 2022;25:100319.

5. Makvandi P, Wang Cy, Zare EN, Borzacchiello A, Niu Ln, Tay FR. Metal-based nanomaterials in biomedical applications: Antimicrobial activity and cytotoxicity aspects. *Advanced Functional Materials*. 2020;30(22):1910021.

6. Khan SA. Metal nanoparticles toxicity: Role of physicochemical aspects. Metal Nanoparticles for Drug Delivery and Diagnostic Applications: *Elsevier*; 2020. p. 1-11.

7. Aderibigbe BA. Metal-based nanoparticles for the treatment of infectious diseases. *Molecules*. 2017;22(8):1370.

8. Bhat MA, Nayak B, Nanda A, Lone IH. Nanotechnology, metal nanoparticles, and biomedical applications of nanotechnology. *Oncology: Breakthroughs in Research and Practice*: IGI Global; 2017. p. 311-41.

9. Schrand AM, Rahman MF, Hussain SM, Schlager JJ, Smith DA, Syed AF. Metal-based nanoparticles and their toxicity assessment. *Wiley interdisciplinary reviews: Nanomedicine and Nanobiotechnology*. 2010;2(5):544-68.

10. Andreescu S, Ornatska M, Erlichman JS, Estevez A, Leiter J. Biomedical applications of metal oxide nanoparticles. *Fine particles in medicine and pharmacy*: Springer; 2012. p. 57-100.

11. Sagadevan S, Fareen A, Hoque ME, Chowdhury ZZ, Johan MRB, Rafique RF, et al. Nanostructured polymer biocomposites: pharmaceutical applications. *Nanostructured Polymer Composites for Biomedical Applications*. 2019:227-59.

12. Thakur N, Manna P, Das J. Synthesis and biomedical applications of nanoceria, a redox active nanoparticle. *Journal of Nanobiotechnology*. 2019;17(1):1-27.

13. Saifi MA, Seal S, Godugu C. Nanoceria, the versatile nanoparticles: promising biomedical applications. *Journal of Controlled Release*. 2021;338:164-89.

14. Alpaslan E, Yazici H, Golshan NH, Ziemer KS, Webster TJ. pH-dependent activity of dextran-coated cerium oxide nanoparticles on prohibiting osteosarcoma cell proliferation. *ACS Biomaterials Science & Engineering*. 2015;1(11):1096-103.

15. Naha PC, Hsu JC, Kim J, Shah S, Bouché M, Si-Mohamed S, et al. Dextran-coated cerium oxide nanoparticles: a computed tomography contrast agent for imaging the gastrointestinal tract and inflammatory bowel disease. *ACS nano*. 2020;14(8):10187-97.

16. Hartati YW, Topkaya SN, Gaffar S, Bahti HH, Cetin AE. Synthesis and characterization of nanoceria for electrochemical sensing applications. *RSC advances*. 2021;11(27):16216-35.

17. Liying H, Yumin S, Lanhong J, Shikao S. Recent advances of cerium oxide nanoparticles in synthesis, luminescence and biomedical studies: a review. *Journal of rare earths*. 2015;33(8):791-9.

18. Mazumder S, Nayak AK, Ara TJ, Hasnain MS. Hydroxyapatite composites for dentistry. *Applications of Nanocomposite Materials in Dentistry*. 2019:123-43.

19. Vattikuti S, Byon C, Reddy C, Shim J, Venkatesh B. Co-precipitation synthesis and characterization of faceted MoS2 nanorods with controllable morphologies. *Applied Physics A*. 2015;119(3):813-23.

20. Rane AV, Kanny K, Abitha V, Thomas S. Methods for synthesis of nanoparticles and fabrication of nanocomposites. *Synthesis of inorganic nanomaterials*: Elsevier; 2018. p. 121-39.

21. Dahman Y. Nanotechnology and functional materials for engineers: *Elsevier*; 2017.

22. Kumari SC, Dhand V, Padma PN. Green synthesis of metallic nanoparticles: a review. *Nanomaterials*. 2021:259-81.

23. Singh J, Dutta T, Kim K-H, Rawat M, Samddar P, Kumar P. 'Green'synthesis of metals and their oxide nanoparticles: applications for environmental remediation. *Journal of nanobiotechnology*. 2018;16(1):1-24.

24. Kafle B. Introduction to nanomaterials and application of UV–Visible spectroscopy for their characterization. *Chemical analysis and material characterization by spectrophotometry*. 2020;6.

25. El-Sherbiny IM, Arafa K, Fytory M. Physical properties, classification, synthesis, and functionalization of magnetic nanomaterials. *Magnetic Nanomaterials in Analytical Chemistry*: Elsevier; 2021. p. 3-21.

26. Yang G, Park S-J. Conventional and microwave hydrothermal synthesis and application of functional materials: A review. *Materials*. 2019;12(7):1177.

27. Sadjadi S. Supercritical fluids in nanoreactor technology. *Organic Nanoreactors*: Elsevier; 2016. p. 373-419.

28. Prasad S, Kumar V, Kirubanandam S, Barhoum A. Engineered nanomaterials: nanofabrication and surface functionalization. *Emerging applications of nanoparticles and architecture nanostructures*: Elsevier; 2018. p. 305-40.

29. Zielińska-Jurek A, Reszczyńska J, Grabowska E, Zaleska A. Nanoparticles preparation using microemulsion systems. *Microemulsions-an introduction to properties and applications*. 2012:229-50.

30. Sarkar A, Saha N, Majumdar G. Fabrication and Characterization of Flexible Semi-conducting Nanocomposite Polymer. 2022.

31. D'Arienzo M, Scotti R, Di Credico B, Redaelli M. Synthesis and characterization of morphology-controlled TiO2 nanocrystals: Opportunities and challenges for their

application in photocatalytic materials. *Studies in Surface Science and Catalysis*. 2017;177:477-540.

32. Fornasiero P, Cargnello M. Morphological, Compositional, and Shape Control of Materials for Catalysis: *Elsevier*; 2017.

33. MODAN EM, PLĂIAȘU AG. Advantages and disadvantages of chemical methods in the elaboration of nanomaterials. *The Annals of "Dunarea de Jos" University of Galati Fascicle IX, Metallurgy and Materials Science*. 2020;43(1):53-60.

34. Cho K, Wang X, Nie S, Chen Z, Shin DM. Therapeutic nanoparticles for drug delivery in cancer. *Clinical cancer research*. 2008;14(5):1310-6.

35. Travan A, Pelillo C, Donati I, Marsich E, Benincasa M, Scarpa T, et al. Non-cytotoxic silver nanoparticle-polysaccharide nanocomposites with antimicrobial activity. *Biomacromolecules*. 2009;10(6):1429-35.

36. Naha PC, Al Zaki A, Hecht E, Chorny M, Chhour P, Blankemeyer E, et al. Dextran coated bismuth–iron oxide nanohybrid contrast agents for computed tomography and magnetic resonance imaging. *Journal of Materials Chemistry B*. 2014;2(46):8239-48.

37. Abed SM, Noman A, Zhang T, Bakrey A. Production of dextrans and their applications in human health and nutrition–Review. *EUROPEAN ACADEMIC RESEARCH*. 2016;IV(4).

38. Díaz-Montes E. Dextran: sources, structures, and properties. *Polysaccharides*. 2021;2(3):554-65.

39. Cogan TM, Jordan KN. Metabolism of Leuconostoc bacteria. Journal of Dairy Science. 1994;77(9):2704-17.

40. Rawal S, Patel MM. Threatening cancer with nanoparticle aided combination oncotherapy. *Journal of controlled release*. 2019;301:76-109.

41. Chaturvedi VK, Singh A, Singh VK, Singh MP. Cancer nanotechnology: a new revolution for cancer diagnosis and therapy. *Current drug metabolism*. 2019;20(6):416-29.

42. Chatterjee P, Kumar S. Current developments in nanotechnology for cancer treatment. *Materials Today: Proceedings*. 2022;48:1754-8.

43. Grodzinski P, Kircher M, Goldberg M, Gabizon A. Integrating nanotechnology into cancer care. *ACS Publications*; 2019.

44. Marrugo-Ramírez J, Mir M, Samitier J. Blood-based cancer biomarkers in liquid biopsy: a promising non-invasive alternative to tissue biopsy. *International journal of molecular sciences*. 2018;19(10):2877.

45. Kiplagat A, Martin DR, Onani MO, Meyer M. Aptamer-conjugated magnetic nanoparticles for the efficient capture of cancer biomarker proteins. *Journal of Magnetism and Magnetic Materials*. 2020;497:166063.

46. Sanità G, Carrese B, Lamberti A. Nanoparticle surface functionalization: How to improve biocompatibility and cellular internalization. *Frontiers in Molecular Biosciences*. 2020;7:587012.

47. Zhang Z, Qian H, Huang J, Sha H, Zhang H, Yu L, et al. Anti-EGFR-iRGD recombinant protein modified biomimetic nanoparticles loaded with gambogic acid to enhance targeting and antitumor ability in colorectal cancer treatment. *International journal of nanomedicine*. 2018;13:4961.

48. Phongpradist R, Chittasupho C, Intasai N, Siahaan TJ, Berkland CJ, Charoenkwan P, et al. Biodegradable nanoparticles surface modification techniques with cIBR peptide targeting to LFA-1 expressing leukemic cells. *Journal of nanotechnology in engineering and medicine*. 2012;3(4).

49. Torres-Pérez SA, Torres-Pérez CE, Pedraza-Escalona M, Pérez-Tapia SM, Ramón-Gallegos E. Glycosylated nanoparticles for cancer-targeted drug delivery. *Frontiers in Oncology*. 2020;10:605037.

50. Yao Y, Zhou Y, Liu L, Xu Y, Chen Q, Wang Y, et al. Nanoparticle-based drug delivery in cancer therapy and its role in overcoming drug resistance. *Frontiers in Molecular Biosciences*. 2020;7:193.

51. Hanahan D. Hallmarks of cancer: new dimensions. *Cancer discovery*. 2022;12(1):31-46.

52. Acharya S, Sahoo SK. PLGA nanoparticles containing various anticancer agents and tumour delivery by EPR effect. *Advanced drug delivery reviews*. 2011;63(3):170-83.

53. Bertrand N, Wu J, Xu X, Kamaly N, Farokhzad OC. Cancer nanotechnology: the impact of passive and active targeting in the era of modern cancer biology. *Advanced drug delivery reviews*. 2014;66:2-25.

54. Maeda H, Bharate G, Daruwalla J. Polymeric drugs for efficient tumor-targeted drug delivery based on EPR-effect. *European journal of pharmaceutics and biopharmaceutics*. 2009;71(3):409-19.

55. Li Y, Zeng S, Hao J. Non-invasive optical guided tumor metastasis/vessel imaging by using lanthanide nanoprobe with enhanced down-shifting emission beyond 1500 nm. *ACS nano*. 2019;13(1):248-59.

56. Forte E, Fiorenza D, Torino E, Costagliola di Polidoro A, Cavaliere C, Netti PA, et al. Radiolabeled PET/MRI nanoparticles for tumor imaging. *Journal of Clinical Medicine*. 2019;9(1):89.

57. Song G, Kenney M, Chen Y-S, Zheng X, Deng Y, Chen Z, et al. Carbon-coated FeCo nanoparticles as sensitive magnetic-particle-imaging tracers with photothermal and magnetothermal properties. *Nature biomedical engineering*. 2020;4(3):325-34.

58. Reece-Mills M, Bath LE, Kelnar CJ, Wallace HB, Keys C, Carachi R. Long-term effects of childhood cancer therapy on growth and fertility. *The Surgery of Childhood Tumors*: Springer; 2016. p. 657-70.

59. Cohen D. Cancer drugs: high price, uncertain value. *BMJ*. 2017;359.

60. Oun R, Moussa YE, Wheate NJ. The side effects of platinum-based chemotherapy drugs: a review for chemists. *Dalton transactions*. 2018;47(19):6645-53.

61. Schirrmacher V. From chemotherapy to biological therapy: A review of novel concepts to reduce the side effects of systemic cancer treatment. *International journal of oncology*. 2019;54(2):407-19.

62. Chihara D, Fanale MA, Miranda RN, Noorani M, Westin JR, Nastoupil LJ, et al. The survival outcome of patients with relapsed/refractory peripheral T-cell lymphoma-not otherwise specified and angioimmunoblastic T-cell lymphoma. *British journal of haematology*. 2017;176(5):750-8.

63. Corrado G, Salutari V, Palluzzi E, Distefano MG, Scambia G, Ferrandina G. Optimizing treatment in recurrent epithelial ovarian cancer. *Expert review of anticancer therapy*. 2017;17(12):1147-58.

64. Parvanian S, Mostafavi SM, Aghashiri M. Multifunctional nanoparticle developments in cancer diagnosis and treatment. *Sensing and Bio-Sensing Research*. 2017;13:81-7.

65. Zhao C-Y, Cheng R, Yang Z, Tian Z-M. Nanotechnology for cancer therapy based on chemotherapy. *Molecules*. 2018;23(4):826.

66. Chen Y, Chen C, Zhang X, He C, Zhao P, Li M, et al. Platinum complexes of curcumin delivered by dual-responsive polymeric nanoparticles improve chemotherapeutic efficacy based on the enhanced anti-metastasis activity and reduce side effects. *Acta Pharmaceutica Sinica B*. 2020;10(6):1106-21.

67. Naves LB, Dhand C, Venugopal JR, Rajamani L, Ramakrishna S, Almeida L. Nanotechnology for the treatment of melanoma skin cancer. *Progress in biomaterials*. 2017;6(1):13-26.

68. Avagliano A, Ruocco MR, Nasso R, Aliotta F, Sanità G, Iaccarino A, et al. Development of a stromal microenvironment experimental model containing proto-myofibroblast like cells and analysis of its crosstalk with melanoma cells: a new tool to potentiate and stabilize tumor suppressor phenotype of dermal myofibroblasts. *Cells*. 2019;8(11):1435.

69. James N, Coker R, Tomlinson D, Harris J, Gompels M, Pinching A, et al. Liposomal doxorubicin (Doxil): an effective new treatment for Kaposi's sarcoma in AIDS. *Clinical oncology*. 1994;6(5):294-6.

70. Berges R. Eligard®: pharmacokinetics, effect on testosterone and PSA levels and tolerability. *European Urology Supplements*. 2005;4(5):20-5.

71. Tsoulfas G. The impact of the European financial crisis on clinical research within the European union or" when life gives you lemons, make lemonade". *Hippokratia*. 2012;16(1):6.

72. Lombardo D, Kiselev MA, Caccamo MT. Smart nanoparticles for drug delivery application: development of versatile nanocarrier platforms in biotechnology and nanomedicine. *Journal of Nanomaterials*. 2019;2019.

73. Wang-Gillam A, Li C-P, Bodoky G, Dean A, Shan Y-S, Jameson G, et al. Nanoliposomal irinotecan with fluorouracil and folinic acid in metastatic pancreatic cancer after previous gemcitabine-based therapy (NAPOLI-1): a global, randomised, open-label, phase 3 trial. *The Lancet*. 2016;387(10018):545-57.

74. Perez JM, Asati A, Nath S, Kaittanis C. Synthesis of biocompatible dextran-coated nanoceria with pH-dependent antioxidant properties. *Small*. 2008;4(5):552-6.

75. Sadidi H, Hooshmand S, Ahmadabadi A, Javad Hoseini S, Baino F, Vatanpour M, et al. Cerium oxide nanoparticles (Nanoceria): Hopes in soft tissue engineering. *Molecules*. 2020;25(19):4559.

76. Dhall A, Self W. Cerium oxide nanoparticles: a brief review of their synthesis methods and biomedical applications. *Antioxidants*. 2018;7(8):97.

77. Nelson BC, Johnson ME, Walker ML, Riley KR, Sims CM. Antioxidant cerium oxide nanoparticles in biology and medicine. *Antioxidants*. 2016;5(2):15.

78. Asati A, Santra S, Kaittanis C, Nath S, Perez JM. Oxidase-like activity of polymer-coated cerium oxide nanoparticles. *Angewandte Chemie*. 2009;121(13):2344-8.

79. Asati A, Santra S, Kaittanis C, Perez JM. Surface-charge-dependent cell localization and cytotoxicity of cerium oxide nanoparticles. *ACS nano*. 2010;4(9):5321-31.

80. Sung H, Ferlay J, Siegel RL, Laversanne M, Soerjomataram I, Jemal A, et al. Global cancer statistics 2020: GLOBOCAN estimates of incidence and mortality worldwide for 36 cancers in 185 countries. *CA: a cancer journal for clinicians*. 2021;71(3):209-49.

81. Winklhofer S, Lin W-C, Wang ZJ, Behr SC, Westphalen AC, Yeh BM. Comparison of positive oral contrast agents for abdominopelvic CT. *American Journal of Roentgenology*. 2019;212(5):1037-43.

82. FitzGerald PF, Colborn RE, Edic PM, Lambert JW, Torres AS, Bonitatibus Jr PJ, et al. CT image contrast of high-Z elements: phantom imaging studies and clinical implications. *Radiology*. 2016;278(3):723.

83. Lambert JW, Sun Y, Stillson C, Li Z, Kumar R, Wang S, et al. An intravascular tantalum oxide–based CT contrast agent: Preclinical evaluation emulating overweight and obese patient size. *Radiology*. 2018;289(1):103.

84. Sbitany H, Koltz PF, Mays C, Girotto JA, Langstein HN. CT contrast extravasation in the upper extremity: strategies for management. *International Journal of Surgery*. 2010;8(5):384-6.

85. Zhang X, Zhang R, Huang J, Luo M, Chen X, Kang Y, et al. Albumin enhances PTX delivery ability of dextran NPs and therapeutic efficacy of PTX for colorectal cancer. *Journal of Materials Chemistry B*. 2019;7(22):3537-45.

86. Datta A, Mishra S, Manna K, Saha KD, Mukherjee S, Roy S. Pro-oxidant therapeutic activities of cerium oxide nanoparticles in colorectal carcinoma cells. ACS omega. 2020;5(17):9714-23.

87. Wang J, Luo B, Li X, Lu W, Yang J, Hu Y, et al. Inhibition of cancer growth in vitro and in vivo by a novel ROS-modulating agent with ability to eliminate stem-like cancer cells. *Cell death & disease*. 2017;8(6):e2887-e.

88. Miri A, Darroudi M, Sarani M. Biosynthesis of cerium oxide nanoparticles and its cytotoxicity survey against colon cancer cell line. Applied Organometallic Chemistry. 2020;34(1):e5308.

89. Lu M, Zhang Y, Wang Y, Jiang M, Yao X. Insight into several factors that affect the conversion between antioxidant and oxidant activities of nanoceria. *ACS applied materials & interfaces*. 2016;8(36):23580-90.

90. Gao R, Mitra RN, Zheng M, Wang K, Dahringer JC, Han Z. Developing Nanoceria-Based pH-Dependent Cancer-Directed Drug Delivery System for Retinoblastoma. *Advanced functional materials*. 2018;28(52):1806248.

91. Yang J, Zhou J, Zhao Y, Zhu L, Luo G, Ge B. Hollow CeO2 with ROS-Scavenging Activity to Alleviate Colitis in Mice. *International Journal of Nanomedicine*. 2021;16:6889.

92. Lord MS, Berret JF, Singh S, Vinu A, Karakoti AS. Redox active cerium oxide nanoparticles: Current status and burning issues. *Small*. 2021;17(51):2102342.

93. Alpaslan E, Geilich BM, Yazici H, Webster TJ. pH-controlled cerium oxide nanoparticle inhibition of both gram-positive and gram-negative bacteria growth. *Scientific reports*. 2017;7(1):1-12.

94. Yazici H, Alpaslan E, Webster TJ. The role of dextran coatings on the cytotoxicity properties of ceria nanoparticles toward bone cancer cells. *Jom*. 2015;67(4):804-10.

95. Edwards H, Johnson A, Lewis I. Applications of Raman spectroscopy to the study of polymers and polymerization processes. *Journal of Raman spectroscopy*. 1993;24(8):475-83.

96. Idris MNSiM, Chiang H-P, Muslim N, Chau Y-FC, Mahadi AH, Voo NY, et al., editors. A Comparative Study of Visible Raman Scattering of Ceria Prepared by Sol-gel and Hydrothermal Techniques with Gold Nanoparticles. *IOP Conference Series: Materials Science and Engineering*; 2018: IOP Publishing.

97. Dutta D, Mukherjee R, Patra M, Banik M, Dasgupta R, Mukherjee M, et al. Green synthesized cerium oxide nanoparticle: a prospective drug against oxidative harm. *Colloids and surfaces B: Biointerfaces*. 2016;147:45-53.

98. Mohammadi MR, Malkovskiy AV, Jothimuthu P, Kim K-M, Parekh M, Inayathullah M, et al. PEG/dextran double layer influences Fe ion release and colloidal stability of iron oxide nanoparticles. *Scientific reports*. 2018;8(1):1-11.

99. Demchenko AP. Beyond annexin V: fluorescence response of cellular membranes to apoptosis. *Cytotechnology*. 2013;65(2):157-72.

100. Crowley LC, Scott AP, Marfell BJ, Boughaba JA, Chojnowski G, Waterhouse NJ. Measuring cell death by propidium iodide uptake and flow cytometry. *Cold Spring Harbor Protocols*. 2016;2016(7):pdb. prot087163.

101. Hu X-m, Li Z-x, Lin R-h, Shan J-q, Yu Q-w, Wang R-x, et al. Guidelines for regulated cell death assays: a systematic summary, a categorical comparison, a prospective. *Frontiers in cell and developmental biology*. 2021;9:634690.

102. Guo R, Wang Y, Yu S, Zhu W, Zheng F, Liu W, et al. Dual role of hydrogen peroxide on the oxidase-like activity of nanoceria and its application for colorimetric hydrogen peroxide and glucose sensing. *RSC advances*. 2016;6(65):59939-45.

103. Davoodbasha MA, Saravanakumar K, Abdulkader AM, Lee S-Y, Kim J-W. Synthesis of biocompatible cellulose-coated nanoceria with pH-dependent antioxidant property. *ACS Applied Bio Materials*. 2019;2(5):1792-801.

104. Diaconeasa Z, Barbu-Tudoran L, Coman C, Leopold L, Mesaros A, Pop O, et al. Cerium oxide nanoparticles and its cytotoxicity human lung cancer cells. *Romanian Biotechnological Letters*. 2015;20(4):10679.

105. Chen W, Li F, Yu J. Combustion synthesis and characterization of nanocrystalline CeO2-based powders via ethylene glycol–nitrate process. *Materials Letters*. 2006;60(1):57-62.

106. Farahmandjou M, Zarinkamar M, Firoozabadi T. Synthesis of Cerium Oxide (CeO2) nanoparticles using simple CO-precipitation method. *Revista mexicana de fisica*. 2016;62(5):496-9.

107. Wang W, Howe JY, Li Y, Qiu X, Joy DC, Paranthaman MP, et al. A surfactant and template-free route for synthesizing ceria nanocrystals with tunable morphologies. *Journal of Materials Chemistry*. 2010;20(36):7776-81.

108. Wang L, Wang Y, Zhang Y, Yu Y, He H, Qin X, et al. Shape dependence of nanoceria on complete catalytic oxidation of o-xylene. *Catalysis Science & Technology*. 2016;6(13):4840-8.

109. Hanafy BI, Cave GW, Barnett Y, Pierscionek B. Ethylene glycol coated nanoceria protects against oxidative stress in human lens epithelium. *RSC advances*. 2019;9(29):16596-605.

110. Li C, Zhao W, Liu B, Xu G, Liu L, Lv H, et al. Cytotoxicity of ultrafine monodispersed nanoceria on human gastric cancer cells. *Journal of Biomedical Nanotechnology*. 2014;10(7):1231-41.

111. Cha H-R, Babu VR, Rao K, Kim Y-H, Mei S, Joo W-H, et al. Fabrication of amino acid based silver nanocomposite hydrogels from PVA-poly (acrylamide-co-acryloyl phenylalanine) and their antimicrobial studies. *Bulletin of the Korean Chemical Society*. 2012;33(10):3191-5.

112. Li Y, Hou X, Yang C, Pang Y, Li X, Jiang G, et al. Photoprotection of cerium oxide nanoparticles against UVA radiation-induced senescence of human skin fibroblasts due to their antioxidant properties. *Scientific reports*. 2019;9(1):1-10.

113. Costantino F, Cavaliere E, Gavioli L, Carzino R, Leoncino L, Brescia R, et al. Photocatalytic activity of cellulose acetate nanoceria/Pt hybrid mats driven by visible light irradiation. *Polymers*. 2021;13(6):912.

114. Kaygusuz H, Erim FB. Biopolymer-assisted green synthesis of functional cerium oxide nanoparticles. *Chemical Papers*. 2020;74(7):2357-63.

115. Akhtar MJ, Ahamed M, Alhadlaq HA, Khan MM, Alrokayan SA. Glutathione replenishing potential of CeO2 nanoparticles in human breast and fibrosarcoma cells. *Journal of colloid and interface science*. 2015;453:21-7.

116. Lord MS, Tsoi B, Gunawan C, Teoh WY, Amal R, Whitelock JM. Anti-angiogenic activity of heparin functionalised cerium oxide nanoparticles. *Biomaterials*. 2013;34(34):8808-18.

APPENDIX A: EQUIPMENTS AND CATALOG NUMBERS

Name of Equipment	Cat No, Brand, Country
Inverted light microscope	CKX41, Olympus, USA
Automated cell counter	LunaII, ThermoFisher, USA
Centrifuge	5702R, Eppendorf, Germany
Class II Biological Safety Cabinets	AC2-4L1, ESCO, Southeast Asia
Water bath	Benchmark Scientific, USA
Pipette	Easypet 2, Eppendorf, Germany
Vacuum glass	BORO 3.3, Isolab, Germany
Incubator	Sanyo, Japan
Pipette (10, 100, 200, 1000 μL)	Research Plus, Eppendorf, Germany
Refrigerator (+4)	Arçelik, Turkey
Freezer (-20)	Bosch, Germany
Freezer (-80)	U570, New Brunswick Scientific, USA
Imaging reader Cytation 5	BioTek, USA
Cryogenic vial	430488, Corning, USA
Liquid Nitrogen Tank	LS750, Worthington, USA
Mr.Frosty Freezing Container	5100-0001, Thermo Fisher Scientific, USA
UV-Vis Spectroscopy	DU 800, Beckman Coulter, USA
Dynamic Light Scattering	Malvern Instruments, UK
Vortex	Scientific Industries, USA
Power Supply	Bio-Rad, USA
Ice Machine	AF100, Scotsman, USA
PH Meter	30046241, Mettler Toledo, Switzerland

APPENDIX B: LIST OF SOLUTION AND KITS

Name of Buffer, Solution and Kits	Cat No, Brand, Country
2′,7′-Dichlorofluorescin diacetate	D6883, Sigma Aldrich, USA
WST-1	11 644 807 001, Roche, USA
Dimethyl Sulfoxide (DMSO)	BP231, Thermo Fisher Scientific, USA
UltraPure™ Cell Culture Grade Water	S30529, Hyclone, USA
Trypan Blue	T8154, Sigma Aldrich, USA
MycoAlert PLUS™	Lonza, Switzerland
Phosphate Buffered Saline	806544, Sigma Aldrich, USA
Penicillin-Streptomycin	15140-122, Gibco, USA
L-Glutamine 200mM (100X)	25030-081, Gibco, USA
Trypsin-EDTA 0.25%	25200-056, Gibco, USA
F12 Kaighn's Modification	SH30526.01, Hyclone, USA
McCoy’s 5A Medium	M9309, Sigma, USA
Dulbecco’s Modified Eagle’s Medium- High Glucose (DMEM)	D5796, Sigma, USA
RPMI-1640 Medium	SH30255.01, Hyclone, USA
Heat-inactivated fetal bovine serum	SV30160.03HI, Hyclone, USA
Dextran from Leuconostoc Mesenteroides	D9260-10G, Sigma Aldrich, USA
Dextran from Leuconostoc spp.	31388-25G, Sigma Aldrich, USA
Cerium (III) Nitrate Hexahydrate	392219, Sigma Aldrich, USA
Ammonium Hydroxide Solution	221228, Sigma Aldrich, USA
MycoAlert™ Plus Mycoplasma Detection Kit	LT07-703, Lonza, CH

APPENDIX C: LIST OF CELL LINES

Cell Line	Cat No, Brand, Country
COLO 201, Human Adenocarcinoma; Colorectal; Dukes' type D	CCL-224, ATCC, USA
DLD-1, Human Adenocarcinoma; Colorectal; Dukes' type C	CCL-221, ATCC, USA
LoVo, Human Adenocarcinoma; Colorectal; Dukes' type C, grade IV	CCL-229, ATCC, USA
HT-29, Human Adenocarcinoma; Colorectal	HTB-38, ATCC, USA
SW48 Human Adenocarcinoma; Colorectal; Dukes' type C, grade IV	CCL-231, ATCC, USA